

# **Coupled adsorption and redox interface reactions governing the retention of Se and Tc on Fe(II)/Fe(III)-bearing clay minerals**

Inaugural dissertation  
of the Faculty of Science,  
University of Bern

presented by  
Yanting Qian  
from China

Supervisor of the doctoral thesis:  
Prof. Dr. Sergey V. Churakov  
Institute of Geological Sciences, University of Bern and Laboratory for Waste  
Management, Paul Scherrer Institut

Supervisor:  
Dr. Maria Marques Fernandes  
Nuclear Energy and Safety Division, Paul Scherrer Institut

Co-supervisor:  
Dr. Sylvain Grangeon  
Bureau de Recherches Géologiques et Minières



**Coupled adsorption and redox interface reactions governing the  
retention of Se and Tc on Fe(II)/Fe(III)-bearing clay minerals**

Inaugural dissertation  
of the Faculty of Science,  
University of Bern

presented by  
Yanting Qian  
from China

Supervisor of the doctoral thesis:  
Prof. Dr. Sergey V. Churakov  
Institute of Geological Sciences, University of Bern and Laboratory for Waste  
Management, Paul Scherrer Institut

Supervisor:  
Dr. Maria Marques Fernandes  
Nuclear Energy and Safety Division, Paul Scherrer Institut

Co-supervisor:  
Dr. Sylvain Grangeon  
Bureau de Recherches Géologiques et Minières

Bern, 16.01.2024

The Dean  
Prof. Dr. Marco Herwegh

The original document is available from the repository of the University of Bern (BORIS).



This work is licensed under a Creative Commons Attribution 4.0 International License. To view a copy of this license, visit <https://creativecommons.org/licenses/by/4.0/> or send a letter to Creative Commons, PO Box 1866, Mountain View, CA 94042, USA.

## Acknowledgment

I would like to express my deepest gratitude to those who contribute to the successful completion of this thesis. I want to thank my supervisor Dr. Maria Marques Fernandes and Prof. Dr. Sergey Churakov for giving me the opportunity to work on this PhD project and the constant support and encouragement throughout the four years. I also want to thank my co-supervisor Dr. Grangeon Sylvain for his support in clay characterization including sample preparation, collaboration of other characterization methods, and guidance in data analysis. I am very thankful to Dr. Andreas C. Scheinost for his professional support in beamtime measurements, detailed discussion, constructive suggestions, and efficient correction on my writings. Many thanks also go to Dr. Jean-Marc Greneche for Mössbauer spectrometry measurements, Dr. Alwina Hoving for MEO/MER measurements, Eric Bourhis for XPS measurements, Nicolas Maubec XRD measurements, Dr. Elisabeth Agnes Müller Gubler for SEM and TEM measurements of Tc, Astrid Schaible for guidance in clay purification, Andreas Laube for ICP-OES measurements, and Jörg Exner for assisting with EXAFS measurements. This PhD thesis would never be possible without your great contributions.

I would like to extend my thanks to all the colleagues at LES. In particular, I want to thank Dr. Bin Ma and Dr. Zhe Yang for their insightful and detailed discussion of my experiment data; Dr. Rainer Dähn for advice on EXAFS data analysis; and Cyrill Lang, Petar Bunic, and Dominik Kunz for laboratory help. Furthermore, I would like to give big thanks to my lunch group Dan Miron, Vasyl Stotskyi, Athanasios Mokos, Haonan Peng, Romana Boiger, and Enzo Curti for the awesome lunch therapy where I can freely express my opinions and release my stress. Additionally, I would like to thank Xiaoyan Wei, Olha Marinich, and Fulvio Di Lorenzo for creating a good office environment.

Finally, I would like to thank my parents for their unconditional love and support throughout the four PhD years and covid period, which built up a solid foundation for me to be myself, explore the world, and always stretch forward. Importantly, I am grateful for being in my church family, where I constantly had delicious food, happy outdoor sports, joyful car rides, constructive conversations, caring tea times, and loving hugs. Without these support in life, I wouldn't enjoy Switzerland so much. Because out from Him and through Him and to Him are all things. To Him be the glory forever. (Romans 11:36)

**Financial support:**

This project is financed by the European Union's Horizon 2020 research and innovation program under grant agreement No 847593.

Yanting Qian  
Zurich, 05.11. 2023

## Abstract

$^{79}\text{Se}$  and  $^{99}\text{Tc}$  are two long-lived fission products with high levels of toxicity.  $\text{Se(IV)}$  and  $\text{Tc(VII)}$  are present in vitrified high-level radioactive waste (HLW) in highly mobile forms. The potential release of these elements from the repository poses a significant threat to the biosphere. Therefore, it is imperative to employ the clay engineered backfill materials to impede the migration of  $\text{Se(IV)}$  and  $\text{Tc(VII)}$  towards the biosphere. Considering the extremely low solubility of reduced Se and Tc, reduction of  $\text{Se(IV)}$  and  $\text{Tc(VII)}$  stands out as one of the most effective approaches to slow down their migration. Clay minerals, primary components of bentonite, the chosen engineered backfill material, naturally contain structural  $\text{Fe(III)}$  which readily undergoes reduction to  $\text{Fe(II)}$  in the reducing environment of the repository. This transformation facilitates its role as a reductant for  $\text{Se(IV)}$  and  $\text{Tc(VII)}$ . As such, this thesis primarily aims to investigate the pivotal role of Fe within the clay mineral, and to quantitatively assess its impact on the retention of Se and Tc.

In the first step of the study, it is essential to reduce the structural  $\text{Fe(III)}$  present in the native clay mineral to  $\text{Fe(II)}$ , thus establishing a reducing potential. This thesis employed three distinct types of 2:1 dioctahedral clay minerals, namely Texas montmorillonite STx-1, Wyoming montmorillonite SWy-2, and nontronite clay NAu-2. These clays were chosen due to their varying Fe content, which leads to different ratios of  $\text{Fe(II)/Fe(III)}$  and diverse Fe distributions within the octahedral sheet. Consequently, the reduced clay exhibits varying redox potentials. Following reduction, comprehensive characterization of the modified clay minerals was performed, including assessments of their structure, morphology, cation exchange capacity, and the accessibility of sorption edge sites. The results of this characterization demonstrated negligible alterations in structural integrity and sorption properties of the reduced clay minerals when compared to their native counterparts.

In the second step, batch sorption experiments were systematically conducted, varying parameters including pH levels, Se and Tc concentrations, reaction durations, and the use of reduced clay samples with different  $\text{Fe(II)}$  content and redox potential. Following these sorption experiments, spectroscopic techniques, X-ray Absorption Near Edge Spectroscopy (XANES) and Extended X-ray Absorption Fine Structure (EXAFS), were applied to discern the reduction products and ascertain the local structure of Se and Tc.

The sorption experiments revealed that all reduced clay minerals possess the capacity to effectively impede the migration of Se and Tc.  $\text{Se(IV)}$  exhibited sorption via an inner-sphere surface complex, followed by reduction, resulting in the formation of red  $\text{Se(0)}$

initially, which gradually transformed into grey Se(0) as insoluble solids. In contrast, the retention mechanism for Tc(VII) involved its reduction to Tc(IV), leading to the formation of  $\text{TcO}_2 \cdot n\text{H}_2\text{O}$  precipitate, with no detectable adsorbed Tc species observed. Despite the differences in the retention mechanisms, both Se and Tc retention efficiency were found to be directly proportional to the structural Fe(II) content. Furthermore, the presence of surface adsorbed  $\text{Fe}^{2+}_{\text{aq}}$  was found to enhance the retention of Tc.

The findings presented in this thesis provide compelling evidence that Fe(II)/Fe(III)-bearing clay minerals hold significant promise for immobilizing Se and Tc within the engineered barriers of a repository. Moreover, the sorption data generated enriches the geochemical sorption modeling database, further enhancing our understanding of these retention processes. The insights gained from this thesis make a substantial contribution to the risk assessment of repository systems.



# Table of Contents

**Acknowledgment..... i**

**Abstract..... iii**

**Chapter 1: Introduction ..... 1**

1.1 Background ..... 2

1.2 Fe-bearing clay minerals ..... 3

1.3 Redox reaction between Fe-bearing clay minerals and Se and Tc..... 8

1.4 Objectives of the thesis ..... 10

1.5 Outline of the thesis..... 12

1.6 References ..... 14

**Chapter 2: Oxidation state and structure of Fe in nontronite: from oxidizing to reducing conditions..... 20**

Abstract ..... 21

2.1 Introduction ..... 22

2.2 Materials and methods ..... 25

2.2.1 Clays and clay reduction by Citrate-Bicarbonate-Dithionite..... 25

2.2.2 X-ray diffraction ..... 26

2.2.3 Transmission electron microscopy ..... 27

2.2.4 <sup>57</sup>Fe Mössbauer spectrometry ..... 27

2.2.5 X-ray photoelectron spectroscopy ..... 28

2.2.6 XANES and EXAFS sample preparation and spectra collection ..... 28

2.2.7 Mediated electrochemical oxidation and reduction..... 29

2.3 Results and discussion..... 30

2.3.1 Reduction..... 30

2.3.2 X-ray diffraction ..... 32

2.3.3 Transmission electron microscopy ..... 32

2.3.4 Mössbauer spectrometry..... 35

2.3.5 X-ray photoelectron spectroscopy ..... 37

2.3.6 Fe K-edge XAFS ..... 38

2.3.7 Mediated electrochemical oxidation and reduction..... 42

2.3.8 Fe redox state identification ..... 43

2.4 Conclusions ..... 44

Acknowledgments ..... 45

2.5 Reference..... 46

2.6 Supporting information ..... 55

**Chapter 3: Influence of structural Fe content in clay minerals on selenite redox**

<b>reactions: kinetics and structural transformations.....</b>	<b>60</b>
Abstract .....	61
3.1 Introduction .....	62
3.2 Materials and methods.....	64
3.2.1 Clays .....	64
3.2.2 Preparation of reduced clay suspensions .....	65
3.2.3 Cation exchange capacity and edge site availability .....	66
3.2.4 Se sorption kinetics.....	67
3.2.5 X-ray absorption spectroscopy .....	68
3.2.6 Mediated electrochemical reduction and oxidation.....	69
3.3 Results and discussion.....	70
3.3.1 Clay characterization .....	70
3.3.2 Sorption kinetics .....	71
3.3.3 Se K-edge XAFS measurements of kinetic clay samples.....	73
3.3.4 Se reduction .....	78
3.3.5 Structure of the initial selenite sorption complex .....	83
3.3.6 Redox potential of clays .....	85
3.4 Conclusion.....	89
Acknowledgement.....	90
3.5 Reference.....	91
3.6 Supporting information .....	97
<b>Chapter 4: The retention of technetium by Fe-bearing clay minerals.....</b>	<b>98</b>
Abstract .....	99
4.1 Introduction .....	99
4.2 Materials and methods.....	102
4.2.1 Clay preparation and reduction.....	102
4.2.2 Tc sorption experiments .....	103
4.2.3 X-ray absorption spectroscopy .....	104
4.2.4 Transmission electron microscope .....	104
4.3 Results and discussion.....	105
4.3.1 Tc sorption edge .....	105
4.3.2 Tc sorption isotherm .....	107
4.3.3 Tc K-edge XAFS measurements of sorption isotherm clay samples .....	109
4.3.4 Tc retention by Fe(II) species .....	112
4.3.5 Tc(VII) reduction products .....	115
4.3.6 Electron transfer in Tc retention by Fe(II) clay minerals .....	116

4.4 Conclusion and outlook.....	117
Acknowledgment .....	118
4.5 Reference.....	119
<b>Chapter 5: Comparison of the retention of Se and Tc .....</b>	<b>124</b>
5.1 Chemical properties.....	125
5.2 Retention mechanism .....	125
5.3 Reference.....	129
<b>Chapter 6: Conclusions and outlook.....</b>	<b>130</b>
6.1 Conclusions .....	131
6.2 Outlook.....	134
6.3 Reference.....	136
<b>Declaration of consent .....</b>	<b>139</b>



## Chapter 1: Introduction

## 1.1 Background

Deep geological repository is considered as the safest option for a long-term disposal of spent nuclear fuel (SF) and vitrified high-level radioactive waste (HLW) (IAEA, 2003). In September 2022, National Cooperative for the Disposal of Radioactive Waste (Nagra) announced the intention to submit the general license application for construction of the Swiss radioactive waste repository in “Nördlich Lägern” region using Opalinus clay as the host rock. In the Swiss concept of deep geological repository (Figure 1.1), SF and HLW sealed in steel canisters are disposed in tunnels and back-filled with highly compacted bentonite clays as an engineered barrier (Nagra, 2002). In the initial stage of the repository, oxygen entrapped in the pores of multi-barrier system may be consumed gradually by corrosion of steel canister within less than 100 years. After consumption of oxygen, anoxic corrosion of steel canister ( $\text{Fe}^0 + 2 \text{H}_2\text{O} \leftrightarrow \text{Fe}^{2+} + \text{H}_2 + 2 \text{OH}^-$ ) produces large amount of  $\text{H}_2$  and ferrous (Fe(II)) iron phases like magnetite, siderite, pyrite, iron oxides, and green rust. The repository maintains an anoxic reducing condition. The redox potential (Eh) of the repository is estimated to range between -0.1 V and -0.3 V (SHE) (Wersin et al., 2003). Over time, as the steel canisters corrode completely, radionuclides will be released. The engineered and natural barriers are designed to retard the migration of radionuclides over an extended period of time, isolating them from the biosphere and ensuring that any residual radionuclides reaching the biosphere will have radioactivity levels similar to the natural background (Vuori, 1995).

In Switzerland, HLW refers to the vitrified highly active residue resulting from the reprocessing of spent nuclear fuel, which contains a majority of the radioactive fission products recovered by reprocessing of spent nuclear fuel (Nagra, 2002). According to the safety assessment calculations, the main long-term dose determining radionuclides present in HLW include  $^{14}\text{C}$ ,  $^{129}\text{I}$ ,  $^{99}\text{Tc}$ ,  $^{79}\text{Se}$ ,  $^{135}\text{Cs}$ , and  $^{36}\text{Cl}$ , etc. (McGinnes, 2002). Specifically, this thesis will focus on studying the two redox-sensitive radionuclides  $^{79}\text{Se}$  and  $^{99}\text{Tc}$ . Although Se occurs in the -II oxidation state in spent nuclear fuel (Curti et al., 2015), it is present in IV oxidation state in simulated vitrified waste (Curti et al., 2013). Tc is present as a mixture of Tc(IV)/Tc(VII) in the glass after vitrification (Childs et al., 2018). When the canister is fully corroded, Se and Tc in these oxidation states will be released to the near field. There is a strong interplay between the mobility and bioavailability of Tc and Se and their respective oxidation states (Fernández-Martínez and Charlet, 2009; Meena and Arai, 2017). Se(IV) and Tc(VII) are highly soluble and mobile. When reduced to lower oxidation

states such as elemental Se(0) and Tc(IV), they become insoluble and immobile, thus leading to effective retention. Therefore, the reducing environment within the repository, coupled with the formation of redox-sensitive Fe(II)/Fe(III) phases and the pH level of the pore water, exerts a significant influence on the retention and transport of Tc and Se when released from canister. Given their long half-life and elevated toxicity, it is crucial to gain a comprehensive understanding of the migration behavior of Tc and Se in order to ensure an accurate safety assessment of the repository.

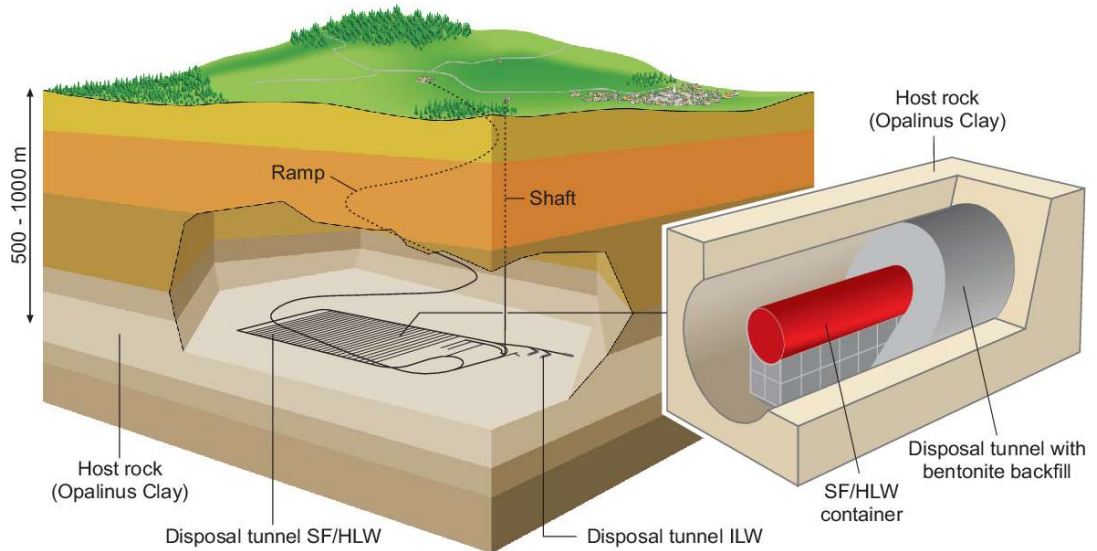


Figure 1.1. Possible View of the Swiss concept of deep geological repository for radioactive waste SF/HLW/ILW. SF: spent fuel; HLW: high-level waste; ILW: intermediate-level waste. (Nagra, 2002)

## 1.2 Fe-bearing clay minerals

Bentonite is considered as backfill material due to its diverse physical and chemical properties: low hydraulic permeability/conductivity, swelling pressure accompanied with self-sealing ability, high sorption capacity, and long-term durability of properties (Pusch, 2006; Sellin and Leupin, 2013; Wagner, 2013).

- *Low hydraulic permeability/conductivity:*

Bentonite has a very fine particle size, which results in a densely packed structure with extremely small pores. It is able to sustain significant hydraulic pressure gradient, giving it low hydraulic permeability. In other words, it acts as an effective barrier against the flow of water.

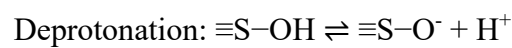
- *Swelling pressure and self-sealing ability:*

When hydrated, bentonite has the ability to swell and expand. This property is particularly important in scenarios where the backfill material is exposed to water. The swelling pressure exerted by bentonite helps it conform to the surrounding environment, filling any gaps or voids that may exist. In addition, this self-sealing ability ensures the reducing environment inside of the repository.

- *High sorption capacity:*

Bentonite possesses a high capacity to absorb and retain metal ions (Ifeoma Mary and Onyedikachi Anthony, 2019; Liu et al., 2022; Tournassat et al., 2015). This property is crucial in a repository context because it allows bentonite to immobilize radionuclides, preventing them from migrating through the backfill material.

Bentonite consists of montmorillonite, while Opalinus clay is composed mainly of illite and illite/smectite mixed layer minerals (Bradbury et al., 2014). Both montmorillonite and illite are 2:1 dioctahedral clay minerals with a TOT layer structure, including an alumina octahedral (O) sheet sandwiched between two silica tetrahedral (T) sheets (Bergaya and Lagaly, 2006), as shown in Figure 1.2. Clay mineral exhibits a permanent negative charge, due to isomorphous substitution by lower valence cations in either the octahedral sheet (i.e. substitution of  $Mg^{2+}$ ,  $Fe^{2+}$ , or  $Mn^{2+}$  for  $Al^{3+}$ ) or the tetrahedral sheet (i.e. substitution of  $Al^{3+}$  or rarely  $Fe^{3+}$  for  $Si^{4+}$ ). The permanent negative charge is compensated by the electrostatic adsorption of hydrated exchangeable cations in the interlayer (Liu et al., 2022). Edge sites of clay minerals, characterized by surface hydroxyl groups ( $\equiv S-OH$ ), are the primary sites to form surface sorption complexes. The surface hydroxyl is amphoteric and can undergo both protonation and deprotonation reactions, as demonstrated below:





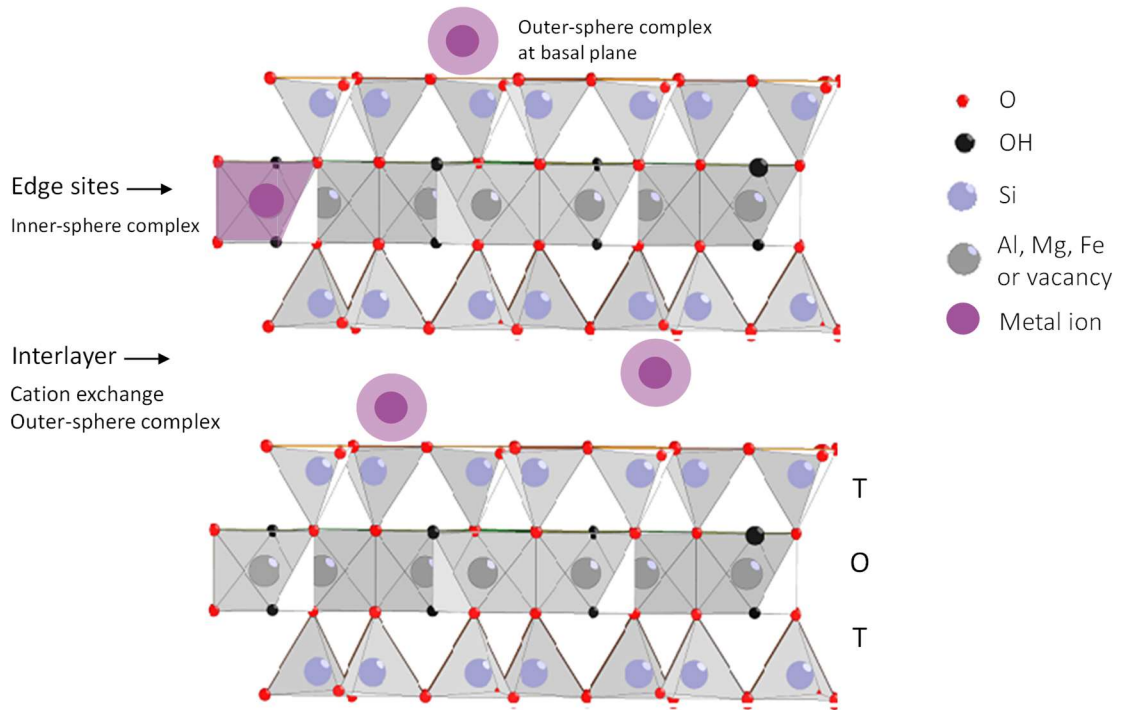
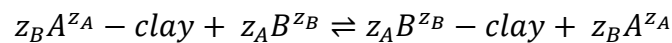


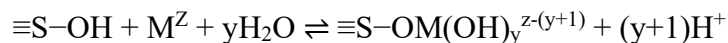
Figure 1.2. Sketch of a 2:1 dioctahedral clay mineral with an alumina octahedral sheet sandwiched between two silica tetrahedral sheets, and inner-sphere and outer-sphere complex with the clay mineral (modified from Soltermann (2014)).

Clay mineral is a charged particle with a high specific surface area, making it well-known for its sorption properties. There are two major sorption mechanisms on clay minerals: cation exchange and surface complexation. Hydrated exchangeable cations can form outer-sphere complexes with the clay minerals in the interlayer and basal planes through electrostatic forces and be exchanged by other metal cations (Tournassat et al., 2015). The cation exchange reaction of a metal B, of valence  $z_B$ , exchanging with a metal A, of valence  $z_A$ , on a clay mineral in the A-form, can be written as:



The surface complexation at the edge site is pH-dependent due to the protonation and deprotonation of the hydroxyl group, which can establish chemical bonds with the adsorbed ions forming inner-sphere sorption complexes (Stumm, 1995). If aqueous speciation does not change, cation adsorption generally increases as pH increases (Baeyens and Marques Fernandes, 2018). With the exception of the alkaline and alkaline-earth metals, most metals ions such as transition metals, lanthanides and actinides form surface complexes at the edge sites of clay minerals. Surface complexation reactions on generic edge sites can be written

as:



where  $M$  is a metal with valence  $z$ , and  $y$  is an integer. For  $y = 0$  the surface complex is  $\equiv\text{SOM}^{Z-1}$ . For anions, the adsorption decreases as pH increases, such as Cr(VI) (Joe-Wong et al., 2017; Rai et al., 1989; Zachara et al., 1988), Se(IV) (Missana et al., 2009), and As(V) (Goldberg, 2002; Lin and Puls, 2000; Mohapatra et al., 2007). Anion adsorption onto  $\equiv\text{SOH}$  sites can be described in the low pH range with reactions below:



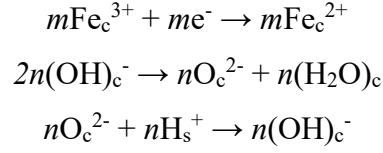
Iron is the fourth most abundant elements in the earth's crust and is ubiquitous in clay minerals. Fe is naturally incorporated into the clay structure and can be found mostly in the octahedral sheets of the clay mineral. The content of structural Fe varies among different clay minerals, such as approximately 3 wt% in montmorillonite and 20 wt% in nontronite (Stucki, 2006). Additionally, as a result of steel canister corrosion, dissolved  $\text{Fe}^{2+}$  in  $\mu\text{M}$  concentration will be adsorbed onto the surface of clay minerals. Consequently, Fe-bearing clay minerals in the geological repository can exist in several forms (Nagra, 2013):

- (i) Structural Fe ( $\text{Fe(II)}_{\text{str}}$ ) mostly located in the octahedral sheets of the clay minerals;
- (ii)  $\text{Fe}^{2+}$  adsorbed ( $\text{Fe(II)}_{\text{ad}}$ ) onto the surface of the clay minerals;
- (iii) Fe precipitated as ferrous iron containing minerals including ferrous oxides, sulfides, and carbonates on the surface of clay minerals.

The retention of Tc (Fan et al., 2013; Liu et al., 2012; Pearce et al., 2014; Pepper et al., 2003; Wharton et al., 2000) and Se (Charlet et al., 2012; Jordan et al., 2009; Myneni et al., 1997; Scheinost and Charlet, 2008) on ferrous iron containing minerals (iii) have been intensively studied. In this study, only Fe-bearing clay mineral form (i) and (ii) were discussed.

Fe is a redox-sensitive element, and its redox couple  $\text{Fe(II)}/\text{Fe(III)}$  has an important impact on the redox reactivity of the clay mineral. In terms of form (i)  $\text{Fe(II)}_{\text{str}}$ , the structural arrangement of Fe in the clay mineral is intimately connected to its redox reactivity. The location of structural Fe in the octahedral sheet can be either random or clustered, leading to different chemical properties of clay minerals. When the Fe atoms are too far apart to interact with one another, intervalence electron transfer may not occur, impacting the redox activity of the structural Fe (Komadel et al., 2006; Schuette et al., 2000). Dioctahedral clay minerals indicate that two-thirds of the octahedral sites are occupied by trivalent cations

such as  $\text{Fe}^{3+}$  and  $\text{Al}^{3+}$ , while one-third of the octahedral sites remain vacant. The distribution of these vacant sites has been studied extensively. The vacancy with hydroxyl groups located on the opposite side is labelled a trans-vacancy, while the one on the same side is labelled as a cis-vacancy. Initial proposals suggested a shift in Fe coordination from six-fold to five-fold via dehydration after the chemical reduction of clay minerals (Drits and Manceau, 2000; Stucki and Roth, 1977). The chemical reactions are shown below:



where  $m$  and  $n$  are stoichiometric parameters, and subscripts  $c$  and  $s$  are species from the crystal structure and solution, respectively. However, years later, Manceau et al. observed that the octahedral Fe(III) in dioctahedral smectite remains in six-fold coordination as it was reduced to octahedral Fe(II). Meanwhile, the octahedral Fe(II) cations migrate from cis-sites to neighboring empty trans-sites and possibly form Fe clusters in the smectite structure (Manceau et al., 2000). It is widely accepted that changes in the structural Fe(II) content through clay reduction may cause a rearrangement of Fe and vacant sites, consequently affecting electron transfer and the corresponding redox properties (Charlet et al., 2022; Manceau et al., 2000; Neumann et al., 2011). Trioctahedral clay minerals have octahedral sites fully occupied by divalent cations without any vacant sites and are not discussed in this thesis.

Regarding the form (ii)  $\text{Fe(II)}_{\text{ad}}$ , it can be adsorbed on the clay surface at different sites described by the two site protolysis non electrostatic surface complexation and cation exchange (2SPNE SC/CE) sorption model (Bradbury and Baeyens, 1997). Based on the sorption edge of Fe(II) on Na-STx-1, it was observed that before reaching a pH of 4, Fe(II) was adsorbed at interlayer sites through cation exchange, while predominantly binding at edge sites via surface complexation between pH 4 and 9 (Soltermann et al., 2014a). Due to the clay dissolution equilibrium,  $\text{Fe}^{2+}_{\text{aq}}$  also exists in the clay suspension. These various Fe(II) species of the clay mineral,  $\text{Fe(II)}_{\text{str}}$ ,  $\text{Fe(II)}_{\text{ad}}$ , and  $\text{Fe}^{2+}_{\text{aq}}$ , display distinct levels of reactivity in sorption-redox reactions. Among them,  $\text{Fe(II)}_{\text{ad}}$  is the most reactive one,  $\text{Fe(II)}_{\text{str}}$  is less reactive than  $\text{Fe(II)}_{\text{ad}}$  due to its spatial inaccessibility and bonding environment, and  $\text{Fe(II)}_{\text{aq}}$  is least reactive species (Jaisi et al., 2008a).

The presence of the Fe(II)/Fe(III) couple in clay minerals gives rise to their redox potential (Eh), a crucial factor in redox reactions. Eh depends on various factors, including

clay structure, Fe content, Fe(II)/Fe(III) ratio, and solution pH, and is commonly determined through electrochemical methods. However, measuring redox potential can be challenging. The conventional approach employs an Eh electrode with an Eh meter, but achieving equilibrium between the electrode and clay suspension within the experimental timeframe can be difficult due to slow electron transfer (Sander et al., 2015). To overcome this limitation, Gorski et al. introduced a method known as mediated electrochemical reduction (MER) and oxidation (MEO) (Figure 1.3) (Gorski et al., 2012b). This technique involves the addition of mediators—redox-active organic radicals that facilitate electron transfer between the working electrode and clay minerals. By applying an external potential, the redox potential of the clay mineral can be accurately measured, and the redox-active Fe content as well as the Fe(II) and Fe(III) content within the clay mineral can be quantified (Gorski et al., 2012a; Gorski et al., 2013; Gorski et al., 2012b). The MER/MEO method offers significant advantages in accurately determining the redox potential of clay minerals and provides valuable insights into their redox behavior.

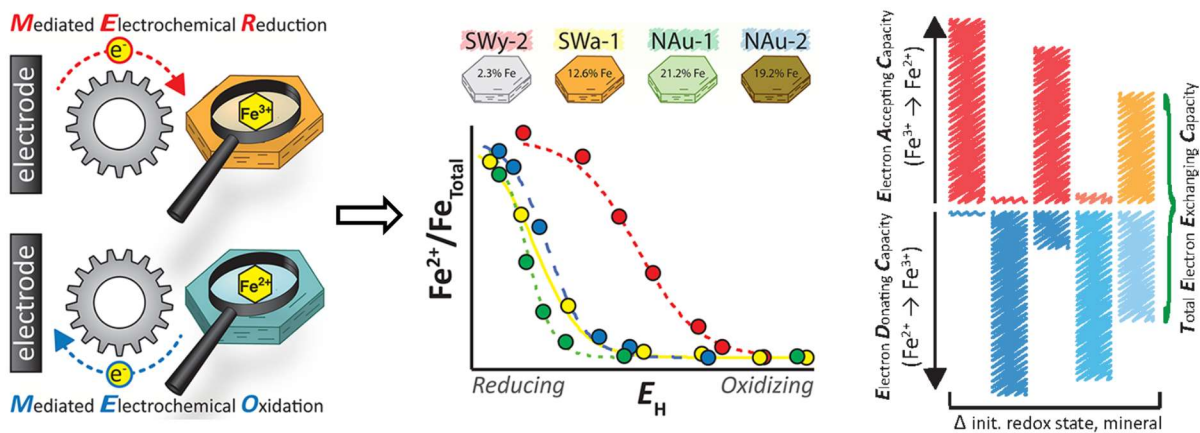


Figure 1.3. Schematic representation of mediated electrochemical reduction (MER) and oxidation (MEO) (Images from Gorski et al. (Gorski et al., 2013; Gorski et al., 2012b))

### 1.3 Redox reaction between Fe-bearing clay minerals and Se and Tc

In this study, two redox-sensitive radionuclides Se and Tc were studied. Both Se and Tc are fission products characterized by high toxicity and long half-lives (<sup>99</sup>Tc: 2.1×10<sup>5</sup> years and <sup>79</sup>Se: 3.8×10<sup>5</sup> years). Consequently, a comprehensive understanding of their migration within the multi-barrier system of the repository is of high importance. The migration of Se and Tc in the backfill clay minerals is closely linked to their solubility in the pore water. This solubility is determined by their oxidation states, which can be altered by redox reactions. As a result, redox reactions play a significant role in influencing the

migration and retention of Se and Tc on the clay minerals.

The oxidation state of Se varies from -II to VI. Oxidized species, Se(VI) and Se(IV), remain stable under oxidizing conditions, while reduced species, Se(0), Se(-I), and Se(-II), are stable under reducing conditions (Figure 1.4). Oxidized species are highly soluble and mobile, while reduced species are relatively insoluble and thus immobile. Se presents in the -II oxidation state in the spent nuclear fuel (Curti et al., 2015), but exists in IV oxidation state in simulated vitrified waste (Curti et al., 2013). After the complete corrosion of canister, soluble anions selenite ( $\text{SeO}_3^{2-}$ ) is consequently released into the near field. Although selenite does not adsorb significantly, when it interacts with Fe(II)-bearing clay minerals, it can be reduced by Fe(II) to an insoluble reduced form, thereby effectively retaining it on the clay minerals.

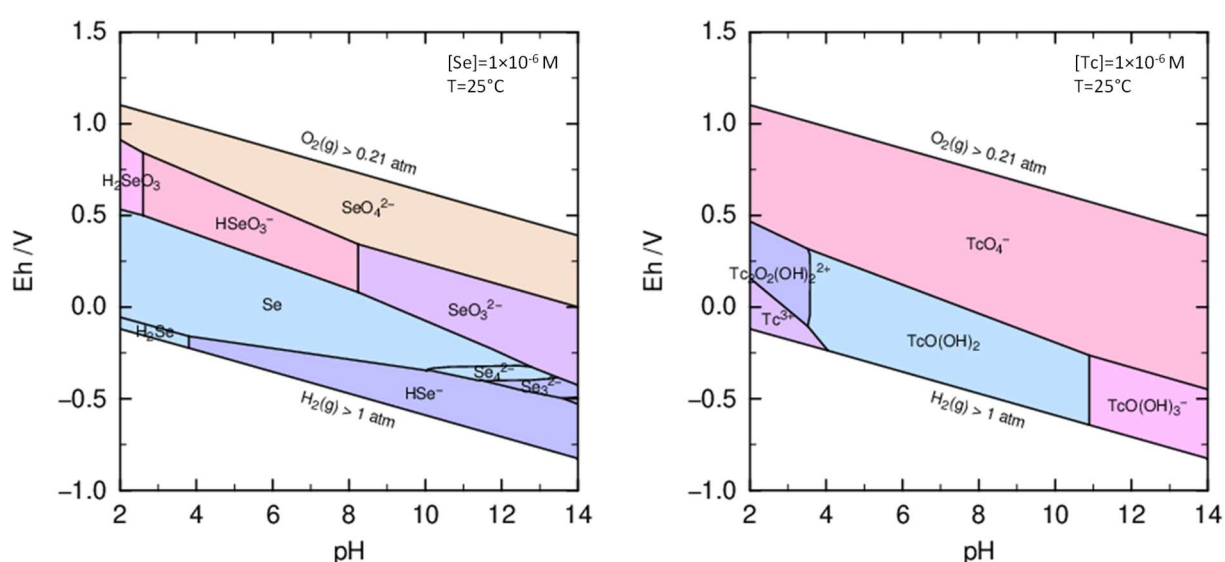


Figure 1.4. Eh-pH diagram of Se-O-H system ( $[\text{Se}] = 10^{-6} \text{ M}$ ) and Tc-O-H system ( $[\text{Tc}] = 10^{-6} \text{ M}$ ) at  $25^\circ\text{C}$ , plotted by PhreePlot using PSI Chemical Thermodynamic Database 2020. (W. Hummel, 2023)

Tc exists in several oxidation states ranging from -I to VII, with IV and VII being the most common and stable states (Heinze, 2004; Sattelberger et al., 2005). In an oxidizing environment, Tc exists as the highly soluble pertechnetate  $\text{TcO}_4^-$ , while under reducing conditions, it is reduced and precipitates as the insoluble tetravalent hydrous oxide  $\text{TcO}_2 \cdot n\text{H}_2\text{O}$  (Figure 1.4). In spent nuclear fuel,  $^{99}\text{Tc}$  is associated in metallic form with the  $\epsilon$  phase (Poineau et al., 2013). In vitrified HLW, Tc is present as a mixture of Tc(IV) and Tc(VII) within the glass matrix, and the released aqueous solution contains  $\text{TcO}_4^-$  anion (Childs et al., 2018; Muller et al., 2014).  $\text{TcO}_4^-$  anions do not significantly adsorb onto clay

minerals due to the repulsion force between the anions and negatively charged clay surfaces. However, extensive studies have demonstrated that Fe(II)-bearing clay minerals can effectively reduce Tc(VII) to Tc(IV), leading to its retention on the clay minerals (Jaisi et al., 2009; Peretyazhko et al., 2008a; Peretyazhko et al., 2008b; Zachara et al., 2007). Therefore, more research needs to be carried out to understand the mechanism of the Tc redox reaction.

In these redox reactions, Fe(II) of clay minerals acts as the reducing agent, providing the driving force for the reduction of Se and Tc. As Fe(II) undergoes oxidation to Fe(III) (Schaefer et al., 2011; Soltermann et al., 2014c), Se(IV) and Tc(VII) are reduced to lower oxidations (Jaisi et al., 2009; Scheinost and Charlet, 2008; Scheinost et al., 2008), thus, electron transfer occurs between the clay and the radionuclides across the interface. Electron transfer mechanism in the redox reactions can be generally divided into two groups: inner-sphere mechanism and outer-sphere mechanism (Chandra, 1999; Hynes, 1986). Inner-sphere mechanisms involve electron transfer between the reductant and oxidant through bridging chemical bonds, which entails the breaking and formation of bonds (Stumm, 1995). On the other hand, the outer-sphere mechanism denotes electron transfer in redox reactions without the occurrence of bond breaking or formation (Clegg et al., 2004; Rosso and Rustad, 2000; Rosso and Morgan, 2002). However, the outer-sphere mechanism is less understood. To unravel the detailed mechanism of the redox reactions between Fe-bearing clay minerals and the oxyanions of Se(IV) and Tc(VII), a good understanding of each component is essential, including Fe(II) as the reductant, electron transfer across the interface as the mediator, and the role of oxyanions of Se(IV) and Tc(VII) as the oxidizing agent.

## **1.4 Objectives of the thesis**

The present PhD project focus on investigating the retention of redox-sensitive Se and Tc on Fe(II)/Fe(III)-bearing clay minerals coupled with adsorption and electron transfer interface reaction. Previous studies have revealed that structural Fe(II) in the clay minerals is redox active (Brigatti et al., 2000), and surface-bond Fe(II) on the clay edge sites is also redox active (Charlet et al., 2007).  $\text{TcO}_4^-$  does not adsorb onto Fe-bearing clay minerals, but reduction of Tc(VII) to Tc(IV) has been observed in Fe-bearing clay systems (Peretyazhko et al., 2008b). However, the mechanism by which electrons are transferred from Fe-clay minerals to  $\text{TcO}_4^-$  remains unclear. In contrast, Se(IV) sorption has been observed as outer-sphere and inner-sphere sorption complexes on Fe(II)/Fe(III)-bearing clay minerals

(Fernández-Martínez and Charlet, 2009). Reduced species of Se(IV) have been reported as red and gray elemental Se(0), as well as two iron selenides with structures similar to  $\text{Fe}_7\text{Se}_8$  and  $\text{FeSe}$  (Scheinost et al 2008). However, the factors determining the formation of reduced species remain unknown. Further investigations are needed to unravel the details of these retention processes. Therefore, the objectives of this thesis focus are list below.

- (i) Characterize Fe(II)/Fe(III)-bearing clay minerals, including redox active Fe content, Fe(II) and Fe(III) content, redox potential of clay minerals, and clay structural integrity after chemical reduction.
- (ii) Study the role of structural Fe(II) in Se and Tc retention.
- (iii) Quantify and characterize the influence of the redox reaction on Se and Tc retention, induced by Fe(II)/Fe(III) associated to clay minerals.
- (iv) Investigate the relationship between Se(IV) reduction kinetics and reduced species.

In this project, 2:1 dioctahedral smectite clays with varying structural Fe content were used, Texas montmorillonite STx-1 (0.5 wt% Fe), Wyoming montmorillonite SWy-2 (2.6 wt% Fe), and nontronite clay NAu-2 (20.3 wt% Fe). Clays were reduced chemically by Citrate-Bicarbonate-Dithionite (CBD) method following Stucki et al. to obtain different Fe(II) content (Stucki et al., 1984b). The reduced clays underwent comprehensive characterization, including analysis of mineralogical composition, morphology, structure, Fe(II)/Fe(III) content, redox potential, cation exchange capacity (CEC), and edge sites. Various techniques were employed for these characterizations, such as X-ray diffraction (XRD), transmission electron microscopy (TEM), Mössbauer spectrometry, extended X-ray absorption fine structure (EXAFS) combined with X-ray absorption near edge structure (XANES), mediated electrochemical reduction (MER) and oxidation (MEO), as well as cation  $^{63}\text{Ni}$  and  $^{152}\text{Eu}$  sorption experiments. These characterization results provide deep insights into the properties and behaviors of the reduced clays in relation to their Fe(II)/Fe(III) content, redox state, and sorption capabilities, and provide reliable reference guidelines for measurements in other clay minerals. Batch sorption experiments were conducted under anoxic condition, and XANES and EXAFS analyses were employed to identify the reduced species. The obtained sorption results for Se and Tc retention on Fe(II)/Fe(III)-bearing clay minerals will enrich the data available for thermodynamic sorption models used in safety analysis. Moreover, the insight gained from molecular-scale surface speciation will lead to a more comprehensive understanding of the interaction

between Se, Tc, and the clay surface, thereby contributing to a more accurate prediction of Se and Tc retention in the deep geological repository.

## 1.5 Outline of the thesis

This PhD thesis consists of six chapters. The introduction provides an overview of the entire project, while the main content delves into the objectives in a comprehensive manner. The conclusion summarizes the crucial findings and their significance within the project, also offering insights into potential avenues for future research.

**Chapter 1: Introduction.** It provides an overview of the background, relevant theoretical knowledge, and the main objectives.

**Chapter 2: Oxidation state and structure of Fe in nontronite: from oxidizing to reducing redox conditions.** The preparation and characterization of nontronite, as a representative of the Fe-bearing clay samples, are described in detail. This chapter provides a basis for the study of redox reactions of Se and Tc in the following chapters. The results of this study have been published in *ACS Earth and Space Chemistry* (Qian et al., 2023).

**Chapter 3: Influence of structural Fe content in clay minerals on selenite redox reactions: kinetics and structural transformations.** Various reduced species were observed in the selenite sorption experiments at different time intervals, which indicates a complex relationship between kinetics and the sorption-reduction mechanism. Initially, selenite kinetics experiments were conducted on reduced STx-1, reduced SWy-2, as well as low and high-level reduced NAu-2. Subsequently, the reduced species were identified using EXAFS spectroscopy. The study describes the relationships between the reduced species of selenite and the degree of clay reduction, as well as the reaction time. This chapter has been submitted to *Geochimica et Cosmochimica Acta*.

**Chapter 4: The retention of technetium by Fe-bearing clay minerals.** Pertechetate sorption experiments were performed on reduced STx-1, reduced SWy-2, as well as low and high-level reduced NAu-2. Samples of varying Fe(II) content, different Fe(II) location (structural and surface adsorbed), solution pH, and pertechetate concentration were measured with EXAFS spectroscopy. The study aims to investigate the molecular-scale reduced species at different experiment conditions and understand the reduction mechanism of pertechetate. This chapter is in preparation for publication.



**Chapter 5: Comparison of the retention of Se and Tc.** The retention of Se and Tc were described separately in chapter 3 and chapter 4. This chapter aims to compare the similarities and differences among the major findings concerning the retention of Se and Tc.

**Chapter 6: Conclusions and outlook** – provides a summary of the main works conducted and their findings within the entire project, as well as proposing potential research topics for the future.

## 1.6 References

- Baeyens B. and Marques Fernandes M. (2018) 5 - Adsorption of heavy metals including radionuclides. In *Developments in Clay Science* (eds. R. Schoonheydt, C. T. Johnston and F. Bergaya). Elsevier. pp. 125-172.
- Bergaya F. and Lagaly G. (2006) Chapter 1 General Introduction: Clays, Clay Minerals, and Clay Science. In *Developments in Clay Science* (eds. F. Bergaya, B. K. G. Theng and G. Lagaly). Elsevier. pp. 1-18.
- Bradbury M. H. and Baeyens B. (1997) A mechanistic description of Ni and Zn sorption on Na-montmorillonite Part II: modelling. *Journal of Contaminant Hydrology* **27**, 223-248.
- Bradbury M. H., Berner U., Curti E., Hummel W., Kosakowski G. and Thoenen T. (2014) The long term geochemical evolution of the nearfield of the HLW repository, Nagra Technical Report NTB 12-01, Nagra, Wettingen, Switzerland.
- Brigatti M. F., Lugli C., Cibir G., Marcelli A., Giuli G., Paris E., Mottana A. and Wu Z. (2000) Reduction and Sorption of Chromium by Fe(II)-Bearing Phyllosilicates: Chemical Treatments and X-Ray Absorption Spectroscopy (XAS) Studies. *Clays and Clay Minerals* **48**, 272-281.
- Chandra A. (1999) A theoretical study of outersphere electron transfer reactions in electrolyte solutions. *The Journal of Chemical Physics* **110**, 1569-1580.
- Charlet L., Tournassat C., Grenèche J.-M., Wersin P., Géhin A. and Hadi J. (2022) Mössbauer spectrometry insights into the redox reactivity of Fe-bearing phases in the environment. *Journal of Materials Research* 10.1557/s43578-022-00823-8.
- Charlet L., Kang M., Bardelli F., Kirsch R., Géhin A., Grenèche J.-M. and Chen F. (2012) Nanocomposite Pyrite–Greigite Reactivity toward Se(IV)/Se(VI). *Environmental Science & Technology* **46**, 4869-4876.
- Charlet L., Scheinost A. C., Tournassat C., Grenèche J.-M., Géhin A., Fernandez-Martinez A., Coudert S., Tisserand D. and Brendle J. (2007) Electron transfer at the mineral/water interface: Selenium reduction by ferrous iron sorbed on clay. *Geochimica et Cosmochimica Acta* **71**, 5731–5749.
- Childs B. C., Lawler K. V., Braband H., Mast D. S., Bigler L., Stalder U., Peterson D. R., Jansen A., Forster P. M., Czerwinski K. R., Alberto R., Sattelberger A. P. and Poineau F. (2018) The Nature of the Technetium Species Formed During the Oxidation of Technetium Dioxide with Oxygen and Water. *European Journal of Inorganic Chemistry* **2018**, 1137-1144.
- Clegg A. D., Rees N. V., Klymenko O. V., Coles B. A. and Compton R. G. (2004) Marcus Theory of Outer-Sphere Heterogeneous Electron Transfer Reactions: Dependence of the Standard Electrochemical Rate Constant on the Hydrodynamic Radius from High Precision Measurements of the Oxidation of Anthracene and Its Derivatives in Nonaqueous Solvents Using the High-Speed Channel Electrode. *Journal of the*

*American Chemical Society* **126**, 6185-6192.

- Curti E., Aimoz L. and Kitamura A. (2013) Selenium uptake onto natural pyrite. *Journal of Radioanalytical and Nuclear Chemistry* **295**, 1655-1665.
- Curti E., Puranen A., Grolimund D., Jädernas D., Sheptyakov D. and Mesbah A. (2015) Characterization of selenium in UO<sub>2</sub> spent nuclear fuel by micro X-ray absorption spectroscopy and its thermodynamic stability. *Environmental Science: Processes & Impacts* **17**, 1760-1768.
- Drits V. A. and Manceau A. (2000) A Model for the Mechanism of Fe<sup>3+</sup> to Fe<sup>2+</sup> Reduction in Dioctahedral Smectites. *Clays and Clay Minerals* **48**, 185-195.
- Fan D., Anitori R. P., Tebo B. M., Tratnyek P. G., Lezama Pacheco J. S., Kukkadapu R. K., Engelhard M. H., Bowden M. E., Kovarik L. and Arey B. W. (2013) Reductive Sequestration of Pertechnetate (99TcO<sub>4</sub><sup>-</sup>) by Nano Zerovalent Iron (nZVI) Transformed by Abiotic Sulfide. *Environmental Science & Technology* **47**, 5302-5310.
- Fernández-Martínez A. and Charlet L. (2009) Selenium environmental cycling and bioavailability: a structural chemist point of view. *Reviews in Environmental Science and Bio/Technology* **8**, 81-110.
- Goldberg S. (2002) Competitive adsorption of arsenate and arsenite on oxides and clay minerals. *Soil Science Society of America Journal* **66**, 413-421.
- Gorski C. A., Klupfel L., Voegelin A., Sander M. and Hofstetter T. B. (2012a) Redox properties of structural Fe in clay minerals. 2. Electrochemical and spectroscopic characterization of electron transfer irreversibility in ferruginous smectite, SWa-1. *Environ Sci Technol* **46**, 9369-9377.
- Gorski C. A., Klupfel L. E., Voegelin A., Sander M. and Hofstetter T. B. (2013) Redox properties of structural Fe in clay minerals: 3. Relationships between smectite redox and structural properties. *Environ Sci Technol* **47**, 13477-13485.
- Gorski C. A., Aeschbacher M., Soltermann D., Voegelin A., Baeyens B., Marques Fernandes M., Hofstetter T. B. and Sander M. (2012b) Redox properties of structural Fe in clay minerals. 1. Electrochemical quantification of electron-donating and -accepting capacities of smectites. *Environ Sci Technol* **46**, 9360-9368.
- Heinze K. (2004) Comprehensive Coordination Chemistry II. 10-volume set. Edited by Jon A. McCleverty and Thomas J. Meyer. *Angewandte Chemie International Edition* **43**, 3875-3876.
- Hynes J. T. (1986) Outer-sphere electron-transfer reactions and frequency-dependent friction. *The Journal of Physical Chemistry* **90**, 3701-3706.
- IAEA (2003) *Scientific and Technical Basis for the Geological Disposal of Radioactive Wastes*. INTERNATIONAL ATOMIC ENERGY AGENCY, Vienna.
- Ifeoma Mary U. and Onyedikachi Anthony I. (2019) Sorption of Heavy Metals on Clay

Minerals and Oxides: A Review. In *Advanced Sorption Process Applications* (ed. E. Serpil). IntechOpen, Rijeka. p. Ch. 7.

- Jaisi D. P., Dong H. and Morton J. P. (2008a) Partitioning of Fe(II) in reduced nontronite (NAu-2) to reactive sites: Reactivity in terms of Tc(VII) reduction. *Clays and Clay Minerals* **56**, 175-189.
- Jaisi D. P., Dong H., Plymale A. E., Fredrickson J. K., Zachara J. M., Heald S. and Liu C. (2009) Reduction and long-term immobilization of technetium by Fe(II) associated with clay mineral nontronite. *Chemical Geology* **264**, 127-138.
- Joe-Wong C., Brown Jr G. E. and Maher K. (2017) Kinetics and products of chromium (VI) reduction by iron (II/III)-bearing clay minerals. *Environmental science & technology* **51**, 9817-9825.
- Jordan N., Lomenech C., Marmier N., Giffaut E. and Ehrhardt J.-J. (2009) Sorption of selenium(IV) onto magnetite in the presence of silicic acid. *Journal of Colloid and Interface Science* **329**, 17-23.
- Komadel P., Madejová J. and Stucki J. W. (2006) Structural Fe(III) reduction in smectites. *Applied Clay Science* **34**, 88-94.
- Lin Z. and Puls R. (2000) Adsorption, desorption and oxidation of arsenic affected by clay minerals and aging process. *Environmental Geology* **39**, 753-759.
- Liu J., Pearce C. I., Qafoku O., Arenholz E., Heald S. M. and Rosso K. M. (2012) Tc(VII) reduction kinetics by titanomagnetite (Fe<sub>3</sub>-xTi<sub>x</sub>O<sub>4</sub>) nanoparticles. *Geochimica et Cosmochimica Acta* **92**, 67-81.
- Liu X., Tournassat C., Grangeon S., Kalinichev A. G., Takahashi Y. and Marques Fernandes M. (2022) Molecular-level understanding of metal ion retention in clay-rich materials. *Nature Reviews Earth & Environment* **3**, 461-476.
- Manceau A., Drits V. A., Lanson B., Chateigner D., Wu J., Huo D., Gates W. P. and Stucki J. W. (2000) Oxidation-reduction mechanism of iron in dioctahedral smectites: II. Crystal chemistry of reduced Garfield nontronite. *American Mineralogist* **85**, 153-172.
- McGinnes D. F. (2002) Model Radioactive Waste Inventory for Reprocessing Waste and Spent Fuel Nagra Technical Report NTB 01-01, Nagra, Wettingen, Switzerland.
- Meena A. H. and Arai Y. (2017) Environmental geochemistry of technetium. *Environmental Chemistry Letters* **15**, 241-263.
- Missana T., Alonso U. and García-Gutiérrez M. (2009) Experimental study and modelling of selenite sorption onto illite and smectite clays. *Journal of Colloid and Interface Science* **334**, 132-138.
- Mohapatra D., Mishra D., Chaudhury G. R. and Das R. P. (2007) Arsenic adsorption mechanism on clay minerals and its dependence on temperature. *Korean Journal of Chemical Engineering* **24**, 426-430.

- Muller I. S., McKeown D. A. and Pegg I. L. (2014) Structural Behavior of Tc and I Ions in Nuclear Waste Glass. *Procedia Materials Science* **7**, 53-59.
- Myneni S. C. B., Tokunaga T. K. and Brown G. E. (1997) Abiotic Selenium Redox Transformations in the Presence of Fe(II,III) Oxides. *Science* **278**, 1106-1109.
- Nagra (2002) Demonstration of disposal feasibility for spent fuel, vitrified high-level waste and long-lived intermediate-level waste, Nagra Technical Report NTB 02-05, Nagra, Wettingen, Switzerland.
- Nagra (2013) Redox properties of iron-bearing clays and MX-80 bentonite – Electrochemical and spectroscopic characterization, Technical Report NTB 13-03, Nagra, Wettingen, Switzerland.
- Neumann A., Petit S. and Hofstetter T. B. (2011) Evaluation of redox-active iron sites in smectites using middle and near infrared spectroscopy. *Geochimica et Cosmochimica Acta* **75**, 2336-2355.
- Pearce C. I., Liu J., Baer D. R., Qafoku O., Heald S. M., Arenholz E., Grosz A. E., McKinley J. P., Resch C. T., Bowden M. E., Engelhard M. H. and Rosso K. M. (2014) Characterization of natural titanomagnetites ( $\text{Fe}_{3-x}\text{TixO}_4$ ) for studying heterogeneous electron transfer to Tc(VII) in the Hanford subsurface. *Geochimica et Cosmochimica Acta* **128**, 114-127.
- Pepper S. E., Bunker D. J., Bryan N. D., Livens F. R., Charnock J. M., Patrick R. A. and Collison D. (2003) Treatment of radioactive wastes: An X-ray absorption spectroscopy study of the reaction of technetium with green rust. *Journal of colloid and Interface Science* **268**, 408-412.
- Peretyazhko T., Zachara J. M., Heald S. M., Kukkadapu R. K., Liu C., Plymale A. E. and Resch C. T. (2008a) Reduction of Tc(VII) by Fe(II) Sorbed on Al (hydr)oxides. *Environmental Science & Technology* **42**, 5499-5506.
- Peretyazhko T., Zachara J. M., Heald S. M., Jeon B. H., Kukkadapu R. K., Liu C., Moore D. and Resch C. T. (2008b) Heterogeneous reduction of Tc(VII) by Fe(II) at the solid–water interface. *Geochimica et Cosmochimica Acta* **72**, 1521-1539.
- Poineau F., Mausolf E., Jarvinen G. D., Sattelberger A. P. and Czerwinski K. R. (2013) Technetium Chemistry in the Fuel Cycle: Combining Basic and Applied Studies. *Inorganic Chemistry* **52**, 3573-3578.
- Pusch R. (2006) Chapter 6 Mechanical Properties of Clays and Clay Minerals. In *Developments in Clay Science* (eds. F. Bergaya, B. K. G. Theng and G. Lagaly). Elsevier. pp. 247-260.
- Qian Y., Scheinost A. C., Grangeon S., Greneche J.-M., Hoving A., Bourhis E., Maubec N., Churakov S. V. and Fernandes M. M. (2023) Oxidation State and Structure of Fe in Nontronite: From Oxidizing to Reducing Conditions. *ACS Earth and Space Chemistry* **7**, 1868-1881.
- Rai D., Eary L. E. and Zachara J. M. (1989) Environmental chemistry of chromium. *Science*

- Rosso K. M. and Rustad J. R. (2000) Ab Initio Calculation of Homogeneous Outer Sphere Electron Transfer Rates: Application to  $M(OH_2)_6^{3+/2+}$  Redox Couples. *The Journal of Physical Chemistry A* **104**, 6718-6725.
- Rosso K. M. and Morgan J. J. (2002) Outer-sphere electron transfer kinetics of metal ion oxidation by molecular oxygen. *Geochimica et Cosmochimica Acta* **66**, 4223-4233.
- Sander M., Hofstetter T. B. and Gorski C. A. (2015) Electrochemical Analyses of Redox-Active Iron Minerals: A Review of Nonmediated and Mediated Approaches. *Environmental Science & Technology* **49**, 5862-5878.
- Sattelberger A. P., Scott B. L. and Poineau F. (2005) Technetium Organometallics. In *Comprehensive Organometallic Chemistry III* (eds. D. M. P. Mingos and R. H. Crabtree). Elsevier, Oxford. pp. 833-854.
- Schaefer M. V., Gorski C. A. and Scherer M. M. (2011) Spectroscopic Evidence for Interfacial Fe(II)–Fe(III) Electron Transfer in a Clay Mineral. *Environmental Science & Technology* **45**, 540-545.
- Scheinost A. C. and Charlet L. (2008) Selenite reduction by mackinawite, magnetite and siderite: XAS characterization of nanosized redox products. *Environmental science & technology* **42**, 1984-1989.
- Scheinost A. C., Kirsch R., Banerjee D., Fernandez-Martinez A., Zaenker H., Funke H. and Charlet L. (2008) X-ray absorption and photoelectron spectroscopy investigation of selenite reduction by FeII-bearing minerals. *Journal of Contaminant Hydrology* **102**, 228-245.
- Schuette R., Goodman B. A. and Stucki J. W. (2000) Magnetic properties of oxidized and reduced smectites. *Physics and Chemistry of Minerals* **27**, 251-257.
- Sellin P. and Leupin O. X. (2013) The Use of Clay as an Engineered Barrier in Radioactive-Waste Management a Review. *Clays and Clay Minerals* **61**, 477-498.
- Soltermann D. (2014) Ferrous iron uptake mechanisms at the montmorillonite-water interface under anoxic and electrochemically reduced conditions. ETH Zurich.
- Soltermann D., Baeyens B., Bradbury M. H. and Marques Fernandes M. (2014a) Fe(II) uptake on natural montmorillonites. II. Surface complexation modeling. *Environ Sci Technol* **48**, 8698-8705.
- Soltermann D., Marques Fernandes M., Baeyens B., Dahn R., Joshi P. A., Scheinost A. C. and Gorski C. A. (2014c) Fe(II) uptake on natural montmorillonites. I. Macroscopic and spectroscopic characterization. *Environ Sci Technol* **48**, 8688-8697.
- Stucki J. and Roth C. (1977) Oxidation - reduction mechanism for structural iron in nontronite. *Soil Science Society of America Journal* **41**, 808-814.
- Stucki J. W. (2006) Chapter 8 Properties and Behaviour of Iron in Clay Minerals. In

- Developments in Clay Science* (eds. F. Bergaya, B. K. G. Theng and G. Lagaly). Elsevier. pp. 423-475.
- Stucki J. W., Golden D. C. and Roth C. B. (1984b) Effects of Reduction and Reoxidation of Structural Iron on the Surface Charge and Dissolution of Dioctahedral Smectites. *Clays and Clay Minerals* **32**, 350-356.
- Stumm W. (1995) The Inner-Sphere Surface Complex. In *Aquatic Chemistry*. American Chemical Society. pp. 1-32.
- Tournassat C., Bourg I. C., Steefel C. I. and Bergaya F. (2015) Chapter 1 - Surface Properties of Clay Minerals. In *Developments in Clay Science* (eds. C. Tournassat, C. I. Steefel, I. C. Bourg and F. Bergaya). Elsevier. pp. 5-31.
- Vuori S. (1995) The environmental and ethical basis of the geological disposal of long-lived radioactive waste; Ydinjätteiden geologinen loppusijoitus. Ympäristösuojelulliset ja eettiset perusteet. *ATS Ydintekniikka* **24**.
- W. Hummel T. T. (2023) The PSI chemical thermodynamic database 2020, Nagra Technical Report NTB 21-03, Nagra, Wettingen, Switzerland.
- Wagner J. F. (2013) Chapter 9 - Mechanical Properties of Clays and Clay Minerals. In *Developments in Clay Science* (eds. F. Bergaya and G. Lagaly). Elsevier. pp. 347-381.
- Wersin P., Johnson L. H., Schwyn B., Berner U. and Curti E. (2003) Redox Conditions in the Near Field of a Repository for SF/HLW and ILW in Opalinus Clay, Nagra Technical Report NTB 02-13, Nagra, Wettingen, Switzerland.
- Wharton M., Atkins B., Charnock J., Livens F., Patrick R. and Collison D. (2000) An X-ray absorption spectroscopy study of the coprecipitation of Tc and Re with mackinawite (FeS). *Applied Geochemistry* **15**, 347-354.
- Zachara J., Cowan C., Schmidt R. and Ainsworth C. (1988) Chromate adsorption by kaolinite. *Clays and Clay Minerals* **36**, 317-326.
- Zachara J. M., Heald S. M., Jeon B.-H., Kukkadapu R. K., Liu C., McKinley J. P., Dohnalkova A. C. and Moore D. A. (2007) Reduction of pertechnetate [Tc(VII)] by aqueous Fe(II) and the nature of solid phase redox products. *Geochimica et Cosmochimica Acta* **71**, 2137-2157.

**Chapter 2: Oxidation state and structure of Fe in  
nontronite: from oxidizing to reducing conditions**

*This chapter has been published in ACS Earth and Space Chemistry. DOI:  
10.1021/acsearthspacechem.3c00136*



# Oxidation state and structure of Fe in nontronite: from oxidizing to reducing conditions

Yanting Qian<sup>1,2</sup>, Andreas C. Scheinost<sup>3a,b,\*</sup>, Sylvain Grangeon<sup>4</sup>, Jean-Marc Greneche<sup>5</sup>, Alwina Hoving<sup>6</sup>, Eric Bourhis<sup>7</sup>, Nicolas Maubec<sup>4</sup>, Sergey V. Churakov<sup>1,2</sup>, Maria Marques Fernandes<sup>1,\*</sup>,

<sup>1</sup>Laboratory for Waste Management, Paul Scherrer Institut, CH-5232 Villigen PSI, Switzerland

<sup>2</sup>Institute for Geological Sciences, University of Bern, CH-3012 Bern, Switzerland

<sup>3a</sup>The Rossendorf Beamline at the European Synchrotron Radiation Facility (ESRF), Avenue des Martyrs 71, 38043, Grenoble, France

<sup>3b</sup>Helmholtz Zentrum Dresden Rossendorf, Institute of Resource Ecology, Bautzner Landstrasse 400, 01328, Dresden, Germany

<sup>4</sup>BRGM – French Geological Survey, 45060 Orléans, France

<sup>5</sup>Institut des Molécules et Matériaux du Mans IMMM UMR CNRS 6283, Le Mans Université, 72085, Le Mans Cedex 9, France

<sup>6</sup>TNO Geological Survey of the Netherlands, PO Box 80015, 3508 TA Utrecht, the Netherlands

<sup>7</sup>Interfaces, Confinement, Matériaux et Nanostructures (ICMN), CNRS/Université d'Orléans, UMR 7374, 1b rue de la Férollerie, CS 40059, 45071 Orléans, France

\*Corresponding author.

E-mail address: [maria.marques@psi.ch](mailto:maria.marques@psi.ch); [scheinost@esrf.fr](mailto:scheinost@esrf.fr);

## Abstract

The redox reaction between natural Fe-containing clay minerals and its sorbates is a fundamental process controlling the cycles of many elements such as carbon, nutrients, redox-sensitive metals, and metalloids (e.g., Co, Mn, As, Se), and inorganic as well as organic pollutants in Earth's critical zone. While the structure of natural clay minerals under oxic conditions is well known, less is known about their behavior under anoxic and reducing conditions, thereby impeding a full understanding of the mechanisms of clay-driven reduction and oxidation (redox) reactions especially under reducing conditions. Here we investigate the structure of a ferruginous natural clay smectite, nontronite, under different redox conditions, and compare several methods for the determination of iron redox states.

Iron in nontronite was gradually reduced chemically with the Citrate-Bicarbonate-Dithionite (CBD) method. <sup>57</sup>Fe Mössbauer spectrometry, X-ray Photoelectron Spectroscopy (XPS), X-ray Absorption Near Edge Structure (XANES) spectroscopy including its pre-edge, Extended X-ray Absorption Fine Structure (EXAFS) spectroscopy, and Mediated Electrochemical Oxidation and Reduction (MEO/MER), provided consistent Fe(II)/Fe(III) ratios. By combining X-Ray Diffraction (XRD) and Transmission Electron Microscopy (TEM), we show that the long-range structure of nontronite at the highest obtained reduction degree of 44% Fe(II) is not different from that of fully oxidized nontronite except for a slight basal plane dissolution on the external surfaces. The short-range order probed by EXAFS spectroscopy suggests, however, an increasing structural disorder and Fe clustering with increasing reduction of structural Fe.

Keywords: Nontronite; Iron reduction; Structure; Fe redox state; Quantitative spectroscopy measurement

## 2.1 Introduction

In the critical zone, Fe(hydr)oxide minerals and Fe-bearing phyllosilicates play a fundamental role in controlling the mobility and bioavailability of several elements and molecules.<sup>1</sup> While alternating redox conditions induced e.g. by fluctuations in the water table or by cycles of organic matter input/degradation often cause the (complete) dissolution and re-precipitation of Fe(hydr)oxides, structural Fe in phyllosilicate may change its oxidation state repeatedly while maintaining essentially the structural integrity of its host phase.<sup>2</sup> Thereby, Fe-bearing clay minerals act as redox batteries, playing important roles e.g. in the natural carbon cycle, for nutrient availability, and for the mobility and toxicity of organic and inorganic pollutants.<sup>3,4</sup> Ferric iron in minerals potentially limits organic matter mineralization in floodplains and thus sustains the ecosystem.<sup>5,6</sup> Fe-bearing clay minerals efficiently retain pesticides,<sup>7,8</sup> phosphates,<sup>9,10</sup> organic contaminants,<sup>11-13</sup> and heavy metals.<sup>14-17</sup> Fe-bearing clay minerals used as engineered barriers and backfill in radioactive waste repositories are critical for immobilizing redox sensitive radionuclides, such as uranium,<sup>18-22</sup> neptunium,<sup>23,24</sup> technetium,<sup>25-28</sup> and selenium.<sup>29,30</sup> Iron redox reactions are involved in all these processes. The Fe(II)/Fe(III) ratio in clay minerals, its structural position and the ability to participate in redox-reactions are the key parameters necessary for the understanding and the modelling the redox-controlled retention processes.<sup>31</sup> In contrast to

iron (hydr)oxides, the geochemical behavior of natural Fe-bearing clay minerals is much less understood due to their diversity in composition and structure. In this study, we combine several microscopic and spectroscopic techniques to shed light on the behavior of iron in a typical Fe-rich smectite clay mineral, nontronite, under varying redox conditions.

Nontronite has a 2:1 layer structure and each layer is composed of an octahedral (O) sheet sandwiched between two tetrahedral (T) sheets, known as the TOT layer. In dioctahedral clays, two-thirds of the octahedral sites are occupied by mostly trivalent cations, while in trioctahedral clays, all octahedral sites are occupied by mostly divalent cations. Octahedra with hydroxyl groups on opposing sides are labelled trans (M1) sites, while octahedra with hydroxyl groups on the same sides are labelled cis (M2) sites. Nontronite belongs to the dioctahedral group of Fe-bearing clay minerals,<sup>32</sup> hence one-third of the cation sites in the octahedral sheets are vacant. The distribution of octahedral cations and vacancies in these sheets generates different octahedral orderings and thus different physical and chemical properties of the clay minerals.<sup>33</sup> Therefore, a well-defined clay structure is the basis for any clay relevant research. While the octahedral ordering has been studied in the past, it is still debated because of the difficulty to obtain accurate structural configurations by experimental methods like TEM and XRD due to nanoscale particle size and the turbostratic stacking of the layers of these swelling clays. Based on <sup>57</sup>Fe Mössbauer, infrared and X-ray absorption spectroscopies, as well as X-ray diffraction,<sup>34-41</sup> and theoretical simulation,<sup>42</sup> it has been established that octahedral sheets of Fe-rich clays are trans-vacant (M1 vacant or centrosymmetric structure), while the octahedral sheets of Fe-poor clays are cis-vacant (M2 vacant or non-centrosymmetric structure).<sup>33</sup>

In addition to octahedral ordering, Fe reduction in the clay requires charge compensation mechanisms to balance the decreased positive charge, which may lead to additional structural changes. Stucki et al. proposed a structural dehydroxylation induced by the pH-buffered dithionite reduction method<sup>43</sup> and observed Fe, Si, and Al dissolution during clay reduction.<sup>44</sup> Manceau et al. stated that Fe remains in six-fold coordination as it is reduced to Fe(II) and that the Fe(II) cations migrate from cis-sites to neighboring empty trans-sites and possibly form trioctahedral clusters in the otherwise dioctahedral nontronite structure.<sup>45</sup> The mechanisms have been linked to local structure instabilities followed by structural rearrangements. Such structural change is likely to alter octahedral ordering, but no direct evidence of the structural transformation has yet been reported and little is known about the influence of the degree of clay reduction on clay surfaces and structures.

Powerful structural characterization methods are a prerequisite to investigate such structural alterations. Powder X-ray diffraction (XRD) provides structural, textural, and morphological information on mineral phases. Due to the presence of turbostratism, XRD patterns of swelling clays show only  $00l$  and unresolved  $hk$  reflections. While this can be quantitatively accounted for in powder XRD, this is less easy in single crystal XRD. In contrast to the long-range order sensitivity of XRD, Extended X-ray Absorption Fine Structure (EXAFS) spectroscopy probes the short-range order around the absorbing element within a few Angstrom distance. Extended Transmission Electron Microscopy (TEM) is used to visualize the morphology and microstructure in clay minerals. Due to advances in resolution and sample preparation methods,<sup>46</sup> it is now possible to acquire direct information on the structure of clay minerals at an atomic level.<sup>47</sup> In addition to structural information and morphology, there is also a great demand for accurate and quantitative measurements of Fe(II) and Fe(III) content, especially for the studies of redox reactions. Currently, Mössbauer spectrometry, X-ray Photoelectron Spectroscopy (XPS), X-ray Absorption Near Edge Structure (XANES) spectroscopy, and Mediated Electrochemical Oxidation and Reduction (MEO/MER) have been developed for this purpose. Mössbauer spectroscopy probes the core of Fe, while XAS probes excitations from core to valence bands. The analysis by XPS is surface sensitive since restricted to the topmost 2-10 nm of a sample, while the hard X-rays employed for XANES and EXAFS penetrate even at the relatively low energy of the Fe K-edge (7.112 keV) tens of microns thereby probing rather the bulk of a sample; MEO/MER measures the electron donating and accepting capacities of the sample through chemical reactions. Each method has its strengths and limitations, but a direct benchmarking of the different methods for Fe(II)/Fe(III) quantification has to the best of our knowledge never been performed.

In this study, we conducted clay reduction experiments in the aqueous phase and applied XRD, TEM, Mössbauer spectrometry, XPS, XANES, EXAFS and MEO/MER to 1) study the clay dissolution in the reduction process, 2) reveal the structure of nontronite and 3) compare the results of four spectroscopic and one chemical method for the measurement of the Fe redox state as a function of increasing reduction by CBD. Based on this analysis we provide a reliable structural characterization of nontronite and provide reference guidelines for the redox state measurements of iron in clay minerals.

## 2.2 Materials and methods

All clay preparation and reduction steps as well as the preparation of samples for the different analytical methods were conducted in an anoxic glovebox under controlled N<sub>2</sub> atmosphere (O<sub>2</sub> < 0.1 ppm).

### 2.2.1 Clays and clay reduction by Citrate-Bicarbonate-Dithionite

The nontronite clay NAu-2 was obtained from the Clay Source Repository of the Clay Minerals Society (Purdue University, West Lafayette, IN). The chemical composition in wt.-% of NAu-2 raw material given by the clay mineral society is: SiO<sub>2</sub> 56.99, Al<sub>2</sub>O<sub>3</sub> 3.4, Fe<sub>2</sub>O<sub>3</sub> 37.42, MgO 0.34, CaO 2.67, Na<sub>2</sub>O 0.11, K<sub>2</sub>O 0.02, and its chemical formula is (M<sup>+</sup><sub>0.97</sub>)[Si<sub>7.57</sub>Al<sub>0.01</sub>Fe<sub>0.42</sub>][Al<sub>0.52</sub>Fe<sub>3.32</sub>Mg<sub>0.7</sub>]O<sub>20</sub>(OH)<sub>4</sub>.<sup>48</sup> According to several sources, the Fe content varies between 21 and 38 wt%.<sup>49</sup> In our study, the Fe content of native NAu-2 is 22 wt% as determined by X-Ray Fluorescence (XRF). The raw clay was subjected to washing, purification and sedimentation treatments to obtain a homogeneous, single-phased Na-form clay suspension with ≤ 0.5 μm Stokes diameter. The treatment includes the following steps: peptisation with deionised water, cation exchange with 1 M NaCl to obtain the Na form, pre-equilibration in the respective clay-water, centrifugation to obtain particles with a Stokes radius ≤ 0.5 μm, flocculation with 1 M NaCl, removal of acid soluble impurities by an acid treatment at pH=3, and finally conversion to 0.1 M NaCl background electrolyte. This treatment largely follows the method published by Baeyens et al. except for replacing NaClO<sub>4</sub> by NaCl.<sup>50</sup>

**Clay dissolution experiment.** The purified nontronite was reduced by the Citrate-Bicarbonate-Dithionite (CBD) method essentially following Stucki et al., however without heating.<sup>51</sup> Different degrees of reduction were obtained by adding different amounts of dithionite, while all other experimental conditions were kept the same. 7 mL of nontronite clay suspension (dry weight: 20.29 g/L) were first mixed with a citrate-bicarbonate (CB) buffer solution (0.4 ml of 0.5 M Na<sub>3</sub>C<sub>6</sub>H<sub>5</sub>O<sub>7</sub>·2H<sub>2</sub>O and 5.6 ml of 1 M NaHCO<sub>3</sub>) in centrifuge tubes for about an hour. A total of fourteen samples with varying degree of reduction were obtained by adding the following amounts of dithionite (Na<sub>2</sub>S<sub>2</sub>O<sub>4</sub>): 0 g, 0.01 g, 0.02 g, 0.05 g, 0.1 g, 0.15 g, 0.2 g, 0.25 g, 0.3 g, 0.35 g, 0.43 g, 0.55 g, 0.8 g, 1.0 g. The tubes were filled with degassed 0.1 M NaCl solution up to 24 ml. The reduction process took about 24 hours under continuous upside-down shaking. The clay suspensions were then centrifuged without additional washing step to separate the clay fraction from the supernatant, which was collected for ICP-OES measurement at neutral pH. The absolute amount of element X

dissolved ( $X_{\text{dis}}$ ) ( $\mu\text{mol/g}$ ) was calculated according to equation 2.1. The percentage of normalized element X released ( $X_{\%}$ ) (%) was calculated with equation 2.2.

$$X_{\text{dis}} = C_x \cdot V / M_x / m \quad (2.1)$$

$$X_{\%} = C_x \cdot V / (M \cdot n_x) \cdot 100 \quad (2.2)$$

where  $C_x$  (ppm or mg/L) is the concentration of dissolved element X in the supernatant measured by ICP-OES;  $V$  (L) is the volume of the solution;  $M$  (kg/mol) is the molar mass of X;  $m$  (g) is the mass of the clay mineral;  $n_x$  is the total mole amount ( $\mu\text{mol}$ ) of X in nontronite.

**Low-reduced and high-reduced N Au-2 samples.** Larger quantities were prepared at only two degrees of reduction for the different characterization methods, following the same reduction method as before.<sup>51</sup> Two air-tight glass bottles with 500 ml nontronite clay suspension (dry weight: 18.09 g/L, 9 g clay in total, 0.03 mol Fe) were first mixed with a CB-buffer solution (12 ml of 0.5 M  $\text{Na}_3\text{C}_6\text{H}_5\text{O}_7 \cdot 2\text{H}_2\text{O}$  and 163 ml of 1 M  $\text{NaHCO}_3$ ) for about an hour. After equilibrium with CB-buffer, the dithionite powder was added to the clay suspension. For the “high-reduced” sample (high-red N Au-2), we added 27 g of dithionite, which represents three times the mass of clay, corresponding to a molar ratio S/Fe of 10. For the “low-reduced” sample (low-red N Au-2), we added 1.3 g of dithionite, which corresponds to a molar ratio S/Fe = 0.5. The bottles were then filled with degassed 0.1 M NaCl solution to a volume of 700 ml. The clay suspensions were stirred for one day. After the reduction step, the clay suspensions were transferred into dialysis bags and washed first with 1 M NaCl at pH 4 to remove the added chemicals and dissolved elements which could be re-adsorbed onto the clay surface, and then with 0.1 M NaCl without pH adjustment to bring the clay suspension to a 0.1 M NaCl matrix. The washing process was considered to be complete when the concentration of citrate and bicarbonate in the conditioning solution were lower than  $10^{-9}$  mol/L. Reduced clay suspensions were stored in air-tight glass bottles covered by aluminum foil in the glove box. High-red N Au-2 was blue-green and low-red N Au-2 was green after reduction (Figure S1). Even though the glovebox atmosphere contained still up to 0.1 ppm  $\text{O}_2$ , the limited headspace of the bottles would restrict re-oxidation of structural Fe in the clay to  $2.4 \cdot 10^{-7}\%$ .

### 2.2.2 X-ray diffraction

All the sample preparation steps were conducted in the glovebox. The clay suspensions were filtered (cut-off diameter of 0.1  $\mu\text{m}$ ), washed with ethanol and crushed with a mortar to produce a powder of dry material that was inserted in a polyimide capillary (internal

diameter: 1.47 mm; wall thickness: 0.05 mm) and the capillary was sealed on both sides using wax. The airtight capillary was then taken out of the glove box and loaded into a Bruker D8 Advance diffractometer equipped with a Mo anode ( $\lambda = 0.7107 \text{ \AA}$ ) and a LynxEye SE detector. Diffraction data were collected in the  $4\text{-}130^\circ$   $2\theta$  range, in continuous scan mode, and averaged every  $0.03^\circ$   $2\theta$ . Total collection time was 23 h. No color change was observed between the initial and final sample, confirming the conservation of the original Fe oxidation state during the measurement. To further check that the sample preparation did not lead to partial sample oxidation, the same procedure was applied to a green rust samples with very fast oxidation kinetics, even at low  $\text{P}_{\text{O}_2}$ , and no change in color and XRD pattern was observed between the initial sample and the same after this sample collection procedure (data not shown).

### 2.2.3 Transmission electron microscopy

Transmission electron microscopy (TEM) experiments were performed using a Philips CM 20 operated at 200 kV. The clay suspensions were filtered in the glovebox (cut-off diameter of  $0.1 \text{ }\mu\text{m}$ ), washed with ethanol and crushed with a mortar to produce a powder of dry material, which was embedded in resin (Agar 100) and left for polymerization at  $60^\circ\text{C}$  for 1-2 days, under anoxic conditions. The hardened resin was then sliced to produce 60-80 nm thick sections that were mounted on lacey carbon films loaded on Cu grids. This procedure was previously applied to study samples prone to Fe oxidation (feitknechte, <sup>52</sup> green rust<sup>53</sup>). In these studies, no trace of oxidation was observed.

### 2.2.4 $^{57}\text{Fe}$ Mössbauer spectrometry

Mössbauer spectra were recorded at 300 K and 77 K, using a constant acceleration spectrometer (driving unit supplied by WissEl GmbH, Germany), a  $^{57}\text{Co}$  source dispersed in a Rh matrix and a bath cryostat. The velocity of the spectrometer was calibrated using an  $\alpha\text{-Fe}$  foil at 300K. The Mössbauer sample, consisting of a thin layer containing  $5 \text{ mg/cm}^2$  Fe, was prepared in the glove box and the holder then sealed for transport to the instrumental facilities. The sample holder was under He gas at 77 K and in vacuum at 300 K during the measurement. Identical spectra were obtained during repeated measurements, hence sample oxidation during the measurements can be excluded. The values of the hyperfine parameters were refined using a least squares fitting procedure (MOSFIT, unpublished software, Le Mans Université, France) with independent quadrupole doublets composed of Lorentzian lines. Isomer shift (I.S.) are reported relative to that of an  $\alpha\text{-Fe}$  spectrum obtained at RT. Since the f-Lamb-Mössbauer factors, which correspond to the fraction of gamma rays

emitted and absorbed without recoil, are assumed to be identical for the different phases present in the samples and for the different Fe species present in the same phase, the proportions of each Fe species are proportional to the relative spectral area.

### **2.2.5 X-ray photoelectron spectroscopy**

XPS measurements were performed in an ESCALAB Xi+ X-ray photoelectron spectrometer (ThermoScientific) employing a monochromated Al K $\alpha$  X-ray source ( $h\nu = 1486.6$  eV). High-resolution spectra were collected using an analysis area of  $650 \times 650 \mu\text{m}^2$  and a 20 eV pass energy. The C(1s) level (284.8 eV) was taken as the reference binding energy. The sample was prepared by suspending an aliquot of the nontronite sample in  $\sim 1$  mL bi-distilled water inside the glove box, agitated by hand, and then pipetting an aliquot of 0.5 mL of the suspension onto a carbon sample holder. The suspension was then dried at 35 °C in an oven in the glovebox. The dried sample was sealed in an air-tight jar, itself sealed in an air-tight aluminum bag. It was then taken out of the glove box, and opened just before being positioned in the measurement apparatus, where it was immediately subjected to vacuum conditions. A charge neutralizer was used for data collection, being monitored using the C(1s) signal corresponding to adventitious carbon.<sup>54, 55</sup> C(1s), Fe(2p), O(1s), Si(2p) spectra were collected and fitted using the Avantage software (ThermoScientific) via a Lorentzian-Gaussian peak with a default value of 30% Lorentzian contribution, and a smart background removal was used for all spectra.

### **2.2.6 XANES and EXAFS sample preparation and spectra collection**

The Fe-K XANES main and pre-edge were recorded to determine directly the Fe oxidation state, while Fe-K EXAFS was measured to determine the short-range structure around Fe. For this, the clay suspension after reduction was centrifuged, the wet clay pastes were placed into a HDPE double-confined sample holder in the glovebox ( $\text{O}_2 < 0.1$  ppm), and the holder was then heat-sealed. Once removed from the glovebox, the holders were immediately dropped into LN<sub>2</sub> for flash freezing. The samples were stored and transported in a LN<sub>2</sub>-filled Dewar and transferred in frozen state within less than 5 min into the He-cryostat at the beamline for measurements.

The measurements were carried out at the Rossendorf Beamline (ROBL) BM20 of the European Synchrotron Radiation Facility (ESRF), France.<sup>56</sup> The storage ring was operated at 6 GeV in top-up mode with a ring current of 200 mA. The X-ray beam was monochromatized by a Si(111) double-crystal monochromator. Higher harmonics were suppressed by using two, 1.4 and 1.2 m long silicon mirrors with a grazing incidence angle



of 2.5 mrad. Up to 8 samples were loaded at the same time in the closed-cycle He-cryostat (CryoVac) running at 10-15 K. The energy of the monochromator was calibrated with an Fe foil (7112 eV). The Fe K-edge XAS spectra were collected in fluorescence mode with an 18-discrete-elements Ge-detector (Mirion) equipped with a Falcon-X (XIA) electronic spectrometer using energy steps of 0.5 eV across the XANES region. The recorded raw data were first averaged in Sixpack<sup>57</sup> and then processed in WinXAS<sup>58</sup> using standard procedures for normalization, conversion into k-space by using the first inflexion point of the main edge, and spline background removal with the auto-spline functionality of WinXAS. EXAFS spectra were extracted with k-weight = 3 and k-range = 2-12 Å. The EXAFS shell fitting was carried out in WinXAS in Fourier-transformed R space (k-range = 2-12 Å<sup>-1</sup>; Bessel window; R-range = 1 – 5.5 Å). Theoretical EXAFS paths for shell fitting were calculated self-consistently using FEFF9.6.4,<sup>59</sup> based on the Garfield nontronite structural model.<sup>60</sup>

The pre-edge region of the Fe K-edge was analyzed with Origin software. A cubic spline interpolation was extended several eV before and after the pre-edge to subtract the background from the normalized XANES spectra.<sup>61</sup> The such-derived, normalized pre-edge spectra were deconvoluted with two Voigt functions without any constraints. The centroid position is calculated according to equation 2.3.<sup>62</sup>

$$\text{Centroid} = \text{peak 1} \cdot \frac{\text{area 1}}{\text{total area}} + \text{peak 2} \cdot \frac{\text{area 2}}{\text{total area}} \quad (2.3)$$

Principal component analysis (PCA) of XANES spectra was conducted with the Iterative Target transformation Factor Analysis (ITFA) software package.<sup>63</sup> Linear combination fits (LCF) were performed with Athena.<sup>64</sup>

### 2.2.7 Mediated electrochemical oxidation and reduction

Electron donating and accepting capacities (EDC and EAC) were measured to determine the redox-active Fe in the N<sub>Au</sub>-2 samples. For this, an electrochemical set-up was used as described in Gorski et al.<sup>65</sup> The whole experiment was performed in the glovebox. The electrolyte in all experiments consisted of 0.1 M NaCl, buffered to pH 7 by 0.01 M MOPS (3-(*N*-morpholino)propanesulfonic acid). To facilitate the transfer of electrons between the clay particles and the working electrode, dissolved one-electron transfer mediators were added to the electrochemical cell. The maximum EDC was measured at an applied potential of 0.6 V vs SHE using ABTS (2,2'-azino-bis(3-ethylbenzothiazoline-6-sulphonic acid) as mediator, and the maximum EAC was measured at an applied potential of -0.6 V vs SHE with TQ (1,1'-trimethylene-2,2'-bipyridyl) as mediator. After equilibration of the mediator with the electrochemical cell at a specific applied potential, a small quantity

of NAu-2 suspension (0.02 mL of ~14 g/L) was added and the current monitored. The oxidative and reductive current peaks, caused by oxidation or reduction of redox-active Fe in the clay mineral, were integrated resulting in the EDC or EAC in moles of electrons per gram of sample. Since only the redox active Fe is assessed by MEO/MER, the total Fe was determined by Total Reflection X-Ray Fluorescence (TXRF) (S2 PICOFOX, Bruker). A drop of the clay suspension together with an added internal standard (Se and Ge) was evaporated on a glass carrier disk which was then inserted in and measured by the TXRF.

## 2.3 Results and discussion

### 2.3.1 Reduction

Clay dissolution is widely observed during the CBD reduction process.<sup>44, 51, 66</sup> We performed here a series of reduction experiments without washing process in order to investigate the relationship between the degree of reduction and eventual dissolution of the clay by the reduction procedure. A blank experiment without adding dithionite is considered to represent the dissolution equilibrium of nontronite in 0.1 M NaCl matrix, with 0.8  $\mu\text{mol/g}$  Al, 6.4  $\mu\text{mol/g}$  Fe, and 16.1  $\mu\text{mol/g}$  Si in the supernatant. The amount of Fe, Si, and Al released as a function of dithionite is illustrated in Figure 2.1. The dissolution of all three elements generally increases with dithionite indicating that the CBD treatment causes additional clay dissolution as already reported in previous studies.<sup>51, 66</sup> The released concentration of Si, Al, and Fe are in the same order of magnitude as the ones reported by Jaisi et al.<sup>66</sup> At the highest amount of dithionite added, 42 g/L, the released concentration of Si, Fe, and Al are 322.1  $\mu\text{mol/g}$ , 228.6  $\mu\text{mol/g}$ , and 17.0  $\mu\text{mol/g}$ , respectively, corresponding to 3.7%, 5.8%, and 2.5% dissolution with respect to their contents in NAu-2. Above 20 g/L dithionite, the release of Fe is increasing faster than that of Si and Al (Figure 2.1b), indicating a slight preferential dissolution of Fe up to 5.8% possibly due to a structural reorganization. This suggests that the reduced clay layer structure may not be representative anymore of the initial nontronite layer structure after harsher CBD treatments. This is in line with the work by Hadi et al.,<sup>67</sup> where the negative layer charge of nontronite increased with the degree of reduction (Fe(III) to Fe(II)) at a lower reduction level, but then dropped rapidly at a higher reduction level due to structural reorganization. Jaisi et al. observed similar findings, whereby the stability of the NAu-2 structure remained intact when the reduction degree was below 30%, however, the stability decreased without affecting the structural integrity as the reduction degree increased to 49% indicated by a consistent 001 peak

position in XRD patterns, and ultimately, the N Au-2 structure transitioned into an amorphous state after reaching a Fe(III) reduction degree of 71%.<sup>66</sup> Although no direct structural information can be derived from dissolution experiments, our results suggest that the structure of our two samples used for more detailed analyses, i.e. low-red N Au-2 (0.7% Fe dissolution, 19% Fe(III) reduction degree, Table 2.1) and high-red N Au-2 (2.8% Fe dissolution, 44% Fe(III) reduction degree, Table 2.1), remains identical to that of the initial nontronite N Au-2.<sup>48</sup>

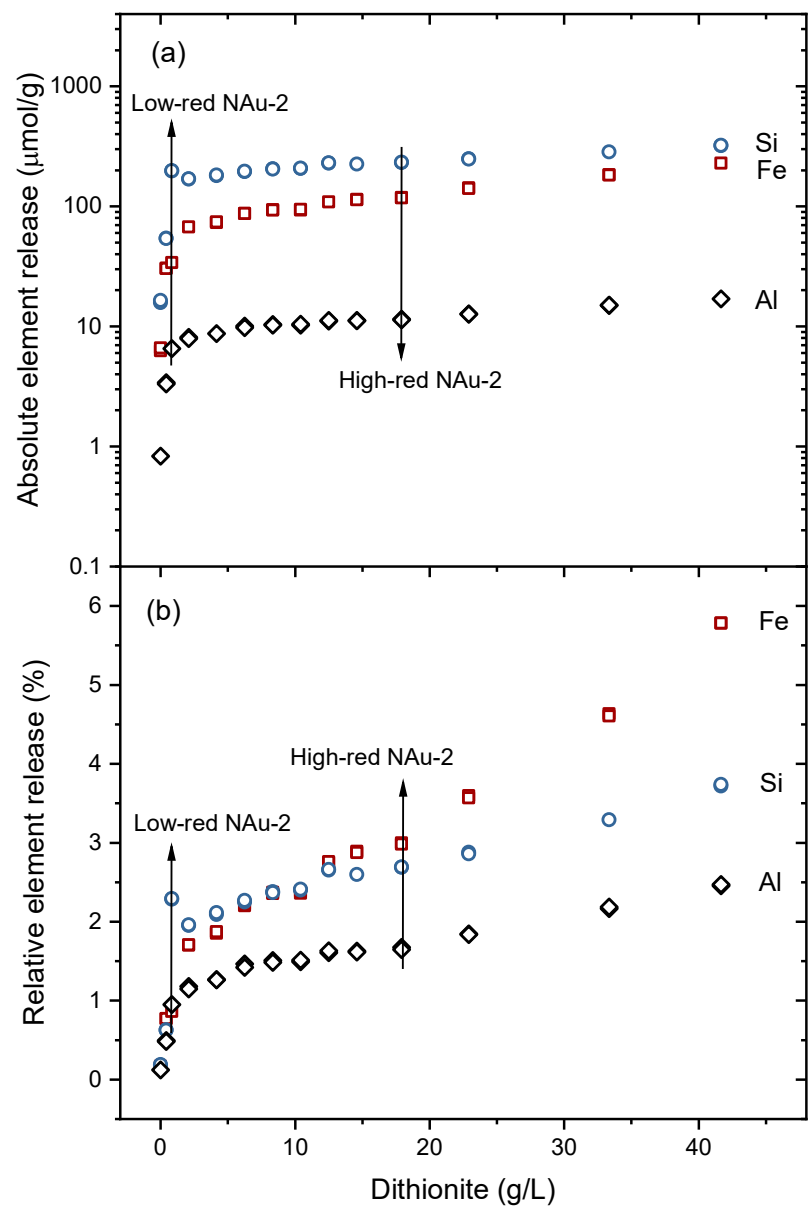


Figure 2.1. Si (blue circle), Fe (red square), and Al (black diamond) released from nontronite by CBD reduction as a function of increasing amounts of dithionite (Errors are smaller than symbol size). Arrows mark the values for the two bulk samples low-red N Au-2 and high-red N Au-2 used for detailed analyses. (a) Absolute element release in  $\mu\text{mol/g}$ ; (b) Relative element release in percent.

2.3.2 X-ray diffraction

Samples of native N<sub>Au</sub>-2, washed low-red and high-red N<sub>Au</sub>-2 were collected for XRD measurements (Figure 2.2). The XRD pattern of sample N<sub>Au</sub>-2 is characteristic for nontronite, with the main reflection being 00 $l$  reflections and asymmetrical  $hk$  reflections due to turbostratic stacking, for example the (11, 02) and (20, 13) reflections at  $\sim 1.41 \text{ \AA}^{-1}$  and  $\sim 2.47 \text{ \AA}^{-1}$ . With increasing reduction degree, additional reflections (black arrows) emerge for example at  $2.23 \text{ \AA}^{-1}$ ,  $3.15 \text{ \AA}^{-1}$ , and  $3.86 \text{ \AA}^{-1}$ , and are attributed to a phase structurally similar to KFeO<sub>2</sub> (ICDD Card #83-2153). The KFeO<sub>2</sub>-like phase was not observed in the as-prepared reduced N<sub>Au</sub>-2 suspension, strongly suggesting that it precipitates during the drying procedure, in spite of using a drying procedure optimized to avoid the possible precipitation of secondary phases. Besides this, the two reduced samples show the typical nontronite pattern, demonstrating the structural integrity after the two CBD treatments.

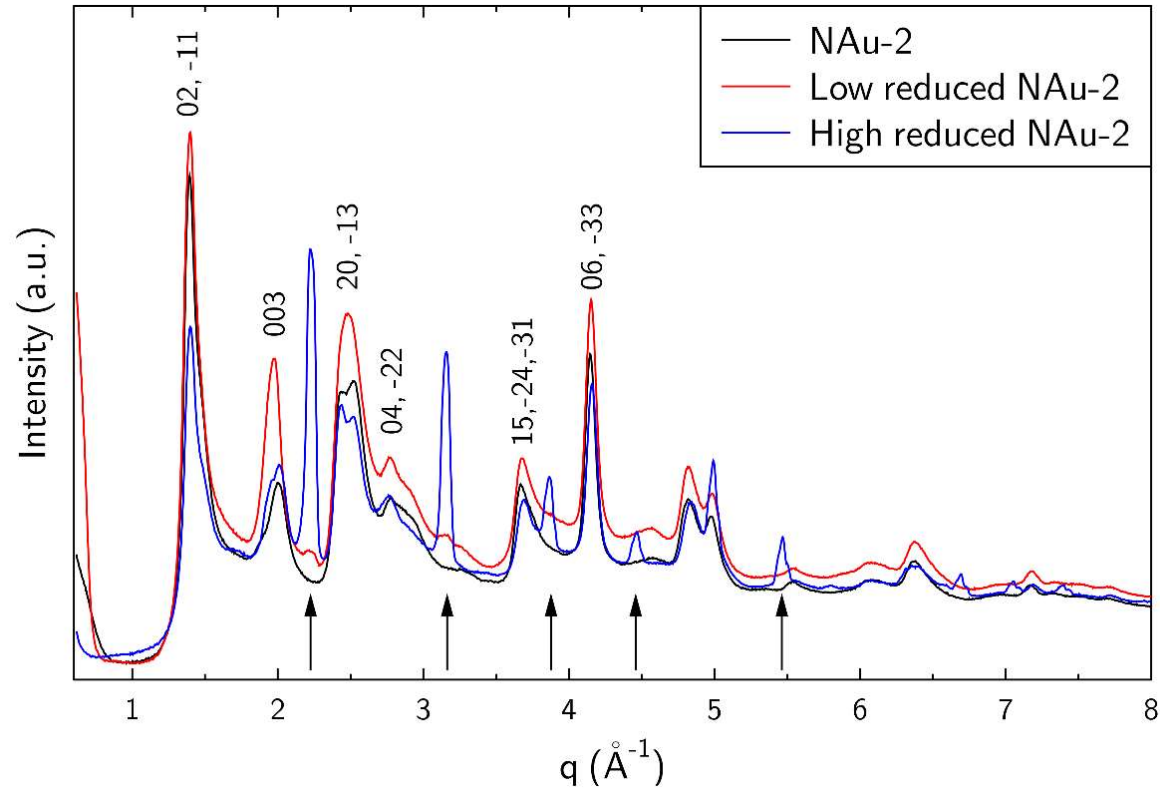


Figure 2.2. XRD patterns of native N<sub>Au</sub>-2, low-red N<sub>Au</sub>-2, and high-red N<sub>Au</sub>-2. Additional lines corresponding to KFeO<sub>2</sub> are marked with arrows.

2.3.3 Transmission electron microscopy

TEM allows studying the morphology and structure of clay minerals, including layer stacking, atomic arrangements, and surface site defects. With the specific sample

preparation method employed here, the clay platelets were preferentially lying perpendicular to the electron beam (i.e. most particles had the **ab** plane perpendicular to the beam), which eased the imaging of the layer plane structure. Furthermore, this unified orientation allowed us to minimize exposure time, while longer exposition times would have been required if the sample had to be tilted to obtain an adequate observation angle. Finally, this preparation procedure allowed us to obtain numerous particles having the same orientation and about the same depth within the resin. Therefore, the acquisition parameters could be optimized first with a trial particle, before moving to a particle used for analysis. The layer structure of nontronite was observed in all three clay samples (Figure 2.3), and no other solids were detected (note that the two reduced samples were prepared with an additional acid wash after reduction to remove any impurities that have the potential to re-absorb to the clay mineral or remain as precipitates in the clay suspension). As highlighted by the yellow lines, the layer-to-layer distance is 10 – 12 Å, which agrees well with the theoretical layer-to-layer distance in smectite, derived by XRD of oriented clay films.<sup>68</sup> Again, the reduced NAu-2 has the same layer structure and a similar layer-to-layer distance as the native sample, showing that the clay structure is stable and well preserved after the CBD treatment. Nevertheless, a slight dissolution of the basal planes is noticeable on the external surfaces, but not in the bulk structure (see areas defined with red dotted lines in Figure 2.3b and Figure 2.3c). The structure images obtained by TEM, therefore, corroborate the results of the reduction experiment (Figure 2.1) and XRD (Figure 2.2) in that the observed 2.8% dissolution affects only the external basal plane surfaces and not affect the bulk structure of nontronite.

In addition, another distance of 4.5 Å was observed in all three nontronite samples. In the TOT layer, a lattice fringe with a distance of 4.5 Å is clearly visible along each layer. The same value could also be obtained by applying the Fast Fourier Transform (FFT) method to the structure area of the selected layer in Figure 2.3c, to transfer the image in the selected region to the frequency domain. The reciprocal value of the frequency 2.19 1/nm is about 4.5 Å, and this distance exists throughout the whole image. This distance corresponds to trans-vacant octahedra in the [100] and [001] axis, where the lattice fringes of 4.5 Å and 10 Å are perpendicular (Figure 2.3a, 2.3c, 2.3e, 2.3i), or in the [110] axis with inclined lattice fringes (Figure 2.3b, 2.3g), where Fe and Si are located in the solid line region and only O occupies the area delineated by dashed lines. In contrast to the trans-vacant case, Fe and Si would be evenly distributed throughout the cis-vacant octahedra (Figure 2.3d, 2.3f, 2.3h);

the resulting cation separation distance of  $\sim 1.5$  Å would be too small to be resolved at the available TEM settings. Only with a TEM resolution better than 1.5 Å, both cis-vacant and trans-vacant octahedra would be discernible.

In previous work, it was proposed that iron moves from cis to trans sites during reduction and forms trioctahedral domains and large vacancies in the octahedral sheets.<sup>41, 45, 69, 70</sup> We could not confirm this for the low-red NAu-2 and high-red NAu-2 samples. Either these phenomena are irregular on a small scale and hence difficult to capture by TEM, or our relatively mild CBD treatment did not cause such a reorganization of the octahedral sheets. Note that the degree of reduction of nontronite was more than 99% in the work of Manceau et al.,<sup>45</sup> while it is less than 44% in our study. According to Figure 2.1, a reduction degree of more than 44 % ( $> 20$  g/L dithionite) can cause preferential dissolution of Fe in the octahedral sheet, which may result in further iron migration and structural reorganization.<sup>67</sup> Therefore, the relationship between structural reorganization and reduction degree beyond  $\sim 40\%$  reduction should be studied in more detail in future work.

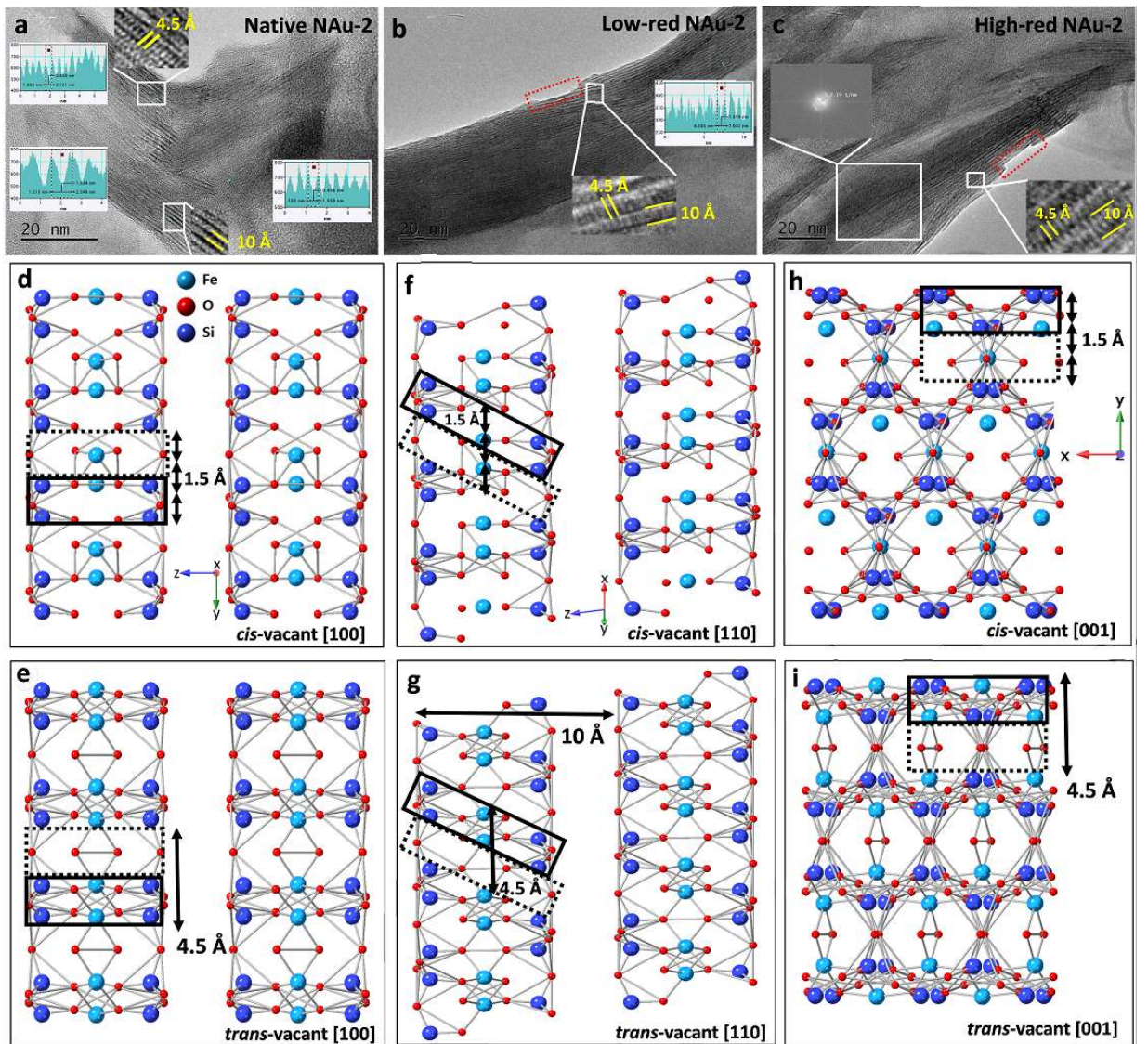


Figure 2.3 TEM image of (a) native NAu-2, (b) low-red NAu-2, (c) high-red NAu-2. Nontronite structure of (d) cis-vacant octahedra [100], (e) trans-vacant octahedra [100], (f) cis-vacant octahedra [110], (g) trans-vacant octahedra [110], (h) cis-vacant octahedra [001], (g) trans-vacant octahedra [001].

#### 2.3.4 Mössbauer spectrometry

The measurements were first carried out with a large velocity scale to check for the presence of additional lines, i.e. magnetic sextets attributed to certain magnetic Fe oxides. Then, the measurements were repeated with a more appropriate velocity scale to optimize the resolution of the hyperfine structures in the region of interest. Only the Mössbauer spectra registered at 77 K (low velocity scale) are presented in Figure 2.4, and their refined values of the hyperfine parameters are listed in Table 2.1. The spectrum of the native NAu-2 required decomposition by at least two quadrupolar components, but a third component



can be considered, further improving the fit. Another fitting model can be obtained by considering the presence of a certain degree of preferential orientation, in agreement with the previous results of X-ray diffraction in this study, with asymmetric quadrupolar components. These different models are characterized by two different values of the isomer shift which are attributed to High Spin (HS) Fe(III) species located in cis- and trans-octahedral sites, as previously observed in the literature.<sup>71</sup> It is also important to note that the presence of HS Fe(III) species in the tetrahedral site, if any, would not exceed 2% (limit of detection). The spectra obtained on low-red and high-red N Au-2 differ from the unreduced, native N Au-2 with the appearance of an additional broad line, whose intensity increases with the degree of reduction. Different fitting models were considered involving between two and six different quadrupolar components, associated or not with some preferential orientation, as previously mentioned in the XRD analysis. They lead to two subspectra, as shown in Figure 2.4, and the corresponding refined mean values of the hyperfine parameters are given in Table 2.1. They are unambiguously attributed to the presence of HS Fe(III) and HS Fe(II) species, the second component increasing with the degree of reduction. It is also important to note that the different fitting models do not allow us to confirm the presence of cis and trans HS Fe(III) located in octahedral units. According to these fits, the fraction of Fe(II) is 0 in native N Au-2, 0.19 in low-red N Au-2, and 0.44 in high-red N Au-2 (see a comparison of Fe(II) fractions obtained by all methods below).

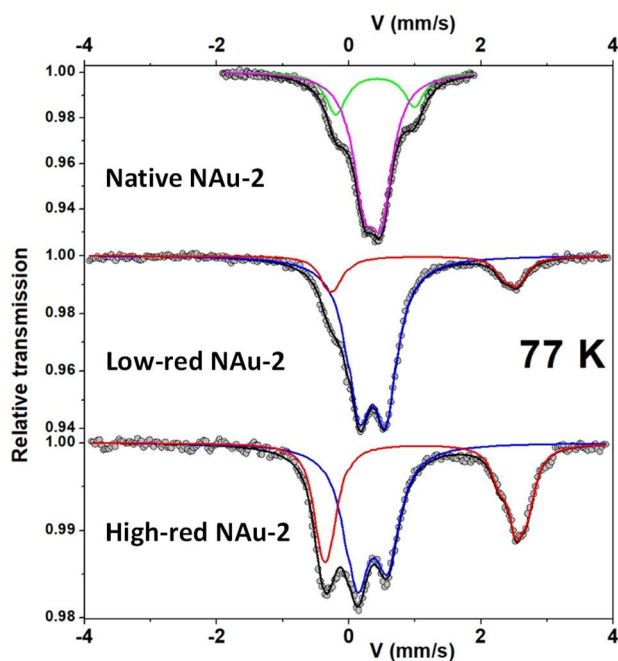


Figure 2.4. Mössbauer spectra of native N Au-2, low-red N Au-2, and high-red N Au-2 at 77 K (see Table 2.1 for the colors).



Table 2.1. Refined hyperfine parameters for the different components of the 77K Mössbauer spectra (see Figure 2.4 for the color of spectral components).

	$\delta$ (mm/s) $\pm 0.01$	QS (mm/s) $\pm 0.02$	% (%) $\pm 2$	Fe site	Color (see Figure 2.4)
Native N Au-2	0.52	1.17	24	Fe(III)	Green
	0.47	0.27	76	Fe(III)	Magenta
Low-red N Au-2	0.47	0.41	81	Fe(III)	Blue
N Au-2	<1.23>	<2.73>	19	Fe(II)	Red
High-red	0.47	0.45	56	Fe(III)	Blue
N Au-2	<1.22>	<2.86>	44	Fe(II)	Red

### 2.3.5 X-ray photoelectron spectroscopy

XPS spectra were used to further probe the Fe redox state of nontronite samples. As shown in Figure 2.5, Fe(II) fractions in native N Au-2, low-red N Au-2, and high-red N Au-2 are 0.07, 0.24, 0.46, respectively, hence 5 to 10% higher than the values derived by Mössbauer spectrometry (Table 2.1). Such slightly higher Fe(II) fractions in nontronite derived by XPS have been explained by Yuan et al. with an accumulation of Fe(II) at the surface through electron transfer,<sup>69</sup> which is selectively probed by the surface-sensitive XPS method.<sup>72</sup> Since a reduction of U(VI) to U(IV) by X-ray irradiation in XPS measurement was observed,<sup>73</sup> 7% of Fe(II) in native N Au-2 could also result from X-ray irradiation of Fe(III). The effect of X-ray irradiation is hard to avoid, therefore, caution has to be taken in interpreting XPS data quantitatively.

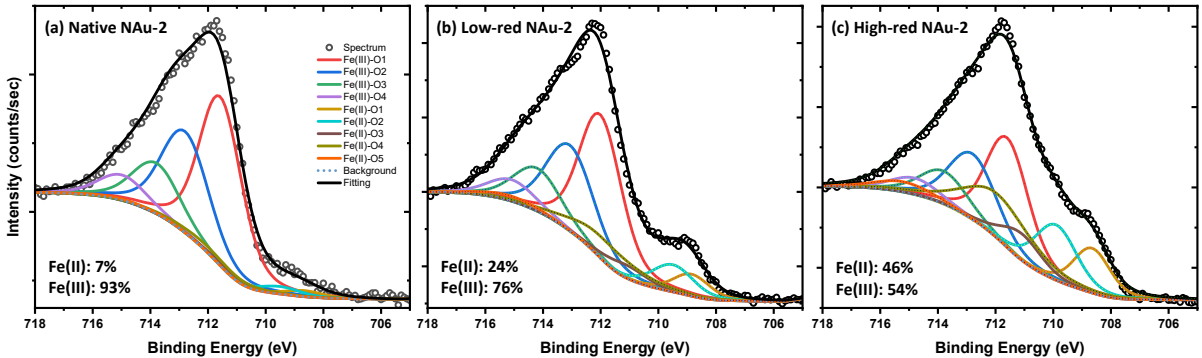


Figure 2.5. XPS spectra of (a) Native N Au-2; (b) Low-red N Au-2; (c) High-red N Au-2. The binding energy, full width at half-maximum (FWHM), area, and percentage of each Fe species are shown in Table S2.1.

### 2.3.6 Fe K-edge XAFS

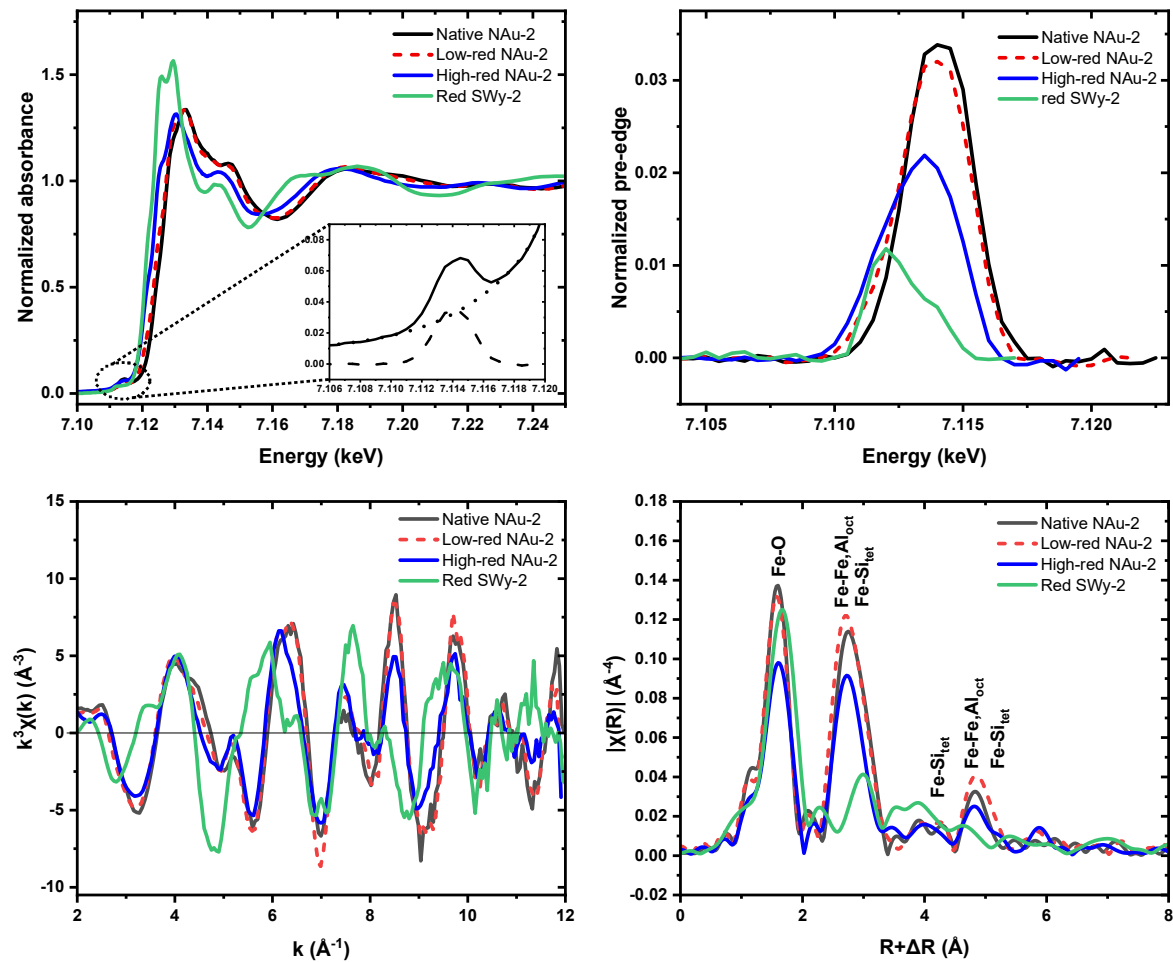


Figure 2.6. Fe K-edge XAFS spectra of native NAu-2, low-red NAu-2, high-red NAu-2, and red SWy-2. The spectrum of red SWy-2 is from Soltermann et al.,<sup>74</sup> where the complete reduction of Fe was confirmed by Mössbauer spectrometry. (a) normalized absorbance (XANES); the insert shows the pre-edge peak (solid line) of native NAu-2 with background (dot line) and the separated pre-edge peak (dash line). (b) normalized Fe K pre-edge peaks. (c)  $k^3$ -weighted EXAFS chi function. (d)  $k^3$ -weighted EXAFS Fourier transform magnitude.

Figure 2.6a shows the Fe K-edge XANES spectra. Assuming that Fe resides prevailing in octahedral sites, the main absorption edge is shifted towards higher energy with increasing oxidation state because of the increasing shielding of the core electron. Accordingly, the edge of the clay samples increases as expected from the (fully reduced) SWy-2 to high-red NAu-2, low-red NAu-2, to the (fully oxidized) native NAu-2. To quantify the Fe(II) fraction, we first applied classical linear combination fit of the XANES spectra. As first endmember we employed native NAu-2, where Mössbauer spectrometry and the Fe-O distance from EXAFS shell fitting (see below) confirmed 100% structural

Fe(III). As second endmember we tested first the XANES spectrum of an Fe(II) aquo complex, which provided only a poor reconstruction of the spectrum of high-red NAu-2, in spite of an assumed octahedral coordination to water molecules. A much better reconstruction was obtained by using the spectrum of red-SWy-2 from Soltermann et al. as endmember,<sup>74</sup> where the much lower content of structural Fe (2.9 wt%) permitted a complete Fe reduction as confirmed by Mössbauer spectrometry (Table S2.2 & Figure S2.2). The such obtained Fe(II) fraction of 0.14 for low-red NAu-2 and 0.48 for high-redNAu-2 are very similar to the Mössbauer values of 0.19 and 0.44 considering the intrinsic error of both methods (Table 2.1). For comparison, we analyzed the set of spectra also with the Iterative Transformation Factor Analysis (ITFA) package, which offers a more thorough statistical approach with respect to the number of spectral components present, as well as an improved noise filtering in comparison to linear combination fitting.<sup>63</sup> Principal component analysis and the Malinoswki indicator confirmed that indeed only two components are present in the data set. Second, VARIMAX rotation and iterative target test transformation was applied to derive the fraction of Fe(II) in the samples. In spite of the presumably more robust procedure and the improved noise filtering of this method<sup>75</sup> the results were identical to conventional LCF (Table S2.2).

Since the XANES edge is not only influenced by the oxidation state, but due to multiple scattering phenomena also by the local coordination geometry, we analyzed also the pre-edge which gives directly the energy of the 1s to 3d electronic transitions and is hence a more direct approach for determining the oxidation state of Fe.<sup>76</sup> For this, we extracted the pre-edge peak from the normalized XANES by subtracting a spline background (Figure 2.6a demonstrates the procedure and Figure 2.6b shows the extracted pre-edge peaks). As expected, the peaks shift to higher energy with decreasing Fe(II) fraction. A more refined analysis was conducted following the approach of Wilke et al. by fitting two Voigt functions to the pre-edge peaks (Figure S2.3) and calculating the centroid position (Table S2.3).<sup>62</sup> When plotting the centroid position versus the Mössbauer-derived Fe(III) fraction, we obtained a linear relationship (Figure S2.4) following the regression equation  $y = 586.7x - 4173$ . Note that the normalized pre-edge height of tetrahedral Fe is  $>0.2$ ,<sup>62</sup> hence one order of magnitude higher than that of the NAu-2 samples, confirming that both Fe(II) and Fe(III) reside prevalently ( $>90\%$ ) in octahedral sites. We conclude that both the main XANES edge as well as its pre-edge provide reliable measurements for the Fe(II)/Fe(III) ratio in the nontronite samples, since the local Fe coordination remains octahedral.

Using Fe K-edge EXAFS spectroscopy, which provides the short range order around the X-ray absorbing Fe atoms, we studied the structural changes induced in nontronite by the different redox steps. The  $k^3$ -weighted EXAFS spectra (Figure 2.6c) as well as their Fourier Transform Magnitudes (FTM) (Figure 2.6d), which can be considered as statistical (pseudo-) radial distribution functions around the X-ray absorbing Fe atoms, show changes of the oxygen coordination sphere (1<sup>st</sup> FTM peak at about 1.7 Å), the nearest cation neighbors such as octahedral Fe or Al and tetrahedral Si (2<sup>nd</sup> FTM peaks at about 2.8 Å), and next nearest cation neighbors octahedral Fe or Al and tetrahedral Si (3<sup>rd</sup> FTM peaks at about 4.9 Å, all uncorrected for phase shift). Since Fe(II) and Fe(III) have different ionic radii (0.78 versus 0.65 Å for six-coordinated cations in high-spin configuration<sup>77</sup>), the length of the Fe-O bond commonly decreases from e.g. 2.14 Å in Fe(OH)<sub>2</sub> to about 2.00 Å in common Fe(III) (hydr)oxides. Note that the EXAFS resolution of 0.16 Å as given by the  $\chi$ -range of 2 to 12 Å<sup>-1</sup> did not allow us to fit the shells corresponding to octahedral Fe(II), Fe(III), and potentially mixed Fe(II,III) sites individually. Table 2.2 shows hence only the average distance determined by fitting one Fe-O shell. The fully oxidized standard for structural Fe(III), native NAu-2, has an Fe-O distance of 2.01 Å, close to that of Fe(III) (hydr-)oxides. The fully reduced standard for structural Fe(II), red SWy-2, has an Fe-O distance of 2.10 Å, hence 0.02 to 0.04 Å shorter than common Fe(II)-O coordinated structures, most likely due to constraints of the clay structure. Low-red NAu-2 has a distance of 2.02 Å and high-red NAu-2 2.05 Å (Table 2.2). Assuming a linear relationship between Fe oxidation state and Fe-O bond length within the octahedral clay sites, we obtain based on the two endmembers  $y=10.99x-22.09$  ( $y$ : fraction of Fe(II),  $x$ : Fe-O bond length), and hence 11% Fe(II) for low reduced NAu-2 and 44% for high reduced NAu-2, in excellent agreement with the XANES result. Therefore, also EXAFS fitting of the Fe-O coordination shell can be used to derive the Fe oxidation state in nontronite and similar dioctahedral clays.

Even more importantly, EXAFS shell fitting allowed us to study the structural changes induced by the reduction within radial distances up to 6 Å from the Fe centers. In native NAu-2, 73% of octahedral positions are occupied by Fe, and the remaining 27% by Al and Mg, as indicated by the structural equation  $(M^{+0.97})[Si_{7.57}Al_{0.01}Fe_{0.42}][Al_{0.52}Fe_{3.32}Mg_{0.7}]O_{20}(OH)_4$ .<sup>48</sup> To reflect this situation during our EXAFS shell fits, we fitted first and second metal shells using both Fe-Fe and Fe-Al paths (note that both Al and Mg produce almost identical backscattering functions and hence cannot be distinguished). To reduce the

large number of fitting parameters, which would necessarily lead to strong collinearity effects, we correlated distances and Debye-Waller factors for both elements and limited the sum of the coordination numbers to their crystallographic values of the dioctahedral structure, i.e. 3 for the first and 6 for the second metal shell (Table 2.2). The such derived first metal shell coordination numbers of 2.1 for Fe and 0.9 for Al/Mg correspond to octahedral occupancies of 70% Fe ( $2.1/3.0 \times 100$ ) and 30% Al/Mg ( $0.9/3.0 \times 100$ ), thereby nicely confirming the independently derived structural equation of nontronite in spite of the rather high error for EXAFS-derived coordination numbers.

For the two reduced samples, the coordination numbers of the two Fe-Fe shells increase, while those of the Fe-Al shells decrease. For the first metal shell, we thereby obtain a Fe occupancy of 83% ( $2.5/3 \times 100$ ), and correspondingly of 17% for Al/Mg (Table 2.2). These changes suggest the formation of Fe clusters by the clay reduction, in line with previous results by Manceau et al., who proposed a migration of Fe cations to neighboring sites after the reduction of Fe(III) to Fe(II).<sup>45</sup> These authors also suggested that this clustering of Fe(II) sites is accompanied by formation of a local tri-octahedral structure. Due to model overparametrization problems (see above), we were not able to adjust our EXAFS fitting scheme to allow for such a transition, which would require an fitted increase of the summed coordination number of the first Fe-Fe,Al shell to a range from 3 to 6. Note that the fitted  $S_0^2$  values of the clay samples are with 0.56 rather small due to fluorescence self-absorption effects because of the rather high Fe concentrations, but they did not influence the coordination numbers, which were fixed according to the crystallographic nontronite model.

The obtained distances of native N<sub>Au</sub>-2 are well in line with the nontronite structure. For high-red N<sub>Au</sub>-2, the nearest Fe-Fe,Al and Fe-Si shells show a slight increase of 0.01 to 0.02 Å, probably an effect of the average increase of Fe-O coordination distances due to an increase of the Fe(II) fraction. Note, however, that this tendency is not confirmed for longer distances. The Debye-Waller factors of all shells reveal an increasing static disorder of the shells with increasing Fe(II)/Fe(III) ratio. This is coherent with an increasing degree of structural constraints in the layers due to isomorphous substitution of Fe(III) by Fe(II).

Table 2.1. Fe K-edge EXAFS shell fitting results

Sample	Shell	CN <sup>a</sup>	R [Å] <sup>b</sup>	σ <sup>2</sup> [Å <sup>2</sup> ] <sup>c</sup>	ΔE <sub>0</sub> [eV]	S <sub>0</sub> <sup>2</sup>	Residual
Native NAu-2	Fe-O	6*	2.01	0.0042	10.1	0.57	9.7
	Fe-Fe	2.1 <sup>d</sup>	3.04 <sup>d</sup>	0.0010 <sup>d</sup>			
	Fe-Al <sup>§</sup>	0.9 <sup>d</sup>	3.04 <sup>d</sup>	0.0010 <sup>d</sup>			
	Fe-Si	4*	3.28	0.0010			
	Fe-Si	4*	4.46	0.0046			
	Fe-Fe	4.5 <sup>e</sup>	5.26 <sup>e</sup>	0.0042 <sup>e</sup>			
	Fe-Al <sup>§</sup>	1.5 <sup>e</sup>	5.26 <sup>e</sup>	0.0042 <sup>e</sup>			
	Fe-Si	8*	5.54	0.0066			
Low-red NAu-2	Fe-O	6*	2.02	0.0039	5.8	0.56	6.2
	Fe-Fe	2.5 <sup>d</sup>	3.04 <sup>d</sup>	0.0012 <sup>d</sup>			
	Fe-Al <sup>§</sup>	0.5 <sup>d</sup>	3.04 <sup>d</sup>	0.0012 <sup>d</sup>			
	Fe-Si	4*	3.28	0.0010			
	Fe-Si	4*	4.48	0.0028			
	Fe-Fe	5.5 <sup>e</sup>	5.25 <sup>e</sup>	0.0042 <sup>e</sup>			
	Fe-Al <sup>§</sup>	0.5 <sup>e</sup>	5.25 <sup>e</sup>	0.0042 <sup>e</sup>			
	Fe-Si	8*	5.52	0.0044			
High-red NAu-2	Fe-O	6*	2.05	0.0066	6.4	0.56	7.8
	Fe-Fe	2.5 <sup>d</sup>	3.05 <sup>d</sup>	0.0039 <sup>d</sup>			
	Fe-Al <sup>§</sup>	0.5 <sup>d</sup>	3.05 <sup>d</sup>	0.0039 <sup>d</sup>			
	Fe-Si	4*	3.30	0.0029			
	Fe-Si	4*	4.46	0.0039			
	Fe-Fe	5.5 <sup>e</sup>	5.23 <sup>e</sup>	0.0081 <sup>e</sup>			
	Fe-Al <sup>§</sup>	0.5 <sup>e</sup>	5.23 <sup>e</sup>	0.0081 <sup>e</sup>			
	Fe-Si	8*	5.49	0.0091			
Red SWy-2	Fe-O	6*	2.10	0.0031	6.64	0.70	4.6

a: Error of coordination number (CN) ± 25%  
b: Error of radial distance (R) ± 0.01 Å  
c: Error of Debye-Waller factor (σ<sup>2</sup>) ± 0.002 Å<sup>2</sup>  
\*: CN fixed according to the structural model of Garfield nontronite <sup>39</sup>.  
d: For the fits of the two nearest Fe<sub>Oct</sub> and Al<sub>Oct</sub> paths, the sum of both CNs was fixed at 3, while both their R and σ<sup>2</sup> values were correlated.  
e: For the fits of the next nearest Fe<sub>Oct</sub> and Al<sub>Oct</sub> paths, the sum of both CNs was fixed at 6, while both their R and σ<sup>2</sup> values were correlated.  
§: Fe-Al represents Fe-(Al+Mg). Al and Mg cannot be differentiated by EXAFS due to their similar electron densities.  
Fitted spectra are shown in Figure S2.5.

2.3.7 Mediated electrochemical oxidation and reduction

In the clay sample, Fe(II) can be transformed to Fe(III) and vice versa by applying oxidizing and reducing potential, respectively. Mediators are used to facilitate the electron transfer in the redox reaction between structural Fe in the clay minerals and working electrode. When an potential is applied, the amount of electrons transferred can be calculated

by integration of the generated current peak so as to get the amount of Fe(II) or Fe(III) in the clay mineral. Table 2.3 shows that the Fe(II)% of native, low-red, and high-red N Au-2 are 0.1%, 19%, and 58%. Moreover, the sum of EDC and EAC indicates the amount of redox-active Fe in the clay structure. In both native and reduced N Au-2 samples, around 30% of total structural Fe is not redox-active when measured by MEO/MER. The fact that 20% of total structural Fe in nontronite is not redox-active has also been reported before by Gorski et al.<sup>65</sup>

Table 2.2. EDC and EAC of nontronite clay samples measured by MEO/MER

Sample	Total Fe <sup>§</sup> (mmol/g <sub>clay</sub> )	EDC* (mmol <sub>e</sub> -/g <sub>clay</sub> )	EAC* (mmol <sub>e</sub> -/g <sub>clay</sub> )	EDC (%Fe <sub>tot</sub> )	EAC (%Fe <sub>tot</sub> )
Native N Au-2	3.9	0.00	2.94	0.1	75
Low-red N Au-2	3.8	0.74	1.72	19	45
High-red N Au-2	3.8	2.19	0.45	58	12

\*: Electron donating capacity (EDC, mmol<sub>e</sub>-/g<sub>clay</sub>) and electron accepting capacity (EAC, mmol<sub>e</sub>-/g<sub>clay</sub>) are the amount of Fe(II) and Fe(III) normalized with the mass of clay mineral, respectively.  
 §: The total Fe amount was corresponding to 31 wt% Fe<sub>2</sub>O<sub>3</sub> in the clay structure.

### 2.3.8 Fe redox state identification

Different methods were applied to measure the Fe redox state in nontronite. XAS demonstrates relatively lower Fe(II) fractions on low-red N Au-2 comparing with the results of MEO/MER and Mössbauer; the Fe(II) fractions of high-red N Au-2 is between the results of Mössbauer and MEO/MER; meanwhile, XPS shows slightly higher Fe(II) fractions on both reduced samples comparing with Mössbauer result (Table 2.4). First of all, the sample preparation of each method has been conducted with uttermost care to keep the original oxidation state. Schaefer et al. suggested that Mössbauer spectra measured at RT and even at 77 K may significantly underestimate Fe(II);<sup>78</sup> we cannot confirm this, since our data collected at 77 K agree well with that of the other techniques. X-ray irradiation induced Fe reduction in XPS was evident since 0.07 of Fe(II) fraction was detected in native N Au-2 which in fact should be fully oxidized. Sorption of cation mediators on montmorillonite has been reported owing to the high surface charge density of clay minerals and the increase of the current peak in MEO/MER measurement was substantial,<sup>79</sup> nevertheless, ABTS is a anion mediator, of which sorption is not an issue in the measurement. Little has been known so far concerning the stability of mediators and the high Fe(II) fraction 0.58 in high-red N Au-2 in MEO/MER measurement. Both XANES and EXAFS as independent

measurements of prevalently electronic and short-range structure, respectively, show good consistency of Fe(II) fractions. The results confirm the reliability of the different analyses of XANES and EXAFS, however, they are also highly dependent on the calibration curve given by standards.<sup>62,80</sup> Initially, Fe<sup>2+</sup><sub>aq</sub> was utilized as a reference for Fe(II) standard; however, it exhibited an approximately 8% difference in Fe(II) fraction owing to dissimilar structures compared to smectite clays. Hence, careful consideration is necessary when selecting standards to establish a precise calibration curve before determining Fe(II) fractions. Overall, the Mössbauer measurement maintains its rank as currently most reliable stand-alone method to determine Fe(II) fraction in clay minerals.

Table 2.3. Comparison of Fe(II) fractions in the three N Au-2 samples obtained by different measurements. Note that for the XANES centroid and EXAFS Fe-O methods, native N Au-2 was used as the standard for pure Fe(III), hence Fe(II) fractions of this sample are necessarily 0, while Mössbauer, XPS, and MEO/MER provide the Fe(II) fraction of native N Au-2 independently.

	Mössbauer at 77K	XPS	XAS				MEO/MER
			XANES centroid	XANES ITFA	XANES LCF	EXAFS Fe-O	
Native N Au-2	0.00	0.07	0.00	0.00	0.00	0.00	0.00
Low-red N Au-2	0.19	0.24	0.16	0.15	0.14	0.11	0.19
High-red N Au-2	0.44	0.46	0.50	0.51	0.48	0.44	0.58

## 2.4 Conclusions

In this study, we demonstrate the structure of our native and reduced nontronite samples, and the structural integrity is ensured after CBD reduction. Quantitative Fe redox state measurements including Mössbauer spectrometry, XPS, XANES, EXAFS, and MEO/MER are compared to exhibit the difference between each method. All methods provide errors of only a few percent relative to a mean value, and this is most likely because of the large precautions to conserve the Fe oxidation state from clay reduction to final analysis. The consistent results indicate that these methods have great potential to be applied to other clay samples.

Fe-bearing clay minerals are one of the main components in soil. Variation of redox potential induced by Fe-bearing clay minerals under alternate flooding-drining condition is expected in different soils and can cause significant changes in soil functioning, plant



response, soil bacterial community, N and P removal efficiency, organic matter decomposition, nutrient cycling, etc.<sup>81-84</sup> Therefore, comprehensive characterization methods of structural Fe redox state associated with redox potential are of particular importance in monitoring and predicting the biogeochemical processes in natural environment. Moreover, Fe-bearing clay mineral also has a strong influence on the fate of contaminants in the environment. Especially in deep geological repositories, Fe-bearing clay minerals play an important role in controlling and immobilizing the radionuclides in radioactive waste by reducing them to a lower and less soluble valence state. A thorough comprehension of these redox processes can significantly contribute to the safety assessment.<sup>79, 85</sup> Such a complete picture of nontronite structure, reduction, and Fe redox state identification builds up a strong basis for studies on resemble Fe-bearing clay minerals and provides references on methods of Fe redox state measurement.

## **Acknowledgments**

This work was supported by European Union's Horizon 2020 research and innovation program under grant agreement No 847593. We thank Astrid Schaible and Andreas Laube for laboratory technical support. The work of XPS has received support under the CERTeM 2020 Program, with the financial support of the Regional Council Centre-Val de Loire (CERTeM 2020 201400096812) and co-funded by the European Union through the European Regional Development Fund (ERDF 2017-EX002247). Beamtime at The Rossendorf Beamline at ESRF was provided by ESRF and HZDR.

## 2.5 Reference

- (1) Huang, J.; Jones, A.; Waite, T. D.; Chen, Y.; Huang, X.; Rosso, K. M.; Kappler, A.; Mansor, M.; Tratnyek, P. G.; Zhang, H. Fe(II) Redox Chemistry in the Environment. *Chemical Reviews* **2021**, *121* (13), 8161-8233.
- (2) Gorski, C. A.; Klupfel, L. E.; Voegelin, A.; Sander, M.; Hofstetter, T. B. Redox properties of structural Fe in clay minerals: 3. Relationships between smectite redox and structural properties. *Environ Sci Technol* **2013**, *47* (23), 13477-13485.
- (3) Borch, T.; Kretzschmar, R.; Kappler, A.; Cappellen, P. V.; Ginder-Vogel, M.; Voegelin, A.; Campbell, K. Biogeochemical Redox Processes and their Impact on Contaminant Dynamics. *Environmental Science & Technology* **2010**, *44* (1), 15-23.
- (4) Stucki, J. W.; Bailey, G. W.; Gan, H. Oxidation-reduction mechanisms in iron-bearing phyllosilicates. *Applied Clay Science* **1996**, *10* (6), 417-430.
- (5) Coward, E. K.; Ohno, T.; Plante, A. F. Adsorption and molecular fractionation of dissolved organic matter on iron-bearing mineral matrices of varying crystallinity. *Environmental science & technology* **2018**, *52* (3), 1036-1044.
- (6) Aepli, M.; Thompson, A.; Dewey, C.; Fendorf, S. Redox Properties of Solid Phase Electron Acceptors Affect Anaerobic Microbial Respiration under Oxygen-Limited Conditions in Floodplain Soils. *Environmental Science & Technology* **2022**.
- (7) Marican, A.; Durán-Lara, E. F. A review on pesticide removal through different processes. *Environmental Science and Pollution Research* **2018**, *25* (3), 2051-2064.
- (8) Cosgrove, S.; Jefferson, B.; Jarvis, P. Pesticide removal from drinking water sources by adsorption: a review. *Environmental Technology Reviews* **2019**, *8* (1), 1-24.
- (9) Yin, H.; Yang, P.; Kong, M.; Li, W. Use of lanthanum/aluminum co-modified granulated attapulgite clay as a novel phosphorus (P) sorbent to immobilize P and stabilize surface sediment in shallow eutrophic lakes. *Chemical Engineering Journal* **2020**, *385*, 123395.
- (10) Buzetky, D.; Nagy, N. M.; Kónya, J. Use of La-, Ce-, Y-, Fe-bentonites for removing phosphate ions from aqueous media. *Periodica Polytechnica Chemical Engineering* **2017**, *61* (1), 27-32.
- (11) Ravindiran, G.; Ganapathy, G. P.; Josephraj, J.; Alagumalai, A. A critical insight into

- biomass derived biosorbent for bioremediation of dyes. *ChemistrySelect* **2019**, 4 (33), 9762-9775.
- (12) Zhang, L.; Xiang, P.; Bao, X.; Xiong, M.; Liu, F. The Influence of Humic Substances on the Sorption of Three Organic Contaminants with Different Structure and Polarity to Clay Minerals. *Water, Air, & Soil Pollution* **2017**, 228 (6), 199.
  - (13) O'Connor, D.; Hou, D.; Ok, Y. S.; Song, Y.; Sarmah, A. K.; Li, X.; Tack, F. M. G. Sustainable in situ remediation of recalcitrant organic pollutants in groundwater with controlled release materials: A review. *Journal of Controlled Release* **2018**, 283, 200-213.
  - (14) Ugwu, I. M.; Igbokwe, O. A. Sorption of heavy metals on clay minerals and oxides: a review. *Advanced sorption process applications* **2019**, 1-23.
  - (15) Jiménez-Castañeda, M. E.; Medina, D. I. Use of surfactant-modified zeolites and clays for the removal of heavy metals from water. *Water* **2017**, 9 (4), 235.
  - (16) Saeedi, M.; Li, L. Y.; Grace, J. R. Desorption and mobility mechanisms of co-existing polycyclic aromatic hydrocarbons and heavy metals in clays and clay minerals. *Journal of environmental management* **2018**, 214, 204-214.
  - (17) Debure, M.; Tournassat, C.; Lerouge, C.; Madé, B.; Robinet, J.-C.; Fernández, A. M.; Grangeon, S. Retention of arsenic, chromium and boron on an outcropping clay-rich rock formation (the Tégulines Clay, eastern France). *Science of the total environment* **2018**, 642, 216-229.
  - (18) Marques Fernandes, M.; Baeyens, B.; Dähn, R.; Scheinost, A. C.; Bradbury, M. H. U(VI) sorption on montmorillonite in the absence and presence of carbonate: A macroscopic and microscopic study. *Geochimica et Cosmochimica Acta* **2012**, 93, 262-277.
  - (19) Bachmaf, S.; Merkel, B. J. Sorption of uranium (VI) at the clay mineral–water interface. *Environmental Earth Sciences* **2011**, 63 (5), 925-934.
  - (20) Bradbury, M. H.; Baeyens, B. Predictive sorption modelling of Ni(II), Co(II), Eu(III), Th(IV) and U(VI) on MX-80 bentonite and Opalinus Clay: A “bottom-up” approach. *Applied Clay Science* **2011**, 52 (1), 27-33.
  - (21) Marques Fernandes, M.; Vér, N.; Baeyens, B. Predicting the uptake of Cs, Co, Ni, Eu, Th and U on argillaceous rocks using sorption models for illite. *Applied Geochemistry* **2015**, 59, 189-199.

- (22) Chakraborty, S.; Favre, F.; Banerjee, D.; Scheinost, A. C.; Mullet, M.; Ehrhardt, J.-J.; Brendle, J.; Vidal, L.; Charlet, L. U(VI) Sorption and Reduction by Fe(II) Sorbed on Montmorillonite. *Environmental Science & Technology* **2010**, *44* (10), 3779-3785.
- (23) Fröhlich, D. R. SORPTION OF NEPTUNIUM ON CLAYS AND CLAY MINERALS – A REVIEW. *Clays and Clay Minerals* **2015**, *63* (4), 262-276.
- (24) Elo, O. Neptunium (V) interactions with the bentonite clay barrier constituents bentonite, montmorillonite, corundum and granitic host rock. **2019**.
- (25) Peretyazhko, T.; Zachara, J. M.; Heald, S. M.; Jeon, B. H.; Kukkadapu, R. K.; Liu, C.; Moore, D.; Resch, C. T. Heterogeneous reduction of Tc(VII) by Fe(II) at the solid–water interface. *Geochimica et Cosmochimica Acta* **2008**, *72* (6), 1521-1539.
- (26) Yang, J.; Kukkadapu, R. K.; Dong, H.; Shelobolina, E. S.; Zhang, J.; Kim, J. Effects of redox cycling of iron in nontronite on reduction of technetium. *Chemical Geology* **2012**, *291*, 206-216.
- (27) Jaisi, D. P.; Dong, H.; Plymale, A. E.; Fredrickson, J. K.; Zachara, J. M.; Heald, S.; Liu, C. Reduction and long-term immobilization of technetium by Fe(II) associated with clay mineral nontronite. *Chemical Geology* **2009**, *264* (1), 127-138.
- (28) Bishop, M. E.; Dong, H.; Kukkadapu, R. K.; Liu, C.; Edelman, R. E. Bioreduction of Fe-bearing clay minerals and their reactivity toward pertechnetate (Tc-99). *Geochimica et Cosmochimica Acta* **2011**, *75* (18), 5229-5246.
- (29) Scheinost, A. C.; Kirsch, R.; Banerjee, D.; Fernandez-Martinez, A.; Zaenker, H.; Funke, H.; Charlet, L. X-ray absorption and photoelectron spectroscopy investigation of selenite reduction by FeII-bearing minerals. *Journal of Contaminant Hydrology* **2008**, *102* (3), 228-245.
- (30) Charlet, L.; Scheinost, A. C.; Tournassat, C.; Greneche, J.-M.; GÉhin, A.; Fernandez-Martinez, A.; Coudert, S.; Tisserand, D.; Brendle, J. Electron transfer at the mineral/water interface: Selenium reduction by ferrous iron sorbed on clay. *Geochimica et Cosmochimica Acta* **2007**, *71* (23), 5731–5749.
- (31) Neumann, A.; Sander, M.; Hofstetter, T. B. Redox Properties of Structural Fe in Smectite Clay Minerals. In *Aquatic Redox Chemistry*, ACS Symposium Series, Vol. 1071; American Chemical Society, 2011; pp 361-379.

- (32) Stucki, J. W.; Goodman, B. A.; Schwertmann, U. *Iron in soils and clay minerals*; Kluwer Academic Publishers, 1988.
- (33) Stucki, J. W. Chapter 8 Properties and Behaviour of Iron in Clay Minerals. In *Developments in Clay Science*, Bergaya, F., Theng, B. K. G., Lagaly, G. Eds.; Vol. 1; Elsevier, 2006; pp 423-475.
- (34) Besson, G.; Bookin, A.; Dainyak, L.; Rautureau, M.; Tsipursky, S.; Tchoubar, C. t.; Drits, V. Use of diffraction and Mössbauer methods for the structural and crystallochemical characterization of nontronites. *Journal of Applied Crystallography* **1983**, 16 (4), 374-383.
- (35) Goodman, B. A.; Russell, J. D.; Fraser, A. R.; Woodhams, F. W. D. A Mössbauer and I.R. Spectroscopic Study of the Structure of Nontronite. *Clays and Clay Minerals* **1976**, 24 (2), 53-59.
- (36) Bonnin, D.; Calas, G.; Suquet, H.; Pezerat, H. Sites occupancy of Fe<sup>3+</sup> in Garfield Nontronite: A spectroscopic study. *Physics and Chemistry of Minerals* **1985**, 12 (1), 55-64.
- (37) Cardile, C. M.; Johnston, J. H. Structural Studies of Nontronites with Different Iron Contents by <sup>57</sup>Fe Mössbauer Spectroscopy. *Clays and Clay Minerals* **1985**, 33 (4), 295-300.
- (38) Murad, E. Mössbauer spectra of nontronites: Structural implications and characterization of associated iron oxides. *Zeitschrift für Pflanzenernährung und Bodenkunde* **1987**, 150 (5), 279-285.
- (39) Manceau, A.; Lanson, B.; Drits, V. A.; Chateigner, D.; Gates, W. P.; Wu, J.; Huo, D.; Stucki, J. W. Oxidation-reduction mechanism of iron in dioctahedral smectites: I. Crystal chemistry of oxidized reference nontronites. *American Mineralogist* **2000**, 85 (1), 133-152.
- (40) Muller, F.; Besson, G.; Manceau, A.; Drits, V. A. Distribution of isomorphous cations within octahedral sheets in montmorillonite from Camp-Bertaux. *Physics and Chemistry of Minerals* **1997**, 24 (3), 159-166.
- (41) Neumann, A.; Petit, S.; Hofstetter, T. B. Evaluation of redox-active iron sites in smectites using middle and near infrared spectroscopy. *Geochimica et Cosmochimica Acta* **2011**, 75 (9), 2336-2355.
- (42) Sainz-Diaz, C. I.; Hernández-Laguna, A.; Dove, M. T. Theoretical modelling of cis-vacant and trans-vacant configurations in the octahedral sheet of illites and smectites. *Physics and Chemistry of Minerals* **2001**, 28 (5), 322-331.

- (43) Lear, P. R.; Stucki, J. W. Role of Structural Hydrogen in the Reduction and Reoxidation of Iron in Nontronite. *Clays and Clay Minerals* **1985**, 33 (6), 539-545.
- (44) Stucki, J. W.; Golden, D. C.; Roth, C. B. Effects of Reduction and Reoxidation of Structural Iron on the Surface Charge and Dissolution of Dioctahedral Smectites. *Clays and Clay Minerals* **1984**, 32 (5), 350-356.
- (45) Manceau, A.; Drits, V. A.; Lanson, B.; Chateigner, D.; Wu, J.; Huo, D.; Gates, W. P.; Stucki, J. W. Oxidation-reduction mechanism of iron in dioctahedral smectites: II. Crystal chemistry of reduced Garfield nontronite. *American Mineralogist* **2000**, 85 (1), 153-172.
- (46) Liu, D.; Tian, Q.; Yuan, P.; Du, P.; Zhou, J.; Li, Y.; Bu, H.; Zhou, J. Facile sample preparation method allowing TEM characterization of the stacking structures and interlayer spaces of clay minerals. *Applied Clay Science* **2019**, 171, 1-5.
- (47) Kogure, T. Visualization of clay minerals at the atomic scale. *Clay Minerals* **2020**, 55 (3), 203-218.
- (48) SOURCE CLAY PHYSICAL/CHEMICAL DATA;  
<https://www.agry.purdue.edu/cjohnston/sourceclays/chem.htm>.
- (49) Rojas-Mantilla, H. D.; Ayala-Duran, S. C.; Pupo Nogueira, R. F. Nontronite mineral clay N<sub>Au</sub>-2 as support for hematite applied as catalyst for heterogeneous photo-Fenton processes. *Chemosphere* **2021**, 277, 130258.
- (50) Baeyens, B.; Bradbury, M. H. A mechanistic description of Ni and Zn sorption on Namontmorillonite Part I: Titration and sorption measurements. *Journal of Contaminant Hydrology* **1997**, 27 (3), 199-222.
- (51) Stucki, J.; Golden, D.; Roth, C. Preparation and Handling of Dithionite-Reduced Smectite Suspensions. *Clays and Clay Minerals - CLAYS CLAY MINER* **1984**, 32, 191-197.
- (52) Grangeon, S.; Warmont, F.; Tournassat, C.; Lanson, B.; Lanson, M.; Elkaïm, E.; Claret, F. Nucleation and growth of feiknechtite from nanocrystalline vernadite precursor. *European Journal of Mineralogy* **2017**, 29 (4), 767-776.
- (53) Agnel, M. I.; Grangeon, S.; Fauth, F.; Elkaïm, E.; Claret, F.; Roulet, M.; Warmont, F.; Tournassat, C. Mechanistic and Thermodynamic Insights into Anion Exchange by Green Rust. *Environmental Science & Technology* **2020**, 54 (2), 851-861.
- (54) Miller, D. J.; Biesinger, M. C.; McIntyre, N. S. Interactions of CO<sub>2</sub> and CO at fractional

- atmosphere pressures with iron and iron oxide surfaces: one possible mechanism for surface contamination? *Surface and Interface Analysis* **2002**, 33 (4), 299-305.
- (55) Piao, H.; McIntyre, N. S. Adventitious carbon growth on aluminium and gold–aluminium alloy surfaces. *Surface and Interface Analysis* **2002**, 33 (7), 591-594.
- (56) Scheinost, A. C.; Claussner, J.; Exner, J.; Feig, M.; Findeisen, S.; Hennig, C.; Kvashnina, K. O.; Naudet, D.; Prieur, D.; Rossberg, A.; et al. ROBL-II at ESRF: A synchrotron toolbox for actinide research. *J. Synchrotron Rad.* **2021**, 28, 333-349.
- (57) Webb, S. M. SIXpack: a graphical user interface for XAS analysis using IFEFFIT. *Physica Scripta* **2005**, 2005 (T115), 1011.
- (58) Ressler, T. WinXAS: A program for X-ray absorption spectroscopy data analysis under MS-Windows. *Journal of Synchrotron Radiation* **1998**, 5 (2), 118-122, Article.
- (59) Rehr, J. J.; Kas, J. J.; Vila, F. D.; Prange, M. P.; Jorissen, K. Parameter-free calculations of X-ray spectra with FEFF9. *Physical Chemistry Chemical Physics* **2010**, 12 (21), 5503-5513, 10.1039/B926434E.
- (60) Manceau, A.; Chateigner, D.; Gates, W. P. Polarized EXAFS, distance-valence least-squares modeling (DVLS), and quantitative texture analysis approaches to the structural refinement of Garfield nontronite. *Physics and Chemistry of Minerals* **1998**, 25 (5), 347-365.
- (61) Agote-Arán, M.; Lezcano-González, I.; Greenaway, A. G.; Hayama, S.; Díaz-Moreno, S.; Kroner, A. B.; Beale, A. M. Operando HERFD-XANES/XES studies reveal differences in the activity of Fe-species in MFI and CHA structures for the standard selective catalytic reduction of NO with NH<sub>3</sub>. *Applied Catalysis A: General* **2019**, 570, 283-291.
- (62) Wilke, M.; Farges, F.; Petit, P.-E.; Brown, G. E.; Martin, F. Oxidation state and coordination of Fe in minerals: An Fe K-XANES spectroscopic study. *American Mineralogist* **2001**, 86 (5-6), 714-730.
- (63) Rossberg, A.; Reich, T.; Bernhard, G. Complexation of uranium (VI) with protocatechuic acid—application of iterative transformation factor analysis to EXAFS spectroscopy. *Analytical and bioanalytical chemistry* **2003**, 376 (5), 631-638.
- (64) Ravel, B.; Newville, M. ATHENA, ARTEMIS, HEPHAESTUS: data analysis for X-ray absorption spectroscopy using IFEFFIT. *Journal of Synchrotron Radiation* **2005**, 12 (4), 537-541.

- (65) Gorski, C. A.; Aeschbacher, M.; Soltermann, D.; Voegelin, A.; Baeyens, B.; Marques Fernandes, M.; Hofstetter, T. B.; Sander, M. Redox properties of structural Fe in clay minerals. 1. Electrochemical quantification of electron-donating and -accepting capacities of smectites. *Environ Sci Technol* **2012**, *46* (17), 9360-9368.
- (66) Jaisi, D. P.; Dong, H.; Morton, J. P. Partitioning of Fe(II) in reduced nontronite (NAu-2) to reactive sites: Reactivity in terms of Tc(VII) reduction. *Clays and Clay Minerals* **2008**, *56* (2), 175-189.
- (67) Hadi, J.; Tournassat, C.; Ignatiadis, I.; Greneche, J. M.; Charlet, L. Modelling CEC variations versus structural iron reduction levels in dioctahedral smectites. Existing approaches, new data and model refinements. *Journal of Colloid and Interface Science* **2013**, *407*, 397-409.
- (68) Brigatti, M. F.; Galán, E.; Theng, B. K. G. Chapter 2 - Structure and Mineralogy of Clay Minerals. In *Developments in Clay Science*, Bergaya, F., Lagaly, G. Eds.; Vol. 5; Elsevier, 2013; pp 21-81.
- (69) Yuan, S.; Liu, X.; Liao, W.; Zhang, P.; Wang, X.; Tong, M. Mechanisms of electron transfer from structural Fe(II) in reduced nontronite to oxygen for production of hydroxyl radicals. *Geochimica et Cosmochimica Acta* **2018**, *223*, 422-436.
- (70) Charlet, L.; Tournassat, C.; Grenèche, J.-M.; Wersin, P.; Géhin, A.; Hadi, J. Mössbauer spectrometry insights into the redox reactivity of Fe-bearing phases in the environment. *Journal of Materials Research* **2022**.
- (71) Gorski, C. A.; Klupfel, L.; Voegelin, A.; Sander, M.; Hofstetter, T. B. Redox properties of structural Fe in clay minerals. 2. Electrochemical and spectroscopic characterization of electron transfer irreversibility in ferruginous smectite, SWa-1. *Environ Sci Technol* **2012**, *46* (17), 9369-9377.
- (72) Ilgen, A. G.; Kukkadapu, R. K.; Dunphy, D. R.; Artyushkova, K.; Cerrato, J. M.; Kruichak, J. N.; Janish, M. T.; Sun, C. J.; Argo, J. M.; Washington, R. E. Synthesis and characterization of redox-active ferric nontronite. *Chemical Geology* **2017**, *470*, 1-12.
- (73) Qiang, S.; Wang, J.; Wang, Y.; Yuan, L.; Shi, L.; Ding, Z.; Wang, W.; Liang, J.; Li, P.; Fan, Q. Analysis of the uranium chemical state by XPS: Is what you see real? *Applied Surface Science* **2022**, *576*, 151886.



- (74) Soltermann, D.; Marques Fernandes, M.; Baeyens, B.; Dahn, R.; Joshi, P. A.; Scheinost, A. C.; Gorski, C. A. Fe(II) uptake on natural montmorillonites. I. Macroscopic and spectroscopic characterization. *Environ Sci Technol* 2014, 48 (15), 8688-8697.
- (75) Yalçıntaş, E.; Scheinost, A. C.; Gaona, X.; Altmaier, M. Systematic XAS study on the reduction and uptake of Tc by magnetite and mackinawite. *Dalton Trans.* **2016**, 45, 17874-17885.
- (76) Gaur, A.; Shrivastava, B. D. Speciation using X-ray absorption fine structure (XAFS). *Review Journal of Chemistry* **2015**, 5 (4), 361-398.
- (77) Shannon, R. D. Revised effective ionic radii and systematic studies of interatomic distances in halides and chalcogenides. *Acta Crystallogr. Sect. A* **1976**, 32 (SEP1), 751-767, Article.
- (78) Schaefer, M. V.; Gorski, C. A.; Scherer, M. M. Spectroscopic Evidence for Interfacial Fe(II)-Fe(III) Electron Transfer in a Clay Mineral. *Environ. Sci. Technol.* 2011, 45 (2), 540–545.
- (79) Hofstetter, T. B.; Sosedova, Y.; Gorski, C.; Voegelin, A.; Sander, M. *Redox properties of iron-bearing clays and MX-80 bentonite – Electrochemical and spectroscopic characterization*; NTB--13-03; Switzerland, 2014.
- (80) Berry, A. J.; O'Neill, H. S. C.; Jayasuriya, K. D.; Campbell, S. J.; Foran, G. J. XANES calibrations for the oxidation state of iron in a silicate glass. *American Mineralogist* **2003**, 88 (7), 967-977.
- (81) McHergui, C.; Besaury, L.; Langlois, E.; Aubert, M.; Akpa-Vinceslas, M.; Buatois, B.; Quillet, L.; Bureau, F. A comparison of permanent and fluctuating flooding on microbial properties in an ex-situ estuarine riparian system. *Applied Soil Ecology* **2014**, 78, 1-10.
- (82) Reddy, K. R.; Patrick, W. H. Effect of alternate aerobic and anaerobic conditions on redox potential, organic matter decomposition and nitrogen loss in a flooded soil. *Soil Biology and Biochemistry* **1975**, 7 (2), 87-94.
- (83) Hagedorn, F.; Kaiser, K.; Feyen, H.; Schleppi, P. Effects of redox conditions and flow processes on the mobility of dissolved organic carbon and nitrogen in a forest soil. *JOURNAL OF ENVIRONMENTAL QUALITY* **2000**, 29 (1), 288-297.
- (84) Marschner, P. Processes in submerged soils – linking redox potential, soil organic matter turnover and plants to nutrient cycling. *Plant and Soil* **2021**, 464 (1), 1-12.
- (85) Yoshida, H.; Metcalfe, R.; Yamamoto, K.; Murakami, Y.; Hoshii, D.; Kanekiyo, A.;

Naganuma, T.; Hayashi, T. Redox front formation in an uplifting sedimentary rock sequence: An analogue for redox-controlling processes in the geosphere around deep geological repositories for radioactive waste. *Applied Geochemistry* **2008**, 23 (8), 2364-2381.

2.6 Supporting information



Figure S2.1. Photographs of nontronite clay suspensions stored in infusion bottles in the glovebox. (a) Native NAu-2, (b) high-red NAu-2, (c) low-red NAu-2.

Table S2.1. XPS fitting results of native NAu-2, low-red NAu-2, and high-red NAu-2.

Sample	Fe2p <sub>3/2</sub> species	Binding energy (eV)	FWHM (eV)	Area (cps·eV)	Atomic %
Native NAu-2	Fe(II)-O1	708.7	1.50	388	1.31
	Fe(II)-O2	709.5	1.70	545	1.85
	Fe(II)-O3	711.1	1.70	264	0.89
	Fe(II)-O4	711.9	2.82	724	2.46
	Fe(II)-O5	715.2	2.30	137	0.46
	Fe(III)-O1	711.6	1.75	12629	42.84
	Fe(III)-O2	712.8	1.95	8448	28.67
	Fe(III)-O3	713.8	1.95	4224	14.34
	Fe(III)-O4	715.0	1.95	2112	7.17
Low-red NAu-2	Fe(II)-O1	708.9	1.50	2601	4.58
	Fe(II)-O2	709.5	1.70	3653	6.43
	Fe(II)-O3	711.1	1.70	1768	3.11
	Fe(II)-O4	711.9	2.82	4854	8.55
	Fe(II)-O5	715.2	2.30	917	1.62
	Fe(III)-O1	712.0	1.75	19791	34.87
	Fe(III)-O2	713.1	1.95	13238	23.33
	Fe(III)-O3	714.2	1.95	6619	11.67
	Fe(III)-O4	715.1	1.95	3310	5.84
High-red NAu-2	Fe(II)-O1	708.7	1.50	4908	8.67
	Fe(II)-O2	709.9	1.70	6895	12.19
	Fe(II)-O3	711.1	1.70	3336	5.90
	Fe(II)-O4	711.9	2.82	9161	16.20
	Fe(II)-O5	715.2	2.30	1730	3.06
	Fe(III)-O1	711.6	1.75	14054	24.86
	Fe(III)-O2	712.8	1.95	9401	16.64
	Fe(III)-O3	713.8	1.95	4700	8.32
	Fe(III)-O4	714.8	1.95	2350	4.16

Table S2.2. Fitting results of the Fe-K main-edge in Figure 6a by ITFA (non-normalized to unity) and by linear combination fitting (LCF, normalized to unity) using native NAu-2 as standard for Fe(III) and red SWy-2 as standard for Fe(II).

Sample	ITFA		LCF		
	Fe(III)	Fe(II)	Fe(III)	Fe(II)	R factor
Native NAu-2	1.00	0.00	1.00	0.00	
Low-red NAu-2	0.86	0.15	0.86	0.14	0.0005
High-red NAu-2	0.47	0.51	0.52	0.48	0.0051

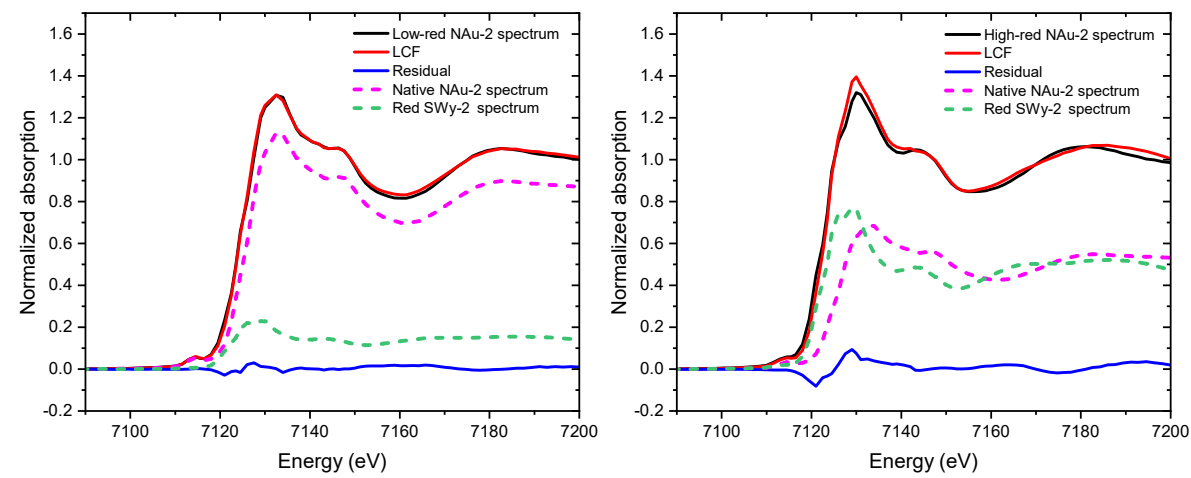


Figure S2.2. Linear combination fit of (a) low-red NAu-2 and (b) high-red NAu-2 spectra using the XANES spectra of native NAu-2 and red SWy-2 as standards for structural Fe(III) and Fe(II), respectively.

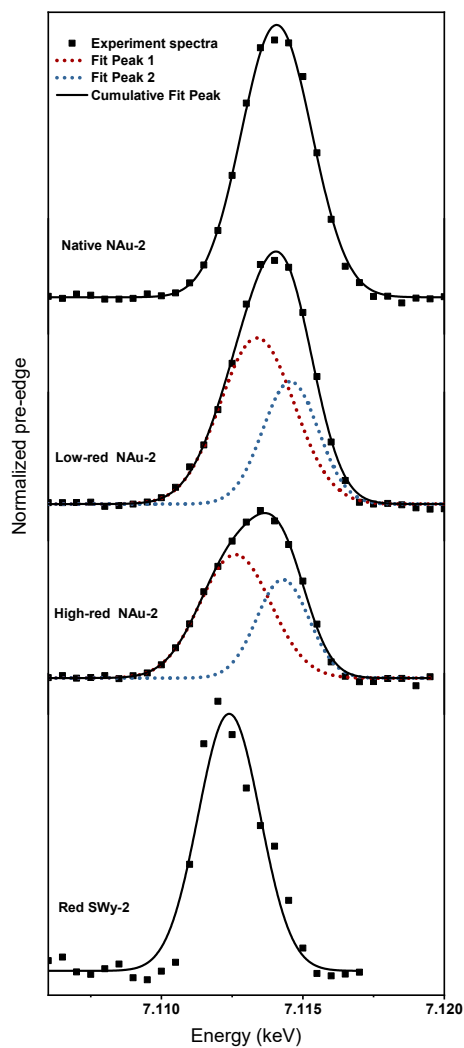


Figure S2.3. Voigt deconvolution of normalized pre-edge.

Table S2.3. Voigt deconvolution of normalized Fe-K pre-edge peaks.

Sample	Peak position (keV)	FWHM (keV)	Area	Total area	Centroid (keV)	R <sup>2</sup>
Native NAu-2	7.11407	0.00293	1.12E-04	1.12E-04	7.11407	0.9964
Low-red NAu-2	7.11338	0.00308	7.19E-05	1.12E-04	7.11380	0.9975
	7.11456	0.00231	3.99E-05			
High-red NAu-2	7.11261	0.00295	5.12E-05	8.13E-05	7.11323	0.9971
	7.11429	0.00217	3.01E-05			
Red SWy-2	7.11240	0.00258	4.58E-05	3.08E-05	7.11240	0.9391

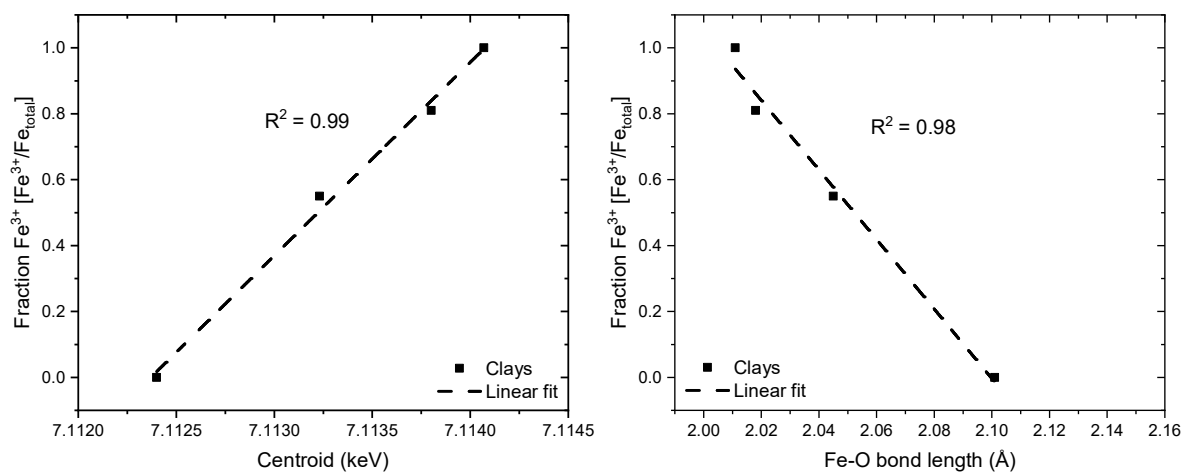


Figure S2.4. (a) Correlation between Mössbauer-determined Fe(III) fraction (y-axis) and pre-edge centroid (x-axis) with regression equation  $y = 586.7x - 4173$ . (b) Correlation between Mössbauer measured Fe(III) fraction (y-axis) and Fe-O bond length derived by EXAFS shell fit (x-axis) bond length with regression equation  $y = -10.6x + 22.2$ .

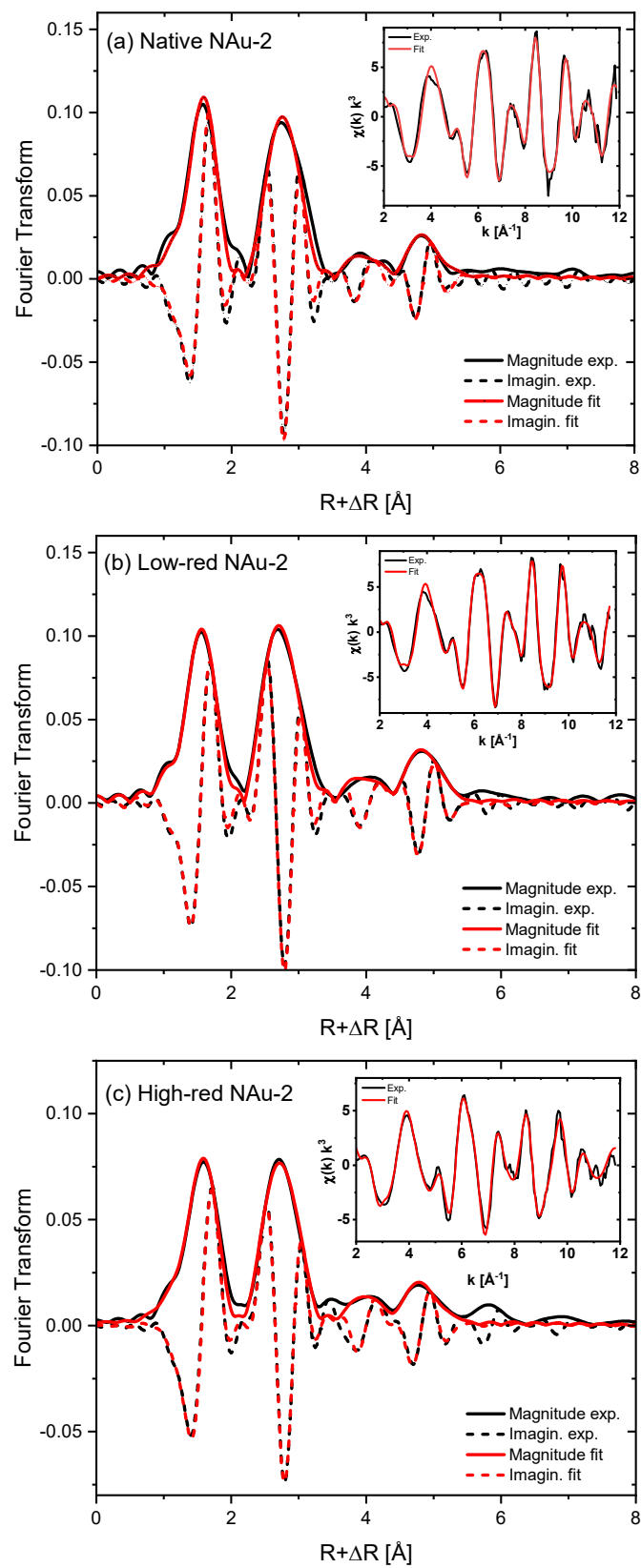


Figure S2.5. Fe K-edge EXAFS fitted spectra.

**Chapter 3: Influence of structural Fe content in clay  
minerals on selenite redox reactions: kinetics and  
structural transformations**

*Manuscript has been submitted in Geochimica et Cosmochimica Acta.*



# Influence of structural Fe content in clay minerals on selenite redox reactions: kinetics and structural transformations

Yanting Qian<sup>1,2</sup>, Andreas C. Scheinost<sup>3a,b</sup>, Sylvain Grangeon<sup>4</sup>, Alwina Hoving<sup>5</sup>, Sergey V. Churakov<sup>1,2</sup>, Maria Marques Fernandes<sup>1,\*</sup>

<sup>1</sup>Laboratory for Waste Management, Paul Scherrer Institut, CH-5232 Villigen PSI, Switzerland

<sup>2</sup>Institute for Geological Sciences, University of Bern, CH-3012 Bern, Switzerland

<sup>3a</sup>The Rossendorf Beamline at the European Synchrotron Radiation Facility (ESRF), Avenue des Martyrs 71, 38043, Grenoble, France

<sup>3b</sup>Helmholtz Zentrum Dresden Rossendorf, Institute of Resource Ecology, Bautzner Landstrasse 400, 01328, Dresden, Germany

<sup>4</sup>BRGM – French Geological Survey, 45060 Orléans, France

<sup>5</sup>TNO Geological Survey of the Netherlands, PO Box 80015, 3508 TA Utrecht, the Netherlands

\*Corresponding author. E-mail address: [maria.marques@psi.ch](mailto:maria.marques@psi.ch);

Keywords: selenite reduction; Fe(II)-bearing clay minerals; red and grey elemental Se(0); kinetics; redox potential

## Abstract

Redox reactions control the environmental fate of selenium, an element of concern due to its small gap between beneficial and detrimental effects on human health and due to the longevity of the radionuclide <sup>79</sup>Se produced in nuclear reactors. Fe-bearing clay minerals are major redox-active ingredients of Earth's critical zone and constitute an important component of the barrier in (radioactive and other) waste repositories. Here we systematically investigate selenite (Se(IV)O<sub>3</sub><sup>2-</sup>) sorption and reduction by Fe-bearing clay minerals of the smectite group, using batch experiments and X-ray absorption fine structure (XAFS) spectroscopy to elucidate reaction mechanisms and kinetics up to 720 or 3600 h. We found a linear relationship between structural Fe(II) content and selenite reduction rate. Selenite reduction depends also on redox potential and pH, with pH 7 showing a slower

reduction rate as compared to pH 5. Selenite first sorbed to clay edge sites by forming an inner-sphere sorption complex, before being reduced to Se(0). The first redox product was amorphous (red) Se(0), which gradually transformed into trigonal (grey) Se(0). Despite an  $\text{Fe}^{2+}_{\text{aq}}$  concentration of up to  $6 \times 10^{-4}$  M in the clay suspension depending on the pH and on the Fe content of the clay, we did not observe formation of iron selenides. This insight into the selenite reduction mechanism provides valuable information for the development of effective approaches for selenite immobilization.

### 3.1 Introduction

Selenium (Se) is a rare element in the earth's crust (0.05 mg/kg) and an important micronutrient for humans, having impact on cell function, antioxidant and immune systems (Titov et al., 2022). The gap between deficiency (<40 µg/day) and toxicity (>400 µg/day) of Se is very narrow (Winkel et al., 2012). Se deficiency can cause a series of health issues including hormonal imbalance in the thyroid, growth retardation, poor immune function, cancer, and increased mortality (Moreno-Reyes et al., 2001; Rayman, 2012). Endemic Se deficiency has been reported in China (Li et al., 2012) and Russia (Volfson et al., 2010). A daily dietary Se supplement of ~200 µg/day is recommended to prevent health issues (Hammouh et al., 2021). In contrast to Se deficiency, excess Se leads to Se poisoning symptoms such as garlic odor breath, discoloration of the skin, hair loss, fatigue, nausea, vomiting, and neurodegeneration (MacFarquhar et al., 2010).

Se is emitted into the ecosystem through both natural sources and anthropogenic activities. In terms of natural sources, Se is primarily found in sedimentary rocks and marine shale deposits, where it commonly exists as metal selenides and forms a minor part of metal-sulfur minerals. The weathering of these seleniferous rocks leads to Se oxidation and release into the environment (Fernández-Martínez and Charlet, 2009). Furthermore, volatilization by plants, bacteria and volcanic eruptions contribute to the natural release of Se in the gas phase. As for anthropogenic sources, Se originates from activities such as coal and oil combustion facilities, selenium refining plants, base metal smelting and refining plants, mining and milling operations, as well as various end-product manufacturers (e.g., glass, semiconductors, and photovoltaic cells) (Fordyce, 2013; Tan et al., 2018). Besides the stable Se isotopes, radioactive  $^{79}\text{Se}$  is a long-lived ( $t_{1/2} = 3.27 \cdot 10^5$  years) fission product present in nuclear fuel (Bingham et al., 2011; Frechou et al., 2007). While Se occurs in the -II oxidation state in spent nuclear fuel (Curti et al., 2015), it is present in IV oxidation state in simulated

vitrified waste (Curti et al., 2013).

Se deficiency and excess are highly influenced by the bioavailability of Se species in the environment, which in turn depends on the Se oxidation state. Se exists in five oxidation states: -II (selenide,  $\text{Se}^{2-}$ ), -I (diselenide), 0 (elemental selenium), IV (selenite,  $\text{SeO}_3^{2-}$ ), and VI (selenate,  $\text{SeO}_4^{2-}$ ) (Ma et al., 2019). Selenate and selenite predominate at relatively high redox potential and are very soluble and mobile. Selenic ( $\text{H}_2\text{SeO}_4$ ) and selenous ( $\text{H}_2\text{SeO}_3$ ) acid are diprotic acids (Zoroufchi Benis et al., 2022) and the presence of their oxyanions  $\text{HSeO}_4^-$ ,  $\text{HSeO}_3^-$ ,  $\text{SeO}_3^{2-}$  depends on the solution pH (Séby et al., 2001). Elemental Se(0) is present at mild reducing redox potential as a stable non-soluble form, which can exhibit both amorphous and crystalline solids: red amorphous Se(0), and crystalline deep-red monoclinic and grey trigonal Se(0) (Fernández-Martínez and Charlet, 2009). Se(-I) and Se(-II) exist in reducing environment depending on pH as  $\text{H}_2\text{Se}$ ,  $\text{HSe}^-$ ,  $\text{Se}^{2-}$ , polyselenides  $\text{Se}_n^{2-}$ , and as poorly soluble metal selenides (Rojo et al., 2018; Scheinost and Charlet, 2008; Scheinost et al., 2008; W. Hummel, 2023). In contrast to the  $\text{HSe}^-$  anion (which is stable only in Fe-free systems),  $\text{FeSe}_x$  species have a low solubility ( $\log K(\text{FeSe}_2) = -13.4$ ,  $\log K(\text{FeSe}) = -0.4$  (W. Hummel, 2023)), so in general, reduction is an efficient way to immobilize soluble Se.

Reduction of Se has been observed biotically and abiotically. Various bacteria carry out dissimilatory reduction to elemental Se(0) by using oxidized Se as electron acceptors to oxidize organic matter (Oremland and Stolz, 2000). Moreover, Se is also reduced abiotically by Fe minerals including magnetite (Jordan et al., 2009), mackinawite (Scheinost et al., 2008), and siderite (Scheinost and Charlet, 2008), green rust (Myneni et al., 1997), pyrite (Charlet et al., 2012; Curti et al., 2013; Rodriguez et al., 2020), troilite (Breynaert et al., 2008), Fe sorbed clay (Charlet et al., 2007), and zerovalent Fe(0) (Olegario et al., 2010). In the presence of above Fe(II)-bearing minerals, Se can be reduced to mostly red and grey elemental Se(0) and sometimes various iron selenides ( $\text{FeSe}$ ) (Scheinost and Charlet, 2008) but rarely the most thermodynamically stable ferroselite ( $\text{FeSe}_2$ ) (Charlet et al., 2012). The reduction is thought to proceed through a combined adsorption and redox process, since aqueous  $\text{Fe}^{2+}$  has little tendency to reduce selenite and selenate (Börsig et al., 2017; Charlet et al., 2012; Frasca et al., 2014). Selenite can be adsorbed through inner-sphere and outer-sphere complexation, depending on adsorbent and pH (Fernández-Martínez and Charlet, 2009; Jordan et al., 2014; Jordan et al., 2013). The reduction process and the final reduced Se species are governed by several factors such as pH, redox potential, kinetics, Se concentration, mineralogical composition of the environment, and biological interactions.

Details about the reduction mechanism with respect to the electron transfer process and the control on the reduced species remain still vague, especially for the abiotic, mineral-surface-driven systems. Since batch sorption experiments are rarely sufficient to derive reduction mechanism, spectroscopic investigations such as X-ray absorption fine structure (XAFS) spectroscopy, including X-ray absorption near edge structure (XANES) and extended X-ray absorption fine structure (EXAFS), are now commonly used to elucidate both oxidation state and local structure of intermediate and final Se species. Furthermore, the reduction processes of selenite and to an even larger extent of selenate are slow and the reduced species may vary over time (Poulain et al., 2022). Therefore, long-term kinetic studies are needed to gain a better understanding of the reduction process from the early transient to long-term equilibrium states.

In this study, we investigate the role of structural Fe in clay minerals on the selenite reduction mechanism. Depending on its redox state, structural iron in clay minerals affects the physicochemical properties of clay minerals and is known to oxidize or reduce elements at their surface (by acting either as an electron donor or acceptor) thus altering their mobility and/or (bio)availability (Huang et al., 2021). We focus here on swelling clays of the smectite group, using reference samples provided by the Clay Source Repository of the Clay Minerals Society (Van Olphen et al., 1979), namely two natural montmorillonites (SWy-2 from Wyoming and STx-1 from Texas) because of their relevance for engineered barrier systems for radioactive waste repositories, and in addition a nontronite (NAu-2 from Australia), a natural Fe rich smectite, because of the abundant literature and datasets concerning its redox reactivity. We perform sorption experiments on these clay minerals reduced to different Fe(II)/Fe(III) ratios, to quantify the sorption and sorption kinetics of selenite on clay minerals. By applying XAFS, we would like to (1) to follow the selenite reduction process, (2) identify the structure of sorbed species, and (3) elucidate the role of aqueous solution chemistry including pH and redox potential, to contribute to a wider understanding of Se immobilization in the environment.

## **3.2 Materials and methods**

### **3.2.1 Clays**

Three dioctahedral smectite clays with different Fe content, Texas montmorillonite STx-1, Wyoming montmorillonite SWy-2, and south Australian nontronite NAu-2, were purchased from the Clay Source Repository of the Clay Minerals Society (Purdue

University, West Lafayette, IN). The chemical composition, structure, and Fe content of the raw material as provided by the Clay Mineral Society are listed in Table 3.1. The as-received clay materials were washed and purified to a homogeneous Na-form clay suspension in 0.1 M NaCl electrolyte. The detailed procedures are described in previous work (Qian et al., 2023).

Table 3.1. Chemical composition and structure of STx-1, SWy-2, and NAu-2 provided by the Clay Minerals Society (Van Olphen et al., 1979)

Clay	Chemical formula. The first round bracket denominates the charge-compensating interlayer cations, the first square bracket the octahedrally coordinated cations, and the second square bracket the tetrahedrally coordinated cations of the TOT layers
STx-1	$(\text{Ca}_{0.27}\text{Na}_{0.04}\text{K}_{0.01})[\text{Al}_{2.41}\text{Fe(III)}_{0.09}\text{Mn}_{\text{tr}}\text{Mg}_{0.71}\text{Ti}_{0.03}][\text{Si}_{8.00}]\text{O}_{20}(\text{OH})_4$
SWy-2	$(\text{Ca}_{0.12}\text{Na}_{0.32}\text{K}_{0.5})[\text{Al}_{3.01}\text{Fe(III)}_{0.41}\text{Mn}_{0.01}\text{Mg}_{0.54}\text{Ti}_{0.02}][\text{Si}_{7.98}\text{Al}_{0.02}]\text{O}_{20}(\text{OH})_4$
NAu-2	$(\text{M}^{+0.97})[\text{Al}_{0.52}\text{Fe}_{3.32}\text{Mg}_{0.7}][\text{Si}_{7.57}\text{Al}_{0.01}\text{Fe}_{0.42}]\text{O}_{20}(\text{OH})_4$

### 3.2.2 Preparation of reduced clay suspensions

The three clay minerals were chemically reduced to obtain different Fe(II) contents associated with different redox potential (Eh) (Gorski et al., 2013). The reduction was conducted by the Citrate-Bicarbonate-Dithionite (CBD) method following Stucki et al. (Stucki et al., 1984a) yet without heating. Purified clay suspensions were degassed with nitrogen gas (N<sub>2</sub>) for two hours before transferring them into a N<sub>2</sub>-atmosphere controlled anoxic glovebox (O<sub>2</sub> < 0.1 ppm). The complete reduction process was conducted in the glovebox. For STx-1, 500 mL clay suspension (22.18 g/L) were first mixed with a citrate-bicarbonate (CB) buffer solution (12 mL of 0.5 M Na<sub>3</sub>C<sub>6</sub>H<sub>5</sub>O<sub>7</sub>·2H<sub>2</sub>O and 164 mL of 1 M NaHCO<sub>3</sub>) in an infusion bottle for about an hour stirring. Afterwards, 2 g dithionite (Na<sub>2</sub>S<sub>2</sub>O<sub>4</sub>) and 24 mL 0.1 M NaCl were added to a total volume of 700 mL. For SWy-2, the same procedures were carried out with 1 L clay suspension (14.32 g/L), 500 mL of 1 M Na<sub>3</sub>C<sub>6</sub>H<sub>5</sub>O<sub>7</sub>·2H<sub>2</sub>O, 250 mL of 1 M NaHCO<sub>3</sub>, and 34.52 g Na<sub>2</sub>S<sub>2</sub>O<sub>4</sub> with a total volume of 1700 mL. The clay suspensions were stirred for about one day after adding dithionite. After reduction, clay suspensions were washed in dialysis bags first with 1 M NaCl at pH 4 to remove added chemicals and dissolved elements, and then with 0.1 M NaCl without pH adjustment until the concentration of citrate and bicarbonate were less than 10<sup>-9</sup> M. For NAu-

2, two reduction degrees (low-red. N<sub>Au</sub>-2 and high-red. N<sub>Au</sub>-2) were prepared, and the details are described in previous work (Qian et al., 2023). Finally, the suspension of reduced clays in 0.1 M NaCl matrix were stored in the glovebox in infusion bottles covered with aluminum foil to avoid photo oxidation. The chemical composition in weight percentage (wt%) of the as prepared native and reduced samples were determined using X-Ray Fluorescence (XRF) spectroscopy. The Fe(II) wt% content was calculated based on the reduction level of each clay and is presented in Table 3.2.

### 3.2.3 Cation exchange capacity and edge site availability

To ensure that the CBD treatment did not alter the sorption properties of the three clays, their cation exchange capacity (CEC) and their surface complexation ability were quantified. The CEC of native and reduced clays were directly quantified using the highly selective divalent nickeltriethylenediamine (Ni-en) complex radiolabelled with <sup>63</sup>Ni (Peigneur, 1976). At sufficiently high concentration, this index cation is expected to completely displace and replace all the cations present on the exchange sites of clay minerals. The whole experiment was carried out in the glovebox (O<sub>2</sub> < 0.1 ppm) and all the solutions were degassed with N<sub>2</sub> before transferring into the glovebox. A Ni-en solution was prepared as a mixture of nickel nitrate Ni(NO<sub>3</sub>)<sub>2</sub> and ethylene diamine C<sub>2</sub>H<sub>4</sub>(NH<sub>2</sub>)<sub>2</sub> labelled with <sup>63</sup>Ni. The clay suspension (~ 6 g/L) was mixed with <sup>63</sup>Ni-en solution (200 mL 0.02 M Ni-en solution at pH 8 and 50 µL 4.5×10<sup>-5</sup> M <sup>63</sup>Ni tracer solution) in a centrifuge tube (Backman 26 mL) to a total volume of 22 mL. After 4 hours continuously end-to-end shaking, the samples were centrifuged at 40,000 g (Backman Coulter Optima™ L-100 XP Ultracentrifuge, 70 Ti rotor) for one hour. The activity in the supernatant was measured using a beta liquid scintillation counter (Tri-Carb 4910 TR), and the pH was determined using a Metrohm electrode (model: 6.0232.100). The Ni-en adsorbed (Ni-en<sub>ads</sub>) in meq/kg (equal to the CEC) is calculated from the redistribution of the radiotracer between the solid and liquid phases and is calculated from equation (3.1):

$$\text{Ni-en}_{\text{ads}} = \frac{A_{\text{in}} - A_{\text{out}}}{A_{\text{in}}} \cdot \text{Ni-en}_{\text{in}} \quad (3.1)$$

where  $A_{\text{in}}$  = initial <sup>63</sup>Ni activity (cpm),  $A_{\text{out}}$  = final <sup>63</sup>Ni activity (cpm), and  $\text{Ni-en}_{\text{in}}$  = initial amount of Ni-en (in meq/kg).

The availability of the edge sites of native and reduced clays for cation surface complexation was assessed by measuring the sorption of Eu(III) (Baeyens and Bradbury, 2004). This trivalent cation was chosen to avoid competitive sorption effects with Fe(II) (M.

Marques Fernandes and Baeyens, 2020; Soltermann et al., 2014b). Note that although the reducing agents were washed away after reduction,  $\text{Fe}^{2+}$  unavoidably dissolved from the clay itself and established equilibrium with the clay suspension, potentially re-adsorbing onto the clay surfaces depending on pH, which would result in a reduced sorption capacity for other divalent cations, while trivalent cations like Eu(III) are less affected. The sorption of Eu(III) on the samples was quantified by radiochemical assay using  $^{152}\text{Eu}$ . Eu sorption isotherms were measured at a series of Eu concentrations using both active  $^{152}\text{Eu}$  and stable Eu ( $\text{Eu}(\text{NO}_3)_3 \cdot 5\text{H}_2\text{O}$ ) between  $1 \times 10^{-7}$  M to  $2 \times 10^{-4}$  M at 2 g/L and pH  $\sim 7$  in 0.1 M NaCl and equilibrated for 7 days. Due to the high buffering capacity of reduced clays, the pH of the suspensions was adjusted with HCl and NaOH before sorption experiments. Afterwards, Eu solution, clay suspension, pH buffer ( $2 \times 10^{-3}$  M MOPS (3-(N-morpholino) propanesulfonic acid), and 0.1 M NaCl were combined in centrifuge tubes to a total volume of 22 mL and sealed. After 7 days end-to-end continuous shaking, tubes were centrifuged at 40,000 g for one hour to separate the clay and the supernatant. Two aliquots of the supernatant were taken immediately for radiochemical assays of  $^{152}\text{Eu}$  using a gamma counter (WIZARD<sup>2</sup>, 2480). The pH of the supernatant was measured with Metrohm electrodes. Each experiment was carried out in duplicate. The sorbed amount of Eu is calculated by equation (3.2).

$$\text{Sorbed} = [C_{\text{init}}] - [C_{\text{eq}}] \cdot \frac{V}{m} \quad (3.2)$$

Where  $C_{\text{init}}$ : initial concentration of active and inactive Eu (M),  $C_{\text{eq}}$ : equilibrium concentration of active and inactive Eu (M), V: total volume of the liquid phase (L), m: mass of the solid phase (kg).

### 3.2.4 Se sorption kinetics

To quantify the sorption of Se, batch type sorption experiments were carried out in a  $\text{N}_2$  atmosphere controlled anoxic glovebox ( $\text{O}_2 < 0.1$  ppm) at room temperature and over different time periods from 4 hours to 3600 hours. Red. SWy-2 and high-red. NAu-2 are up to 3600 h, while red. STx-1 and low-red. NAu-2 are up to 720 h. A solid to liquid ratio of 2 g/L was used in all the experiments, allowing XAS measurements and sorption quantification under the same conditions.

Sorption kinetics were conducted with a  $\text{Na}_2\text{SeO}_3$  concentration of  $3 \times 10^{-5}$  M at pH 5 in 0.1 M NaCl. This Se concentration was chosen to obtain sorption loadings sufficiently high to be measured by XAFS spectroscopy. The pH of the clay suspensions was adjusted accordingly before sampling experiment. Acetate pH buffer, 0.1 M NaCl, and  $\text{Na}_2\text{SeO}_3$

solution were added to a big infusion bottle. Slow end-to-end shaking was employed. At the end of the different equilibration times, samples were transferred into centrifuge tubes and centrifuged at 40,000 g for one hour to separate the clay from the supernatant. A portion of the supernatant was sampled for Se concentration analysis using ICP-OES and for Fe<sup>2+</sup> concentration ([Fe<sup>2+</sup><sub>eq</sub>]) analysis with phenanthroline (C<sub>12</sub>H<sub>9</sub>ClN<sub>2</sub>·H<sub>2</sub>O) through UV-VIS spectrophotometry. The remaining supernatant was used to measure pH. The clay sediments (wet pastes) were filled in High Density Polyethylene (HDPE) XAFS sample holders and covered with Kapton tape. The sorption of Se is expressed by the logarithm of the solid-liquid distribution coefficient R<sub>d</sub> (mL/g) defined in equation (3.3).

$$R_d = \frac{[C_{init}] - [C_{eq}]}{[C_{eq}]} \cdot \frac{V}{m} \quad (3.3)$$

Where C<sub>init</sub>: initial concentration of Se (M), C<sub>eq</sub>: equilibrium concentration of Se (M), V: total volume of the liquid phase (L), m: mass of the solid phase (kg).

### 3.2.5 X-ray absorption spectroscopy

Clay pastes for XAFS were transferred into a liquid N<sub>2</sub> Dewar for flash freezing right after preparation in the glovebox, where they remained for storage and transport to the beamline to conserve the chemical equilibrium at the sampling state and anoxic conditions. At the beamline, they were quickly transferred to a closed-cycle He cryostat used for the XAFS measurements, always maintaining a frozen state.

The XAFS measurements were conducted at the Rossendorf Beamline (ROBL) BM20 of the European Synchrotron Radiation Facility (ESRF), France (Scheinost et al., 2021). The X-ray beam was monochromatized by a Si(111) double-crystal monochromator, and the energy of monochromator was calibrated with an Au foil using the Au L<sub>3</sub>-edge at 11919 eV. 8 samples were loaded at the same time on an automated sample holder and inserted into the closed-cycle He-cryostat (CryoVac). Se-K edge XANES and EXAFS spectra were collected in fluorescence mode at 15 K with an 18-element Ge-detector (Mirion) and a Falcon-X (XIA) electronic spectrometer. Each sample was scanned repeatedly for several times to obtain sufficient statistics. Energy correction and averaging of individual scans was performed in Sixpack (Webb, 2005). The averaged spectra were then processed in WinXAS (Ressler, 1998) using standard procedures. The spectra were normalized by 1<sup>st</sup> and 2<sup>nd</sup> order polynomial fits before and after the absorption edge, respectively. The energy threshold E<sub>0</sub> was determined by the first inflexion point of the absorption edge for conversion into k space, and the EXAFS spectrum was then extracted by using a cubic-spline fit from 2 to 13



$\text{\AA}^{-1}$  at  $k^3$  weight, using the AutoSpline functionality of WinXAS. Statistical analyses (principal component analysis, VARIMAX rotation, iterative target test transformations) were performed with the ITFA software package (Rossberg et al., 2003) for quantitative speciation using both XANES and  $k^3$ -weighted EXAFS spectra (note that only the latter data are reported, but both methods yielded similar results). EXAFS shell fitting was conducted in WinXAS in R space ( $k^3$  weight, Bessel window,  $k$  range 2-12  $\text{\AA}^{-1}$ ).

### 3.2.6 Mediated electrochemical reduction and oxidation

Mediated electrochemical reduction (MER) and oxidation (MEO) were performed at TNO, Utrecht, to measure redox-active Fe in the clay mineral samples and to derive their apparent Eh using the method described by Gorski et al. (Gorski et al., 2012a; Gorski et al., 2013). A three-electrode setup was used having a glassy carbon crucible working electrode, a 3 M NaCl Ag/AgCl reference electrode and a platinum counter electrode separated from the working electrode compartment by a porous glass frit (Hoving et al., 2017). All experiments were carried out in a pH 7 buffered solution (0.1 M NaCl, 0.01 M MOPS buffer,  $\text{pK}_a = 7.2$ ). The stability of the mediators at pH 5 could not be guaranteed, as there was a color change in the buffer solution after measurements. Consequently, the Eh of the clays was not measured at pH 5. A constant potential was applied on the electrochemical cell. Subsequently, an electron transfer mediator was added to facilitate electron transfer between the working electrode and Fe in the clay mineral. After equilibration of the mediator with the applied potential, the clay mineral suspension was added to the cell. The extent of structural Fe reduction or oxidation was determined by integrating the current peak response (electron accepting capacity (EAC) and electron donating capacity (EDC)). Redox profiles were constructed by measuring the EAC and EDC at a wide range of different applied potentials. To ensure proper electron transfer, mediators were used at applied potentials within  $\pm 0.12$  V of their  $E_h^0$  -values (Gorski et al., 2013). The following mediators were used: ABTS (2,2'-azino-bis(3-ethylbenzothiazoline-6-sulphonic acid), ferri/ferro-cyanide ( $\text{Fe}^{2+/3+}(\text{CN})_6$ ), DCPIP (2,6-dichlorophenolindophenol), hexaammineruthenium ( $\text{Ru}^{2+/3+}(\text{NH}_3)_6$ ), resorufin, riboflavin 5'-monophosphate, zwitterionic viologen (4,4' - bipyridinium-1,1' -bis(2-ethylsulfonate)), and triquat (1,1' -trimethylene-2,2' - bipyridyl). The resulting redox profiles of the various clay mineral samples were fitted using a modified form of the Nernst equation (Eq. 2 in Gorski et al., 2013). From these fitted curves the apparent reduction potential was derived.

3.3 Results and discussion

3.3.1 Clay characterization

In a previous study, we compared the morphology of the native and CBD-reduced Fe-bearing phyllosilicates and observed no significant change. Only a limited dissolution of the external layers from the clay platelets could be identified (Qian et al., 2023). To assess the potential impact of this slight external surface dissolution on the chemical properties of the different clays, we measured the CEC with Ni-en and Eu(III) sorption isotherms to compare the surface complexation on edge sites between the native and the reduced clays. The high selectivity of the Ni-en complex for the cation exchange sites, allows us to assess the CECs of the native and reduced clays (Table 3.2). No significant difference of CEC between native and reduced clays were observed, indicating that the cation exchange sites of reduced clays were not significantly affected by the reduction process.

Table 3.2. Clay characterization (Redox active and inactive Fe as measured by MEO/MER, CEC as determined by the Ni-en method).

Clay	Fe(II)/Fe <sub>tot</sub>	Fe(III) /Fe <sub>tot</sub>	Redox inactive Fe/Fe <sub>tot</sub>	Fe(II) wt%	Fe(II) mmol/kg <sub>clay</sub>	CEC meq/kg
High-red. N <sub>Au</sub> -2	0.58	0.12	0.30	11.4	2040	1125
Low-red. N <sub>Au</sub> -2	0.19	0.45	0.34	4.2	740	1137
Native N <sub>Au</sub> -2	0.00	0.75	0.25	0.0	0	1050
Red. S <sub>Wy</sub> -2	1.00	0.00	0.00	2.5	450	1247
Native S <sub>Wy</sub> -2	-*	-	-	0.0*	0	1239
Red. S <sub>Tx</sub> -1	0.89	0.00	0.11	0.6	100	1202
Native S <sub>Tx</sub> -1	-*	-	-	0.0*	0	1247

\*: The native S<sub>Wy</sub>-2 and S<sub>Tx</sub>-1 were not measured by MEO/MER. All the existing Fe in the native S<sub>Wy</sub>-2 and S<sub>Tx</sub>-1 is in Fe(III) state given by the Clay Minerals Society in Table 3.1.

Fig. 3.1 shows the sorption isotherms of trivalent Eu at around pH 7 for the different native and reduced clays. The Eu sorption was predicted using the 2 site protolysis non-electrostatic surface complexation and cation exchange (2SPNE SC/CE) model for montmorillonite (Baeyens and Marques Fernandes, 2018) and is shown as black line in Fig. 3.1. Note the nonlinear shape indicating adsorption to both strong and weak sorption sites.

Our sorption data for the different native and reduced clays agree well with this previously determined model for montmorillonite. Except for a slightly higher Eu sorption (~0.5 log units) on high-red. N Au-2, no significant variation in Eu sorption between native and reduced clays could be identified. The slightly higher Eu sorption on high-red. N Au-2 is likely due to the higher pH of this isotherm (7.3 compared to 7.0-7.1), since in 0.1 M NaCl the sorption of positively charged cations adsorbing via surface complexation raises sharply in the pH range 6-8 (Baeyens and Marques Fernandes, 2018; Jaisi et al., 2008b), hence our conclusion is that Fe reduction by the CBD method did not affect sorption to the edge sites of the clay.

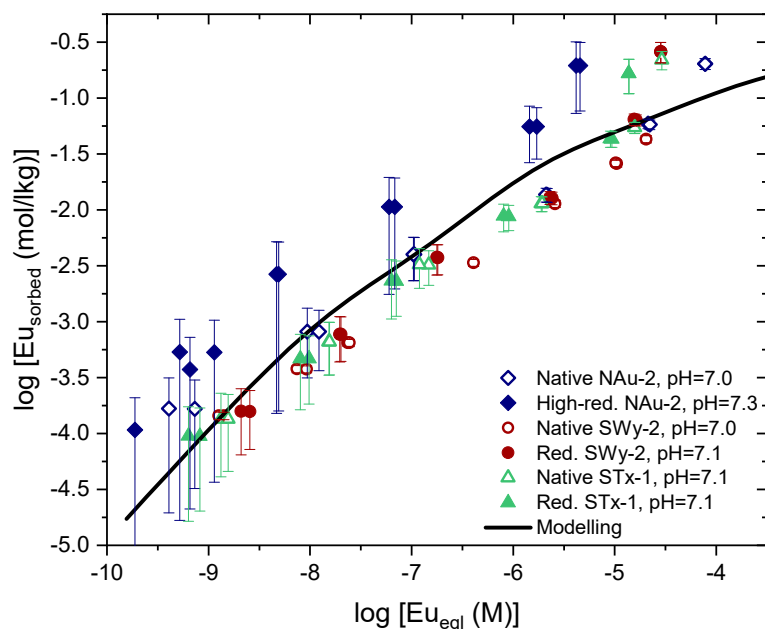


Fig. 3.1. Eu sorption isotherm on native and reduced N Au-2, SWy-2, and STx-1 in 0.1 M NaCl, S/L of 2 g/L, and pH 7. The modelling curve is based on parameters taken from (Baeyens and Marques Fernandes, 2018).

### 3.3.2 Sorption kinetics

Preliminary sorption studies (Fig. S3.1) showed that after 7 days, selenite uptake by reduced clays was comparable to that obtained for non-reduced clays (Missana et al., 2009). The sorption of selenite after 7 days (Fig. S3.1a) decreases as the pH increases from 4 to 8. Missana et al. modelled the data with a simple one-site model (complexes with only weak sites), assuming surface complexation  $\text{pH} < 8$  (Missana et al., 2009). Due to the repulsion of the selenite anion on the deprotonated clay surface, the sorption drops dramatically at  $\text{pH} > 8$ . Previous studies have shown, however, that the Se reduction is kinetically controlled (Charlet et al., 2007; Onoguchi et al., 2019; Pearce et al., 2008). Therefore, we investigated

sorption kinetics on reduced clays up to several months. For these kinetics experiments, we chose a pH of 5 (Fig. S3.1a) and an initial Se concentration of  $3 \times 10^{-5}$  M to obtain sufficient Se loadings (Fig. S3.1b) to be able to study their speciation with XAFS.

Fig. 3.2 shows the sorption kinetics of reduced clays from 4 hours to 3600 hours. The sorption results are listed in Table 3.3. The sorption of selenite on reduced clays increases with contact time, indicating a kinetically controlled uptake reaction, consistent with previous observations (Charlet et al., 2007; López de Arroyabe Loyo et al., 2008; Myneni et al., 1997). High-red. NAu-2 which has with 11.4 wt% the highest amount of Fe(II), shows also a significantly higher selenite uptake than the other reduced clays, achieving complete sorption of selenite achieved after 720 h. Red. SWy-2 exhibited lower sorption, which gradually increased over a period of 3600 h without reaching a plateau. Low-red. NAu-2 and red. STx-1 seem to show a similar behavior, although values of 1440 h, 2160 h, and 3600 h are not available due to contamination. Clearly, selenite sorption on reduced clays requires considerably long equilibration time, suggesting that Se(IV) might be gradually reduced after adsorption on the Fe(II)-bearing clays (Charlet et al., 2007). To further explore the evolution of selenite uptake, presumably by reduction, we followed the sorption kinetics with XAFS.

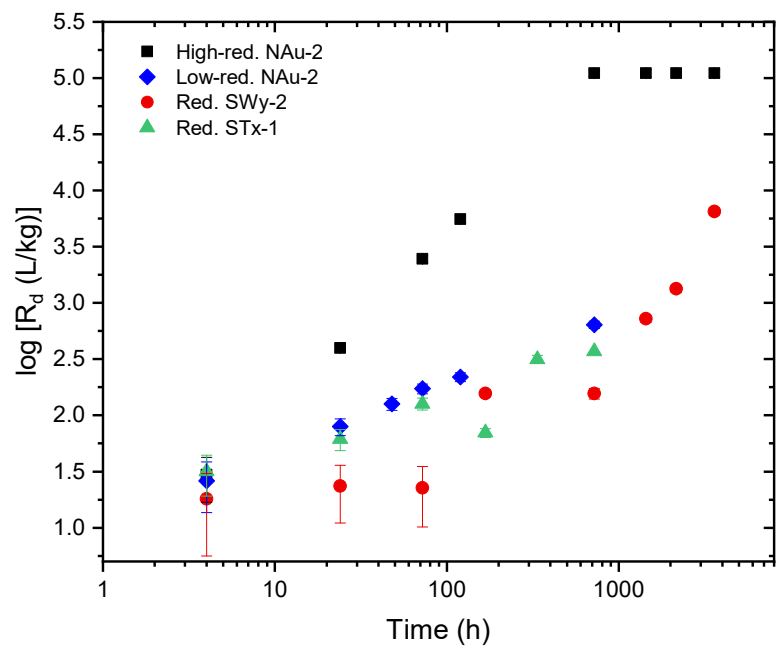


Fig. 3.2. Selenite sorption kinetics on reduced clay samples at S/L of 2 g/L,  $[\text{Se}]_{\text{init}} = 3 \times 10^{-5}$  M, pH=5, and 0.1 M NaCl. If error bars are not visible, they are smaller than symbol sizes.

### 3.3.3 Se K-edge XAFS measurements of kinetic clay samples

To follow the kinetics of Se oxidation state, we performed Se K-edge XANES spectroscopy. The temporal evolution of the four reduced clay samples is shown in Fig. 3.3-3.6 (a) along with selenite (Se(IV)), red Se(0) and grey Se(0) reference spectra. The Se(IV) reference is selenite sorbed to each respective native clay at pH 5, while red Se(0) and grey Se(0) reference are retrieved from previous publications (Charlet et al., 2007; Scheinost and Charlet, 2008; Scheinost et al., 2008). By looking at the two white line positions for Se(IV) and Se(0) (marked by hatched lines), the XANES spectra allow to directly follow the evolution of the oxidation state of selenium across time. Except for high-red. N<sub>Au</sub>-2, which is already largely reduced at this stage, the samples of the shortest reaction time (4 h) show the Se(IV) white line, which then gradually transform into Se(0) white lines.

While XANES alone would be sufficient to discriminate between Se at oxidation states 0 and IV, further details about the exact chemical structure of sorption complexes can be derived by analyzing the EXAFS spectra (see  $k^3$ -weighted EXAFS chi function in subfigures (b) of Fig. 3.3-3.6, and their corresponding Fourier Transform Magnitudes (FTM) in subfigures (c) of Fig. 3.3-3.6). The chi spectra of selenite are dominated by oscillations in the low  $k$ -range arising from backscattering of the Se-O pairs of the selenite molecule, whereas Se(0) spectra are dominated by oscillations in the high  $k$ -range arising from backscattering of the (nearest neighbor) Se-Se pairs of elemental selenium.

In the FTM spectra, the peak at approximately 1.3 Å (distance not corrected for phase shift) represents the Se(IV)-O interaction. Red and grey Se(0) can easily be distinguished since red Se(0) exhibits only one peak at around 2.0 Å (uncorrected for phase shift) representing the nearest Se-Se pairs, while grey Se(0) displays an additional peak at approximately 3.1 Å (uncorrected for phase shift) arising from next nearest Se-Se pairs and hence representing the longer range order of crystalline, grey elemental Se. In fact, all three FTM peaks occur in our set of clay samples with temporal evolution, indicating the presence of selenite and of red and grey elemental selenium.

To further elucidate the presence of different chemical species and to retrieve their statistical distribution among the different clay samples, we performed an in-depth analysis using ITFA (Rossberg et al., 2003). The number and identity of representative species in each kinetic clay series was based on principal component analysis, the Malinoswki indicator, and the visual inspection of the reconstruction (red lines) of the experimental spectra (black lines) (Fig. 3.3-3.6). More details of the procedure can be found e.g. in

Yalçıntaş et al. (Yalçıntaş et al., 2016a). Using only the spectra of the Se reacted clays in each series (i.e., without references), we identified either two or three spectral components (i.e., chemical species) depending on the clay types. About 20 potential reference spectra out of a database, including e.g. red Se(0), grey Se(0), ferroselite, FeSe, and polyselenide, were then added step by step to reconstruct the experimental spectra and assess their statistical contribution.

With one exception (spectrum 4 of red. STx-1), all spectra in each clay series were well reconstructed with sorbed selenite plus either one or two of the elemental Se references (Fig. 3.3-3.6). While red. STx-1 and low-red. NAu-2 required only the addition of red Se(0), red. SWy-2 and high-red. NAu-2 required also the addition of grey Se(0) to obtain a good reconstruction of chi and FTM spectra. Note that the presence of grey Se(0) can also be derived from XANES by a more articulated post-edge dip (at the position of the blue hatched line marking the Se(IV) peak). In none of the samples was the formation of FeSe or FeSe<sub>2</sub> observed.

While the XANES of spectrum 4 of red. STx-1 was accurately reconstructed, differences primarily arose in the chi function. In the k range of 2 to 6 Å<sup>-1</sup>, the oscillation pattern matched that of Se(IV) but with lower amplitude, whereas in the 6-12 Å<sup>-1</sup> range, the oscillation pattern closely resembled that of red Se(0). No other Se species components could be identified to match this spectrum, and the intensity of Se-O and Se-Se<sub>1</sub> peaks in the Fourier transformation magnitude (FTM) aligned well with the trend of Se reduction. Hence, the imperfect reconstruction of spectrum 4 may result from oscillation interference between two Se components.

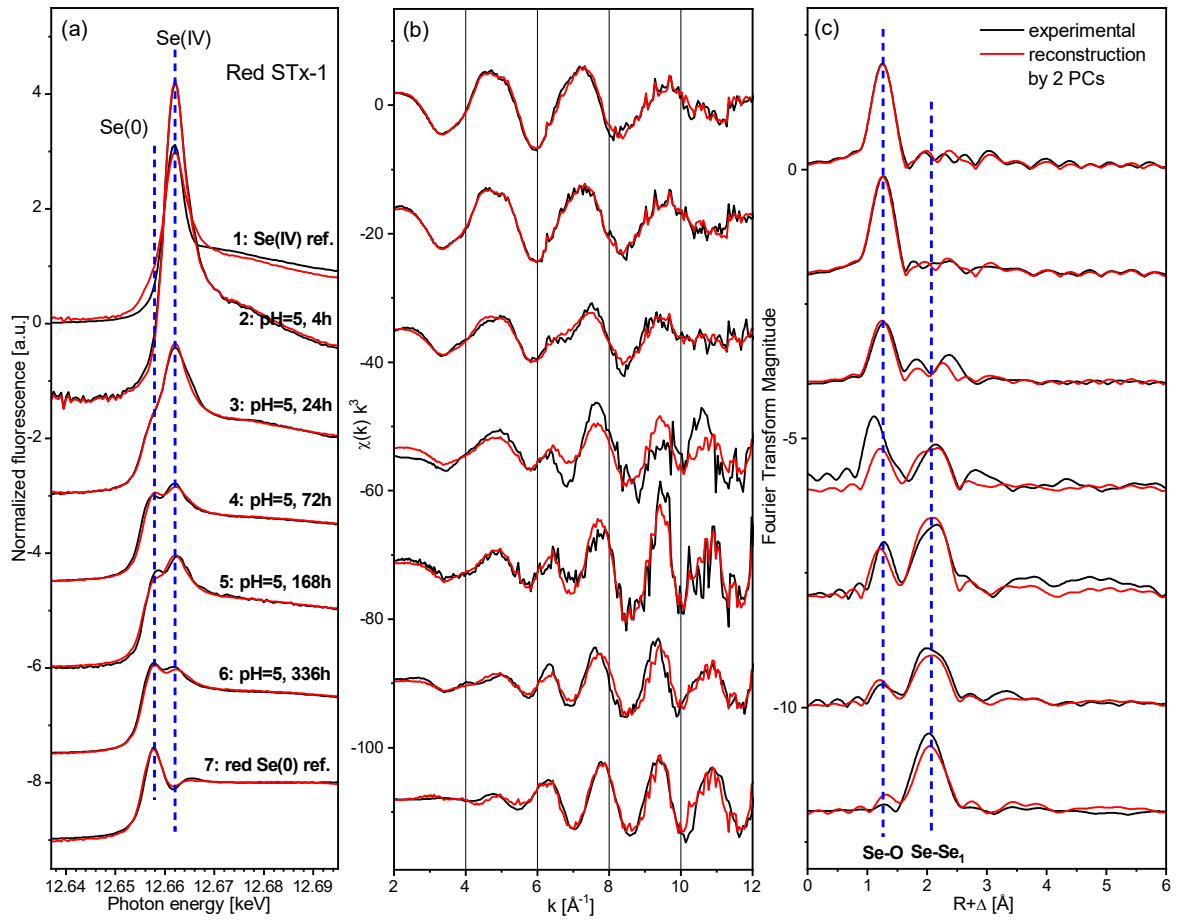


Fig. 3.3. Se K-edge XAFS of selenite sorption kinetics on red. STx-1 at S/L of 2 g/L,  $[\text{Se}]_{\text{init}} = 3 \times 10^{-5}$  M, 0.1 M NaCl, and pH 5. Samples were chosen from the kinetics experiments (Fig. 3.2) The black solid lines are the experimental data. The red solid lines represent the reconstruction of the spectra with two components: Se(IV) and red Se(0), and the blue dash line shows the position of each peak. (a) Normalized Se absorption edge (XANES), (b)  $k^3$ -weighted EXAFS chi function, (c)  $k^3$ -weighted EXAFS Fourier transform magnitude.

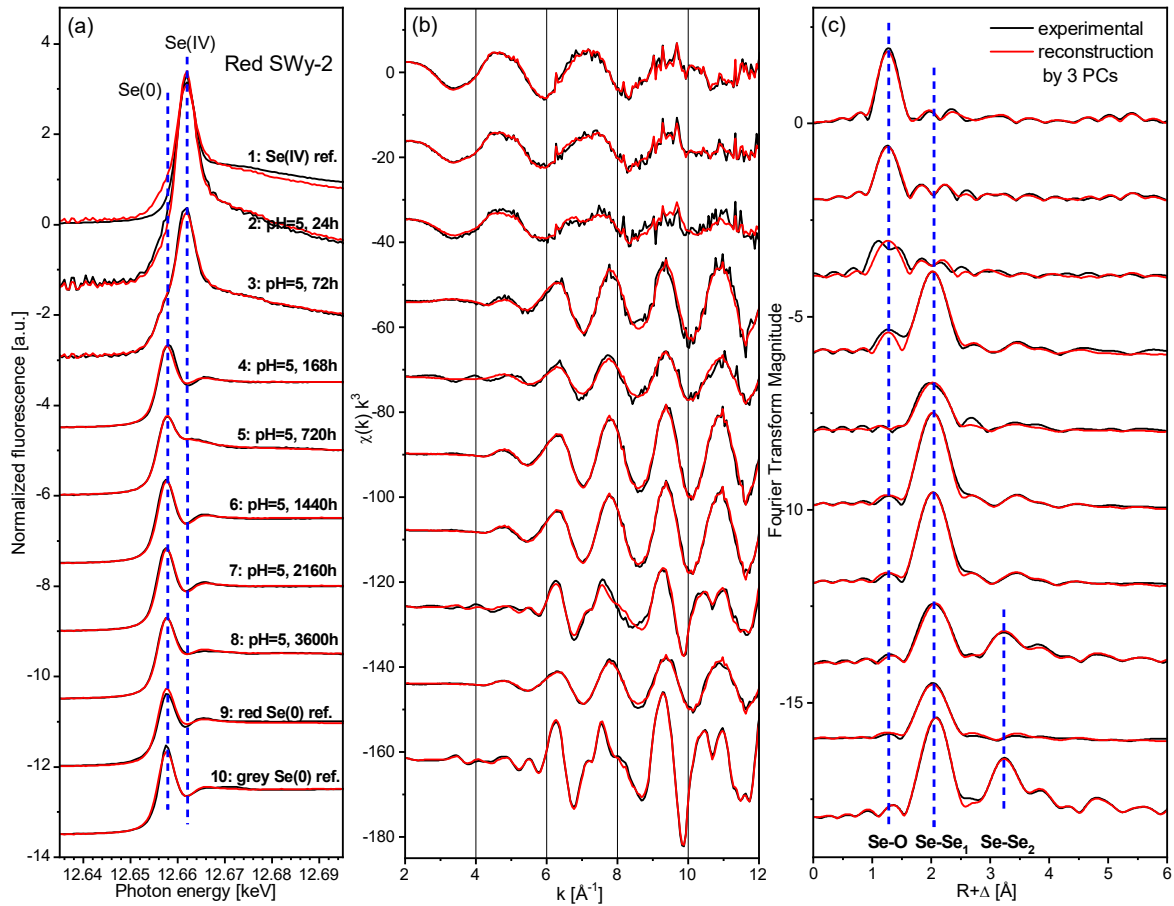


Fig. 3.4. Se K-edge XAFS of selenite sorption kinetics on red. SWy-2 at S/L of 2 g/L,  $[\text{Se}]_{\text{init}} = 3 \times 10^{-5}$  M, 0.1 M NaCl, and pH 5. Samples were chosen from the kinetics experiments (Fig. 3.2) The black solid lines are the experiment data. The red solid lines represent the reconstruction of the spectra with three components: Se(IV), red Se(0), and grey Se(0), and the blue dash line shows the position of each peak. (a) Normalized Se absorption edge (XANES), (b)  $k^3$ -weighted EXAFS chi function, (c)  $k^3$ -weighted EXAFS Fourier transform magnitude.



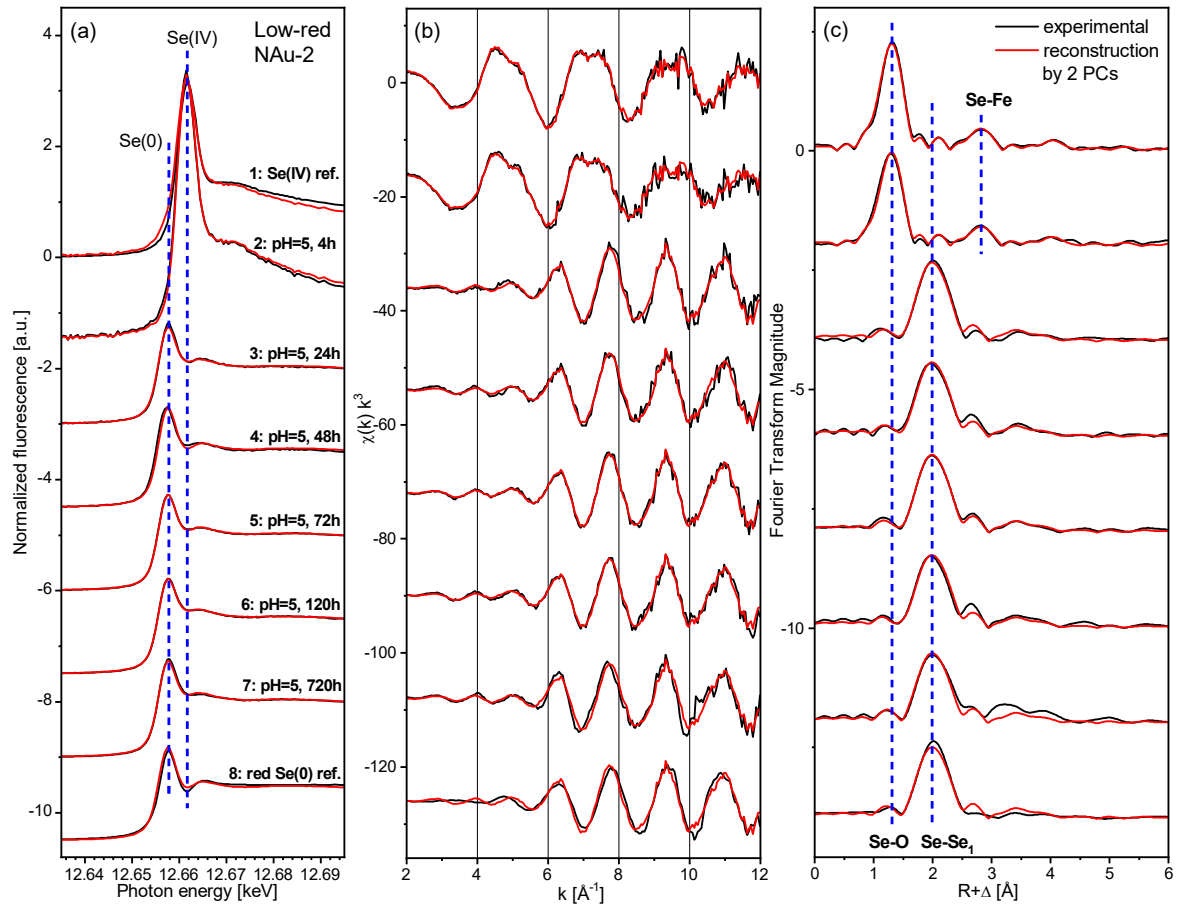


Fig. 3.5. Se K-edge XAFS of selenite sorption kinetics on low-red. NAu-2 at S/L of 2 g/L,  $[\text{Se}]_{\text{init}} = 3 \times 10^{-5}$  M, 0.1 M NaCl, and pH 5. Samples were chosen from the kinetics experiment (Fig. 3.2) The black solid lines are experiment data. The red solid lines represent the reconstruction of the spectra with two components: Se(IV) and red Se(0), and the blue dash line shows the position of each peak. (a) Normalized Se absorption edge (XANES), (b)  $k^3$ -weighted EXAFS chi function, (c)  $k^3$ -weighted EXAFS Fourier transform magnitude.

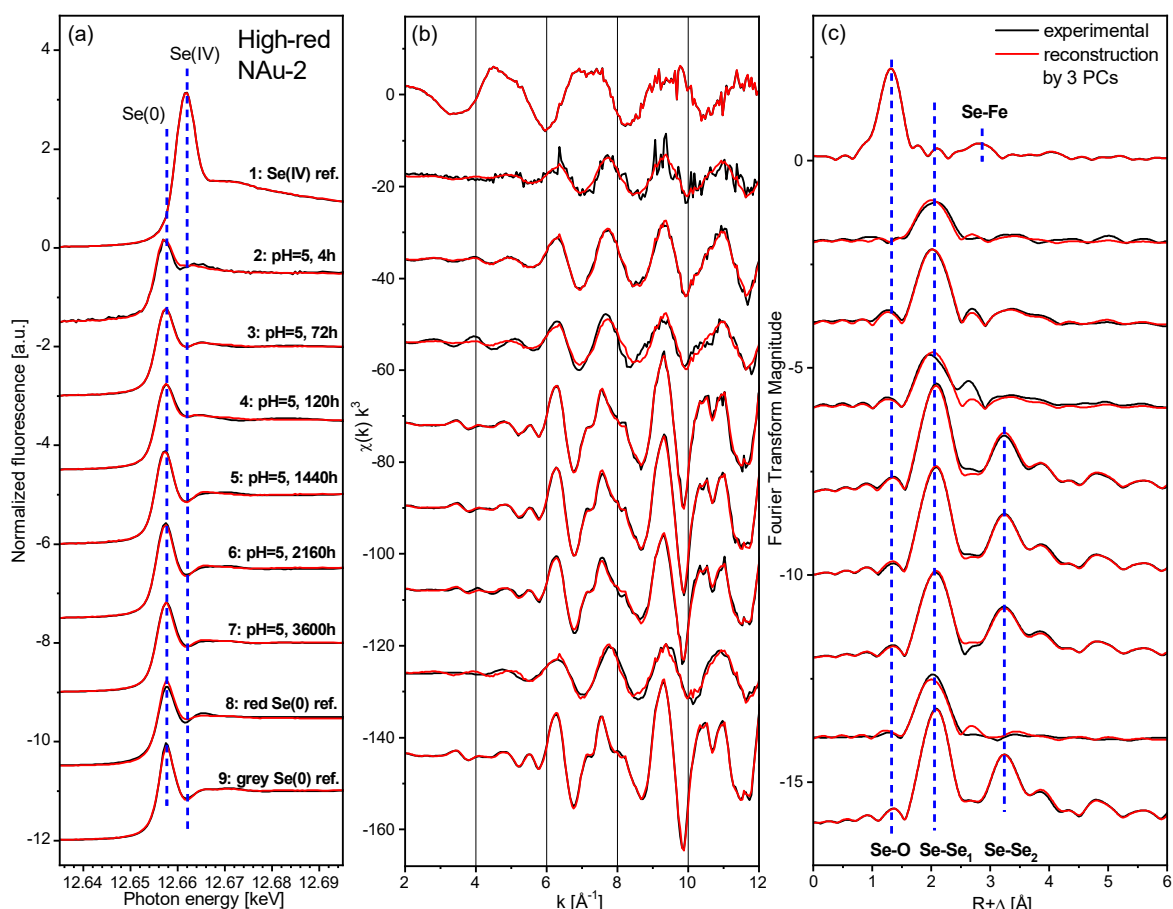


Fig. 3.6. Se K-edge XAFS of selenite sorption kinetics on high-red. NAu-2 at S/L of 2 g/L,  $[\text{Se}]_{\text{init}} = 3 \times 10^{-5} \text{ M}$ , 0.1 M NaCl, and pH 5. Samples were chosen from the kinetics experiment (Fig. 3.2) The black solid lines are the experiment data. The red solid lines represent the reconstruction of the spectra with three components: Se(IV), red Se(0), and grey Se(0), and the blue dash line shows the position of each peak. (a) Normalized Se absorption edge (XANES), (b)  $k^3$ -weighted EXAFS chi function, (c)  $k^3$ -weighted EXAFS Fourier transform magnitude.

### 3.3.4 Se reduction

The fraction of each component consisting of the EXAFS spectra was determined in all clay samples by iterative target test (ITT) (Rossberg et al., 2003) (Fig. 3.7). In red. STx-1, selenite gradually underwent reduction to red Se(0), without complete reduction or observation of grey Se(0) within the examined time range. Red. SWy-2 displayed a faster reduction of selenite compared to red. STx-1 and complete reduction was achieved. After 3600 h, red Se(0) was almost completely replaced by grey Se(0). In contrast to these clays with lower Fe content, selenite reduction was (almost) instantaneous by both reduced NAu-

2 samples, with the degree of Fe reduction influencing the final product. With low-red. NAu-2, only red Se(0) formed, while with high-red. NAu-2, red Se(0) was formed initially, but was then gradually replaced by grey Se(0). Based on the observed trends of reduction behavior, the reduction kinetics of selenite appear to be correlated to the Fe(II) content of the clays.

To further substantiate this observation, we plotted  $[\text{Se(IV)}]_t$  against time and fitted a linear regression between the initial Se(IV) fraction and the time when the lowest Se(IV) fraction was first obtained. The slope of this regression line can be considered as an apparent zero-order kinetics constant  $k$  of selenite reduction (Table 3.3). As already suggested by visual inspection, reduction kinetics exhibit a linear positive relationship ( $R^2=0.97$ ) with Fe(II) content in clay (Fig. 3.8). In addition to the selenite reduction rate, the time of grey Se(0) formation is probably also influenced by Fe(II) content. Comparing the formation of grey Se(0) in Fig. 3.7b and 3.7d, high-red. NAu-2 requires less time to form grey Se(0) than red. SWy-2. The correlation between Fe(II) content and grey Se(0) formation rate needs to be further studied with more Fe(II)-bearing clay samples and extended reaction time.

The decrease of red Se(0) and the increase of grey Se(0) at the same time indicated transformation of red Se(0) to grey Se(0). Red Se(0) is a metastable form of elemental selenium, existing as either an amorphous structure consisting of loosely stacked 8-rings, or a crystalline, monoclinic configuration of 8-rings, while grey Se(0) is the stable state of trigonal elemental selenium, characterized by spiral chains of Se atoms (Scheinost et al., 2008). Formation of red Se(0) resulting from selenite reduction has been observed in various minerals, including montmorillonite (Scheinost et al., 2008), siderite (Scheinost et al., 2008), green rust (Myneni et al., 1997), pyrite (Breynaert et al., 2008), and Fe(II)-sorbed calcite (Chakraborty et al., 2010). Grey Se(0) has been reported on magnetite (Poulain et al., 2022) and natural pyrite (Curti et al., 2013). Reaction conditions varied largely across these selenite reduction reactions, which makes it difficult to derive the factors determining formation of red or grey elemental Se. One notable observation is, however, that the presence of both elemental Se(0) species was noted on pyrite around pH 8 with red Se(0) forming after 3 weeks (Breynaert et al., 2008) and grey Se(0) forming after 8 months (Curti et al., 2013). This is in agreement with our study, where formation of red Se(0) required less time than that for grey Se(0) on the same clay mineral. And interesting question is the possible mechanism leading to the observed transformation of solid-state red Se to solid-state grey Se. Conventionally, the transformation of red Se(0) to grey Se(0) is achieved via

high-pressure heating (Minaev et al., 2005; Wiberg and Wiberg, 2001). However, in this experiment, conducted under ambient conditions, one of the key distinguishing factors is the Fe(II) content within the clays. Note that owing to its additional Se-Se bond and structural arrangement, crystalline grey Se(0) exhibits metallic conductivity (Greenwood and Earnshaw, 2012). It is hence plausible that a continuous electron transfer facilitates the sharing of electrons among adjacent atoms and thus prompts the formation of Se-Se bonds (Persch et al., 2021). High-red. NAu-2, possessing a higher concentration of Fe atoms within its structure, likely promotes faster electron transfer when compared to red. SWy-2 with lower structural Fe content. As for the three types of dioctahedral smectite clays in this study, Fe is predominantly located in the octahedral sheets (Van Olphen et al., 1979) (as opposed to tetrahedral sheets which are occupied mostly by Si or Al). In addition to Fe(II) content, the Fe distribution in the octahedral sheet may be also an important factor to the final reduced species. According to Vantelon et al., SWy-2 displays an ordered distribution of Fe in the octahedral sheet, while STx-1 displays extensive Fe clustering (Vantelon et al., 2003). Hence, despite STx-1 having a low Fe(II) content of 0.6 wt%, electron transfer remains feasible for selenite reduction possibly due to this Fe clustering. Nonetheless, the precise impact of electron transfer kinetics and Fe(II) quantity on the structural transformation between red and grey Se(0) species remains elusive. To address this, future studies could employ clays with the same structure but varying reduction levels over extended reaction times.

In addition to elemental Se(0) being the prevalent reduced species, several investigations have documented formation of FeSe precipitates during selenite sorption onto mackinawite, magnetite, green rust, pyrite, zerovalent iron, and iron hydroxides (Börsig et al., 2018; Breynaert et al., 2008; Diener et al., 2012; López de Arroyabe Loyo et al., 2008; Olegario et al., 2010; Scheinost and Charlet, 2008; Scheinost et al., 2008). All these investigations highlighted the correlation between iron selenide formation and selenite reduction kinetics and presence of  $\text{Fe}^{2+}$  ( $2.8 \sim 77 \times 10^{-3} \text{ M}$  in equilibrium). Fast selenite reduction kinetics in the presence of  $\text{Fe}^{2+}$  fosters the formation of FeSe; observation of FeSe within 30 minutes up to several hours was reported in the literature. Moreover, reduction kinetics are directly associated with the size and surface condition of the iron minerals. Nanominerals (2 - 50 nm) possess a high specific surface area, which enhances reduction kinetics. In addition, the iron sulfide mackinawite FeS contains not only Fe(II) but also S(-II) in the system, acting as electron donor to reduce Se(IV). However, in our study, no FeSe

or FeSe<sub>2</sub> was observed, and a slower reduction kinetics was observed, spanning from days to months. In contrast to the literature reported equilibrium Fe<sup>2+</sup> concentration of 10<sup>-3</sup> M, the results of this study reveal that the concentration of Fe<sup>2+</sup> in the supernatant of the sorption experiment at both pH 5 and 7 (Table 3.3) is several orders of magnitude lower. Additionally, the initial selenite concentration of 10<sup>-2</sup> - 10<sup>-4</sup> M is higher than the 3×10<sup>-5</sup> M used in this study. Moreover, compared to the nanomaterials (2 - 50 nm) mentioned in these references, the clay minerals investigated here possess larger particle sizes (< 500 nm), potentially leading to slower reduction kinetics. Notably, the surface conditions of reduced clays displayed minimal alteration in terms of the cation exchange capacity (Table 3.2) and the availability of surface complexation edge sites (Fig. 3.1) when compared to native clays. Consequently, we observed exclusively elemental Se(0) as the selenite reduced species.

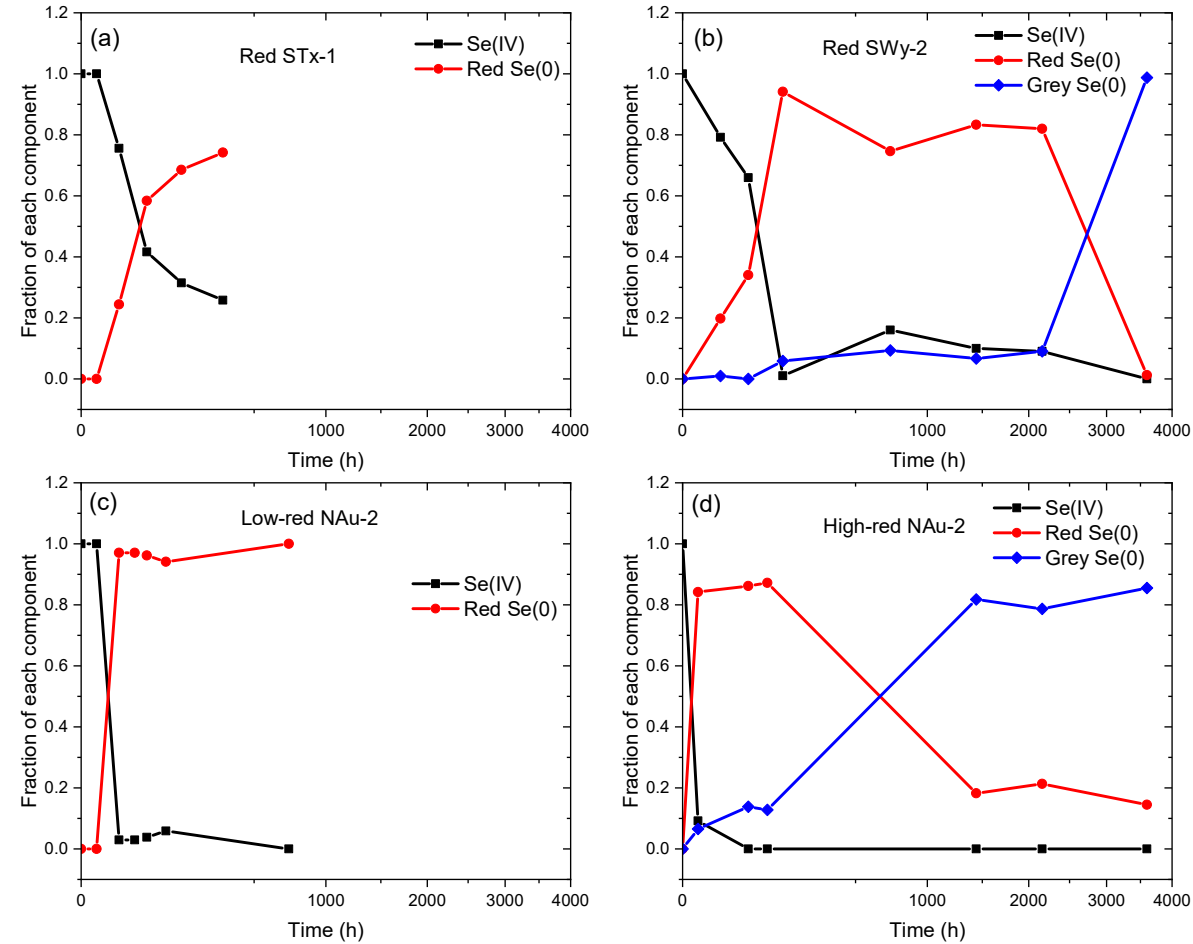


Fig. 3.7. Fraction of selenite Se(IV) (black square lines), red Se(0) (red dot lines), and grey Se(0) (blue diamond lines) for each kinetics experiment with reduced clays (red. STx-1, red. SWy-2, low-red. NAu-2, and high-red. NAu-2) at different reaction time. X-axis is in square root scale. Fractions are derived from the chi spectra in Fig. 3.3-3.6 by ITT.

Table 3.3. Kinetics of selenite sorption and reduction; fraction of reduced species resulted from ITT.

pH	Time hour	log Rd mL/g	Se loading mmol/kg	Se(IV) fraction	red Se(0) fraction	grey Se(0) fraction
<b>Red. STx-1 (Fe(II)<sub>str</sub>: 100 mmol/kg, [Fe<sup>2+</sup><sub>eq</sub>] ≈ 2×10<sup>-5</sup> M, k* = 0.00215 h<sup>-1</sup> at pH 5)</b>						
5	4	1.50	0.74	1.00	0.00	0.00
5	24	1.79	1.37	0.76	0.24	0.00
5	72	2.10	2.52	0.42	0.58	0.00
5	168	1.85	1.49	0.32	0.68	0.00
5	336	2.50	4.82	0.26	0.74	0.00
5	720	2.57	5.31	- <sup>‡</sup>	-	-
<b>[Fe<sup>2+</sup><sub>eq</sub>] ≈ 1×10<sup>-6</sup> M at pH 7</b>						
7	168	1.94	1.84	0.79	0.21	0.00
7	1440	2.79	6.84	0.11	0.77	0.12
<b>Red. SWy-2 (Fe(II)<sub>str</sub>: 450 mmol/kg, [Fe<sup>2+</sup><sub>eq</sub>] ≈ 1×10<sup>-5</sup> M, k* = 0.00576 h<sup>-1</sup> at pH 5)</b>						
5	4	1.26	0.44	- <sup>‡</sup>	-	-
5	24	1.37	0.56	0.79	0.20	0.01
5	72	1.35	0.54	0.66	0.34	0.00
5	168	2.12	2.78	0.00	0.94	0.06
5	720	2.19	2.97	0.16	0.75	0.09
5	1440	2.86	7.34	0.10	0.83	0.07
5	2160	3.13	9.02	0.09	0.82	0.09
5	3600	3.81	11.47	0.00	0.01	0.99
<b>[Fe<sup>2+</sup><sub>eq</sub>] ≈ 3×10<sup>-6</sup> M at pH 7</b>						
7	168	1.58	0.86	0.58	0.36	0.06
7	1440	2.64	5.77	0.05	0.26	0.68
<b>Low-red. NAu-2 (Fe(II)<sub>str</sub>: 740 mmol/kg, [Fe<sup>2+</sup><sub>eq</sub>] ≈ 5×10<sup>-5</sup> M, k* = 0.04306 h<sup>-1</sup> at pH 5)</b>						
5	4	1.42	0.62	1.00	0.00	0.00
5	24	1.90	1.71	0.03	0.97	0.00
5	48	2.10	2.51	0.03	0.97	0.00
5	72	2.24	3.19	0.04	0.96	0.00
5	120	2.34	3.79	0.06	0.94	0.00
5	720	2.81	6.95	0.00	1.00	0.00
<b>High-red. NAu-2 (Fe(II)<sub>str</sub>: 2040 mmol/kg, [Fe<sup>2+</sup><sub>eq</sub>] ≈ 6×10<sup>-4</sup> M, k* = 0.22679 h<sup>-1</sup> at pH 5)</b>						
5	4	1.47	0.70	0.09	0.84	0.07
5	24	2.60	5.53	- <sup>‡</sup>	-	-
5	72	3.39	10.41	0.00	0.86	0.14
5	120	3.75	11.49	0.00	0.87	0.13
5	720	5.04	12.46	- <sup>‡</sup>	-	-
5	1440	5.04	12.46	0.00	0.18	0.82
5	2160	5.04	12.46	0.00	0.21	0.79
5	3600	5.04	12.46	0.00	0.14	0.86
<b>[Fe<sup>2+</sup><sub>eq</sub>] ≈ 3×10<sup>-6</sup> M at pH 7</b>						
7	168	2.16	2.62	0.95	0.05	0.00
7	1440	5.04	12.46	0.00	0.21	0.79

\*: k represents the magnitude of the slope obtained from the linear regression of the Se(IV) fraction between the initial point and the time when the lowest Se(IV) fraction is first attained in Fig. 3.7.  
 ‡: Kinetic samples in Fig. 3.2 were not measured by XAFS due to limited beamtime and thus not displayed in Fig. 3.3-3.6.

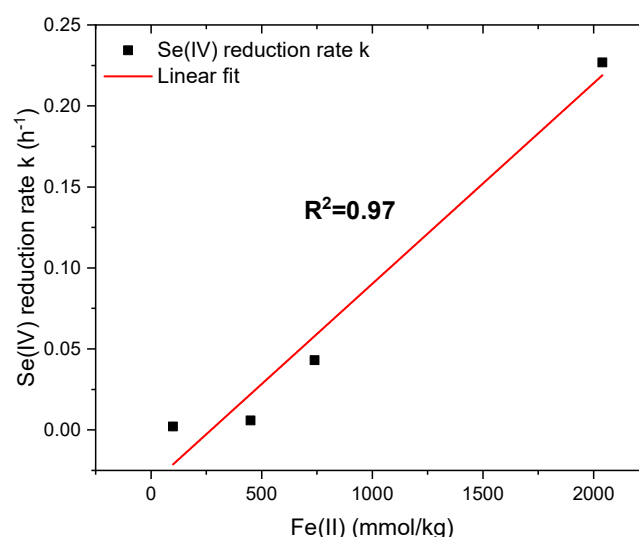


Fig. 3.8. Correlation between Fe(II) content in the clay and Se(IV) reduction rate  $k$  (Table 3.3)

### 3.3.5 Structure of the initial selenite sorption complex

Since previous research has demonstrated that formation of a covalent bond between adsorbed selenite and the clay edges is a prerequisite for its subsequent reduction (Charlet et al., 2007), the structure of this intermediate sorption complex in our samples is of substantial interest. Spectra 1 and 2 (Fig. 3.5), corresponding to adsorbed selenite, exhibit an additional peak at  $2.8 \text{ \AA}$  (uncorrected for phase shift), which could point to backscattering from a clay surface atom and hence towards formation of an inner-sphere sorption complex. Fig. 3.9a compares the spectra of adsorbed selenite on native STx-1, SWy-2, and NAu-2. Only NAu-2 displays a clear peak at  $2.8 \text{ \AA}$  (uncorrected for phase shift), while the peak is less evident in STx-1 and SWy-2. The Fourier backtransform of this peak shown in Fig. 3.9b has an envelope maximum at about  $8 \text{ \AA}^{-1}$  in line with backscattering from Fe, while the maximum for Al would be about  $2 \text{ \AA}^{-1}$  lower. This was confirmed by a successful shell fit, resulting in 2.7 O atoms at  $1.69 \text{ \AA}$  in line with the typical local coordination of selenite (Scheinost et al., 2008), and 1.4 Fe atoms at  $3.24 \text{ \AA}$  indicative for the inner-sphere sorption complex (Table 3.4). Previous studies (Börsig et al., 2021; Jordan et al., 2014; Manceau and Charlet, 1994) have reported two Se-Fe distances at  $2.9 \text{ \AA}$  and  $3.4 \text{ \AA}$  on magnetite, maghemite, and hydrous ferric oxide, corresponding to bidentate mononuclear edge-sharing (ES) and bidentate binuclear corner-sharing (CS) inner-sphere surface complexes, respectively. In our study, the Se-Fe peak does not show splitting, but rather exhibits a mean bond length of  $3.24 \text{ \AA}$ , roughly in between the distances of  $2.9$  and  $3.4 \text{ \AA}$  expected for ES and CS structures, thus probably pointing to a mixture of both ES and CS inner-sphere

complexes at Fe-occupied octahedra of clay edges. As for selenite sorption on montmorillonite, Peak et al. demonstrated bidentate binuclear inner-sphere complexation with Se-Al distances at 3.16 Å (Peak et al., 2006), while others only fitted with Se-O shell (Charlet et al., 2007; Scheinost et al., 2008). The Se-Al distances fitted for the two clays with lower Fe content (Table 3.4) are at 3.11 and 3.18 Å, which aligns with the fitting results of Peak et al. (Peak et al., 2006), and their CN of 1.2 and 0.8 point to the prevalence of ES inner-sphere sorption complexes with Al-occupied octahedra. The spectroscopy results corroborate the modelling of the Se sorption data with a surface complexation reaction by Missana et al. (2009). In addition, Zhang et al. have proposed a two-step selenite adsorption mechanism on goethite involving the initial formation of outer-sphere surface complexes followed by a ligand-exchange process to form inner-sphere surface complexes (Zhang and Sparks, 1990).

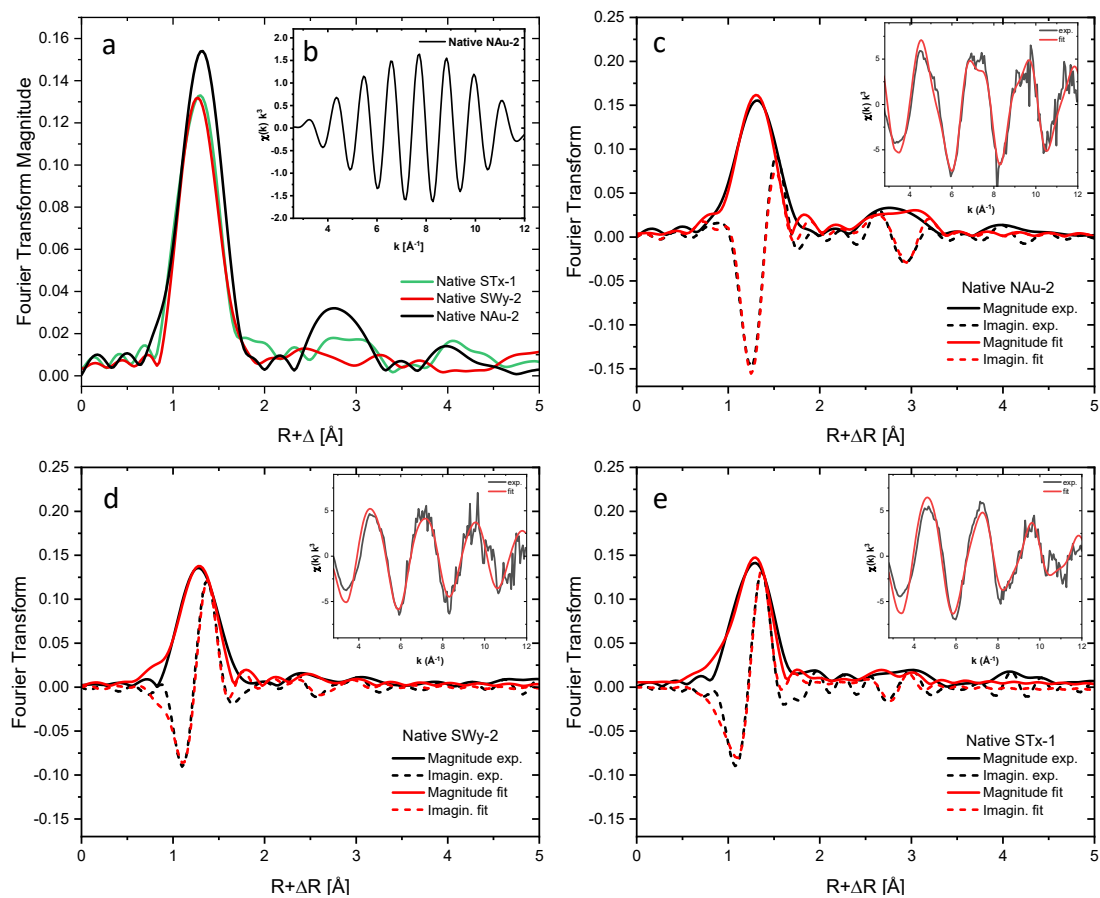


Fig. 3.9. (a) Comparison of Fourier transformation magnitude of Se(IV) sorption on native STx-1, SWy-2, and NAu-2. (b) Backscattered Fourier transformation of the second peak (R: 2.3 – 3.3 Å) of native NAu-2. (c)-(e) Shell fitting of native NAu-2, SWy-2, and STx-1 in  $R$  space; the fitted spectra in  $k$  space are inserted.



Table 3.4. Se K-edge shell fitting results for selenite sorption complexes.

Sample	Shell	CN <sup>a</sup>	R [Å] <sup>b</sup>	σ <sup>2</sup> [Å <sup>2</sup> ] <sup>c</sup>	ΔE <sub>0</sub> [eV]	S <sub>0</sub> <sup>2</sup>	χ <sub>Res</sub>
Native	Se-O	3.6	1.69	0.0054	13.7	0.9*	17.9
STx-1	Se-Al	0.8	3.18	0.0015			
Native	Se-O	2.6	1.69	0.0024	13.4	0.9*	15.5
SWy-2	Se-Al	1.2	3.11	0.0077			
Native	Se-O	2.7	1.69	0.0011	13.3	0.9*	17.2
NAu-2	Se-Fe	1.4	3.24	0.0046			

a: Error of coordination number (CN) ± 25%

b: Error of radial distance (R) ± 0.01 Å

c: Error of Debye-Waller factor (σ<sup>2</sup>) ± 0.002 Å

\*: S<sub>0</sub><sup>2</sup> fixed to 0.9

3.3.6 Redox potential of clays

Here we show the results of selected Se reduction kinetics performed at pH 7, with the aim to separate the influence of redox potential from that of pH, as the redox potential for selenite reduction decreases as pH increases. The redox potential plays a crucial role in determining whether a redox reaction can occur (Masscheleyn et al., 1990). The Eh-pH diagram of Se (Fig. 3.10) illustrates the Se species distribution as a function of Eh and pH. The kinetics of selenite sorption at pH 7 are depicted in Fig. 3.11. After one week, selenite shows no reduction on red. STx-1, partial reduction on red. SWy-2, and no reduction on high-red. NAu-2. The unexpected non-reduction of selenite observed in high-red. NAu-2 after 7 days is intriguing, as it reduces selenite and forms gray Se(0) at the fastest rate at pH 5 and is anticipated to show a similar redox behavior at pH 7. As the reaction time extends to 1440 h, selenite is reduced to red Se(0) on red. STx-1, transformed to grey Se(0) on red. SWy-2, and also converted to grey Se(0) on high-red. NAu-2. This indicates that selenite can still undergo reduction at pH 7, albeit at a much slower rate.

One notable difference is the amount of selenite sorption, which is generally lower at pH 7 compared to pH 5 (Table 3.3). However, despite displaying a lower sorption amount at pH 5 (0.70 mmol/kg, 4 h) compared to pH 7 (2.62 mmol/kg, 168 h), high-red. NAu-2 still exhibits complete reduction at pH 5 and zero reduction at pH 7. Therefore, the selenite sorption amount does not appear to be the primary factor driving the unexpected selenite reduction behavior of high-red. NAu-2. The variation in the selenite reduction behavior at different pH can be attributed to the disparity in the reducing potential required for selenite to be reduced to Se(0) (Fig. 3.10). Specifically, at pH 7, a lower reducing potential is necessary for the reduction of selenite to Se(0) as compared to pH 5.

The redox potential of the reduced clays was determined by MEO/MER measurements (Fig. 3.12). By applying the degree of reduction for each clay, the redox potential associated with the clay can be inferred from the redox profile (Gorski et al., 2013). Both red. STx-1 ( $\text{Fe(II)/Fe}_{\text{tot}}$ : 0.89) and red. SWy-2 ( $\text{Fe(II)/Fe}_{\text{tot}}$ : 1.0) exhibit a redox potential of approximately -0.4 V, while both low-red. ( $\text{Fe(II)/Fe}_{\text{tot}}$ : 0.19) and high-red. NAu-2 ( $\text{Fe(II)/Fe}_{\text{tot}}$ : 0.58) have with about +0.05 V a significantly higher redox potential (Fig. 3.10). The redox potentials of our reduced clays are similar to those reported by Gorski et al. (Gorski et al., 2013). The redox potential of reduced NAu-2 is higher than that of red. STx-1 and red. SWy-2. Hence, we suspect that selenite adsorbed on high-red. NAu-2 was not reduced after one week due to the small potential difference between clay and selenite, whereas red. SWy-2 exhibited easier initiation of selenite reduction owing to the larger potential difference. However, as the contact time increased, with sufficient electron transfer occurring from Fe(II) in high-red. NAu-2 to the adsorbed selenite, selenite was eventually reduced. In the case of red. STx-1, despite the redox potential being sufficient to initiate selenite reduction, selenite remained unreduced after one week. This could be attributed to the relatively low Fe(II) content in red. STx-1, which hinders efficient electron transfer within a short period for selenite reduction. Nevertheless, with sufficient contact time, selenite can still undergo reduction. At pH 5, the potential required to reduce selenite is higher compared to that at pH 7. Therefore, it is likely that the redox potentials of the four reduced clays are sufficient to initiate selenite reduction, indicating that it is not a limiting factor for this process. Note that the Eh-pH diagram illustrates the Se aqueous species in equilibrium, while the Eh measured by MEO/MER represents the initial redox potential of the clay and can be used to assess the progress of a redox reaction. Consequently, the overall reduction process is influenced not only by the redox potential of the clays, which initiates the redox reaction, but also by the experimental condition like pH. Gorski et al. observed that all smectites exhibited unique  $\text{Fe(II)/Fe}_{\text{tot}} - \text{Eh}$  relationship, which correlated with structural properties of clays (Gorski et al., 2013). However, it is not yet clear how these properties affect the redox potential of clays, but they may manifest in the redox reaction under different experimental conditions and need further study.

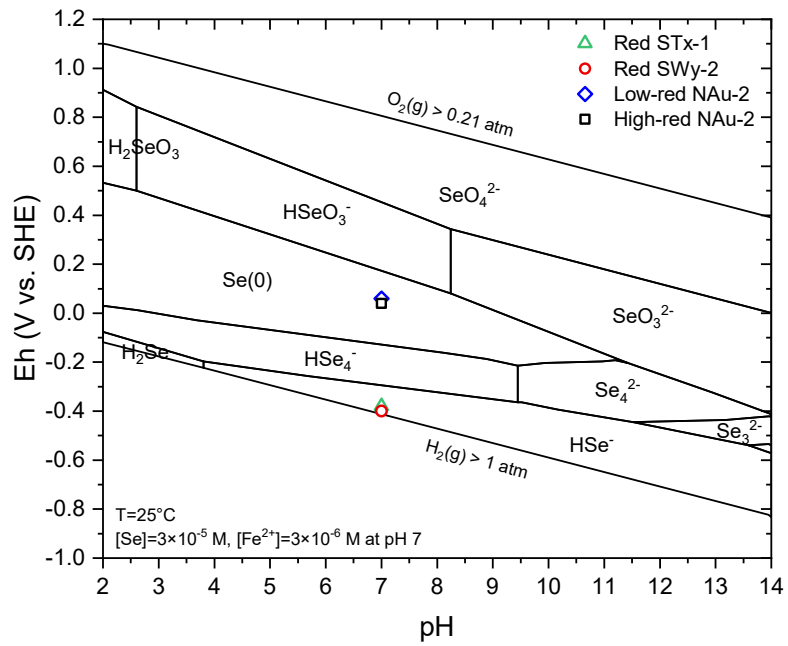


Fig. 3.10. Eh-pH diagram of Se-O-H system at 25°C,  $[\text{Se}]=3\times 10^{-5}\text{ M}$ , and  $[\text{Fe}^{2+}]=3\times 10^{-6}\text{ M}$  ( $[\text{Fe}^{2+}]$  is  $\text{Fe}^{2+}_{\text{eq}}$  determined in sorption experiments at pH 7), plotted by PhreePlot using the PSI Chemical Thermodynamic Database 2020 (W. Hummel, 2023). The redox potentials of reduced clays measured by MEO & MER at pH 7 are also shown (green triangle: red. STx-1, red circle: red. SWy-2, blue diamond: low-red. NAu-2, black square: high-red. NAu-2).

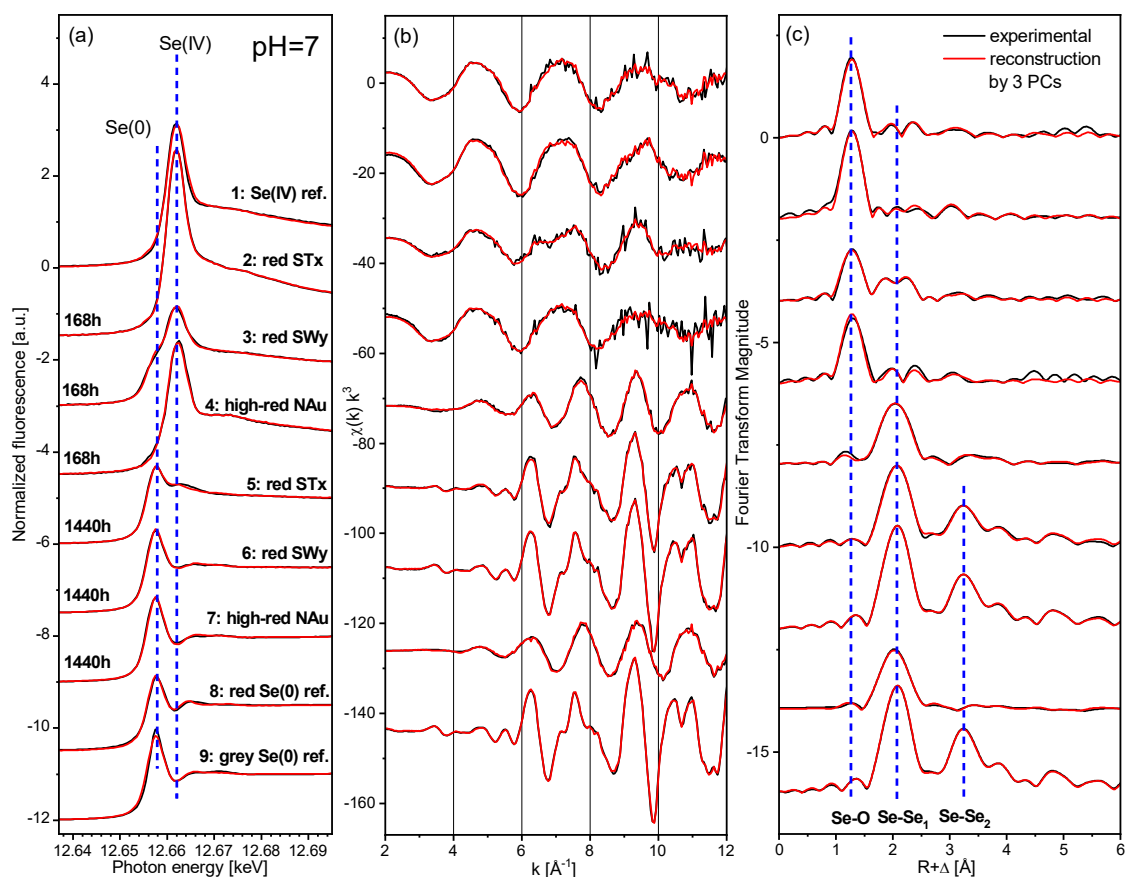


Fig. 3.11. Se K-edge EXAFS of selenite sorption kinetics on red. STx-1, red. SWy-2, and high-red. NAu-2 at S/L of 2 g/L,  $[\text{Se}]_{\text{init}} = 3 \times 10^{-5} \text{ M}$ , 0.1 M NaCl, and pH 7. The kinetics experiment results of the samples were listed in Table 3.3. The experiment data is in black solid line, the red solid line represents the reconstruction of the spectra with three components: Se(IV), red Se(0), and grey Se(0), and the blue dash line shows the position of each peak. (a) Normalized Se absorption edge (XANES), (b)  $k^3$ -weighted EXAFS chi function, (c)  $k^3$ -weighted EXAFS Fourier transform magnitude.

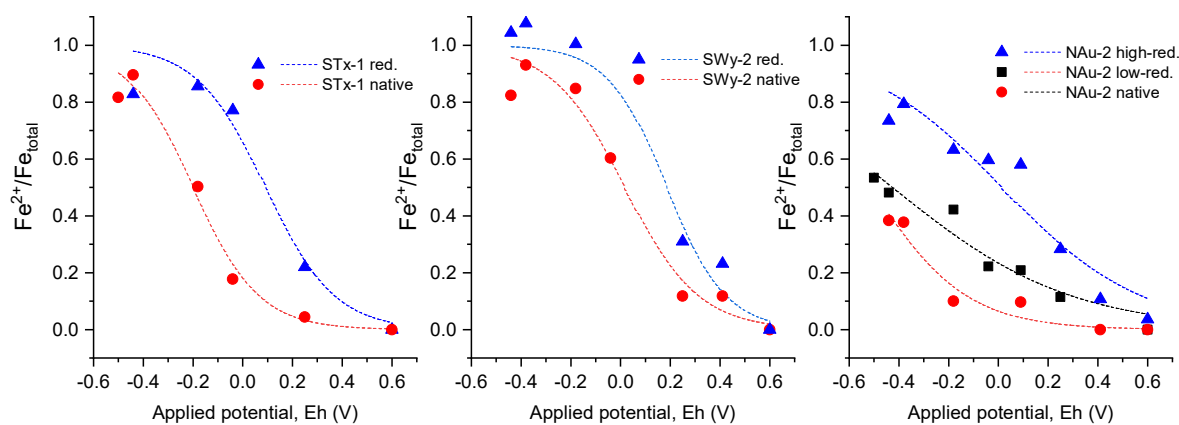


Fig. 3.12. Redox profiles of native and reduced STx-1, SWy-2, and NAu-2 measured by MEO & MER at pH 7.

### 3.4 Conclusion

We systematically investigated the kinetics of selenite adsorption and reduction across four reduced clay minerals, characterized by Fe(II) and Fe(III) contents and associated redox potentials, under different pH conditions. We observed adsorption and reductive precipitation in selenite sorption mechanism. Selenite reduction occurred on all the reduced clays, initially forming amorphous or nanoparticle red Se(0) which gradually transformed into thermodynamically more stable crystalline grey Se(0). No FeSe or FeSe<sub>2</sub> was detected under an initial selenite concentration of  $3 \times 10^{-5}$  M and equilibrium Fe<sup>2+</sup> concentration of up to  $6 \times 10^{-4}$  M at pH 5 within 3600 h. Selenite reduction rate is proportional to the structural Fe(II) content in the clay minerals at pH 5. At pH 7, selenite reduction still took place, albeit at a slower rate compared to pH 5, attributed to a narrower potential difference between clays and selenite. Under current experiment conditions, the determining factor of selenite reduction is the structural Fe(II) content at pH 5, while it is redox potential of clays at pH 7. Overall, the selenite reduction behavior is controlled by different factors, including redox potential of the clays, electron transfer at the interface (e.g., inner-sphere or outer-sphere surface complex), and experimental conditions (e.g. pH, [Se(IV)], time). The redox potential of the clay is related to the total Fe content, redox active Fe, Fe(II)/Fe(III) ratio, and Fe distribution within the structure. Future research should concentrate on one specific clay with varying reduction levels to investigate individual parameters more closely. Furthermore, employing a higher selenite solution concentration can help ascertain whether [Se(IV)] plays a decisive role in the formation of FeSe or FeSe<sub>2</sub>.

The reduced species elemental Se(0) is largely insoluble in water, with the solubility of crystalline grey Se(0) with larger particle size being several orders of magnitude lower than that of amorphous or nanoparticle red Se(0) (Gurunath et al., 2013). Since we observed a trend towards the formation of grey Se with longer reaction time, our findings strongly support the potential immobilization of selenite in selenium contaminated natural environments, where natural sources or anthropogenic activities contribute to elevated selenite concentrations, thereby safeguarding the surrounding ecosystems. Furthermore, in the context of radioactive waste disposal scenarios, the release and migration of long-lived and highly toxic <sup>79</sup>Se after canister corrosion poses significant risks to the biosphere. By immobilizing selenite, we can retard its migration, minimize the potential impact on ecosystems, and ensure the long-term safety of waste disposal facilities. Additionally, the utilization of clay minerals as sorbents in our selenite immobilization experiments enhances

the reliability and applicability of laboratory findings when extrapolating to real-world terrestrial environments and deep geological repositories, where clay minerals play a crucial role. Overall, these results of selenite immobilization are highly relevant in the context of environmental risk assessment associated with its bioavailability. It has implications for ecosystem protection, human health, and the safe management of radioactive waste, highlighting the importance of understanding and implementing effective strategies for selenite immobilization.

## **Acknowledgement**

This work was supported by European Union's Horizon 2020 research and innovation program under grant agreement No 847593. Beamtime at the Rossendorf Beamline at ESRF was provided by ESRF and HZDR. We thank Astrid Schaible and Andreas Laube for laboratory technical support, Dr. Bin Ma for insightful discussions on the results, and Jörg Exner for assisting with EXAFS measurements.

### 3.5 Reference

- Baeyens B. and Bradbury M. H. (2004) Cation exchange capacity measurements on illite using the sodium and cesium isotope dilution technique: Effects of the index cation, electrolyte concentration and competition: Modeling. *Clays and Clay Minerals* **52**, 421-431.
- Baeyens B. and Marques Fernandes M. (2018) 5 - Adsorption of heavy metals including radionuclides. In *Developments in Clay Science* (eds. R. Schoonheydt, C. T. Johnston and F. Bergaya). Elsevier. pp. 125-172.
- Bingham P. A., Connelly A. J., Cassingham N. J. and Hyatt N. C. (2011) Oxidation state and local environment of selenium in alkali borosilicate glasses for radioactive waste immobilisation. *Journal of Non-Crystalline Solids* **357**, 2726-2734.
- Börsig N., Scheinost A. C., Schild D. and Neumann T. (2021) Mechanisms of selenium removal by partially oxidized magnetite nanoparticles for wastewater remediation. *Applied Geochemistry* **132**, 105062.
- Börsig N., Scheinost A. C., Shaw S., Schild D. and Neumann T. (2017) Uptake mechanisms of selenium oxyanions during the ferrihydrite-hematite recrystallization. *Geochimica et Cosmochimica Acta* **206**, 236-253.
- Börsig N., Scheinost A. C., Shaw S., Schild D. and Neumann T. (2018) Retention and multiphase transformation of selenium oxyanions during the formation of magnetite via iron(ii) hydroxide and green rust. *Dalton Transactions* **47**, 11002-11015.
- Breynaert E., Bruggeman C. and Maes A. (2008) XANES–EXAFS Analysis of Se Solid-Phase Reaction Products Formed upon Contacting Se(IV) with FeS<sub>2</sub> and FeS. *Environmental Science & Technology* **42**, 3595-3601.
- Chakraborty S., Bardelli F. and Charlet L. (2010) Reactivities of Fe(II) on Calcite: Selenium Reduction. *Environmental Science & Technology* **44**, 1288-1294.
- Charlet L., Kang M., Bardelli F., Kirsch R., Géhin A., Grenèche J.-M. and Chen F. (2012) Nanocomposite Pyrite–Greigite Reactivity toward Se(IV)/Se(VI). *Environmental Science & Technology* **46**, 4869-4876.
- Charlet L., Scheinost A. C., Tournassat C., Grenèche J.-M., Géhin A., Fernandez-Martinez A., Coudert S., Tisserand D. and Brendle J. (2007) Electron transfer at the mineral/water interface: Selenium reduction by ferrous iron sorbed on clay. *Geochimica et Cosmochimica Acta* **71**, 5731–5749.
- Curti E., Aimoz L. and Kitamura A. (2013) Selenium uptake onto natural pyrite. *Journal of Radioanalytical and Nuclear Chemistry* **295**, 1655-1665.
- Curti E., Puranen A., Grolimund D., Jädernas D., Sheptyakov D. and Mesbah A. (2015) Characterization of selenium in UO<sub>2</sub> spent nuclear fuel by micro X-ray absorption spectroscopy and its thermodynamic stability. *Environmental Science: Processes &*

*Impacts* **17**, 1760-1768.

- Diener A., Neumann T., Kramar U. and Schild D. (2012) Structure of selenium incorporated in pyrite and mackinawite as determined by XAFS analyses. *Journal of Contaminant Hydrology* **133**, 30-39.
- Fernández-Martínez A. and Charlet L. (2009) Selenium environmental cycling and bioavailability: a structural chemist point of view. *Reviews in Environmental Science and Bio/Technology* **8**, 81-110.
- Fordyce F. M. (2013) Selenium Deficiency and Toxicity in the Environment. In *Essentials of Medical Geology: Revised Edition* (ed. O. Selinus). Springer Netherlands, Dordrecht. pp. 375-416.
- Frasca B., Savoye S., Wittebroodt C., Leupin O. X. and Michelot J. L. (2014) Comparative study of Se oxyanions retention on three argillaceous rocks: Upper Toarcian (Tournemire, France), Black Shales (Tournemire, France) and Opalinus Clay (Mont Terri, Switzerland). *Journal of Environmental Radioactivity* **127**, 133-140.
- Frechou C., Aguerre S., Degros J.-P., Kerlau G. and Grangeon T. (2007) Improvement of a radiochemical separation for selenium 79: Applications to effluents and nuclear wastes. *Talanta* **72**, 1166-1171.
- Gorski C. A., Klupfel L., Voegelin A., Sander M. and Hofstetter T. B. (2012a) Redox properties of structural Fe in clay minerals. 2. Electrochemical and spectroscopic characterization of electron transfer irreversibility in ferruginous smectite, SWa-1. *Environ Sci Technol* **46**, 9369-9377.
- Gorski C. A., Klupfel L. E., Voegelin A., Sander M. and Hofstetter T. B. (2013) Redox properties of structural Fe in clay minerals: 3. Relationships between smectite redox and structural properties. *Environ Sci Technol* **47**, 13477-13485.
- Greenwood N. N. and Earnshaw A. (2012) *Chemistry of the Elements*. Elsevier.
- Gurunath S., Pradeep Kumar S., Basavaraj N. K. and Patil P. A. (2013) Amorphous solid dispersion method for improving oral bioavailability of poorly water-soluble drugs. *Journal of Pharmacy Research* **6**, 476-480.
- Hammouh F., Zein S., Amr R., Ghazzawi H., Muharib D., Al Saad D. and Subih H. (2021) Assessment of dietary selenium intake of Jordanian adults in Madaba: a cross sectional study. *Nutrition & Food Science* **51**, 494-506.
- Hoving A. L., Sander M., Bruggeman C. and Behrends T. (2017) Redox properties of clay-rich sediments as assessed by mediated electrochemical analysis: Separating pyrite, siderite and structural Fe in clay minerals. *Chemical Geology* **457**, 149-161.
- Huang J., Jones A., Waite T. D., Chen Y., Huang X., Rosso K. M., Kappler A., Mansor M., Tratnyek P. G. and Zhang H. (2021) Fe(II) Redox Chemistry in the Environment. *Chemical Reviews* **121**, 8161-8233.
- Jaisi D. P., Liu C., Dong H., Blake R. E. and Fein J. B. (2008b) Fe<sup>2+</sup> sorption onto nontronite



- (NAu-2). *Geochimica et Cosmochimica Acta* **72**, 5361-5371.
- Jordan N., Lomenech C., Marmier N., Giffaut E. and Ehrhardt J.-J. (2009) Sorption of selenium(IV) onto magnetite in the presence of silicic acid. *Journal of Colloid and Interface Science* **329**, 17-23.
- Jordan N., Ritter A., Scheinost A. C., Weiss S., Schild D. and Hübner R. (2014) Selenium(IV) Uptake by Maghemite ( $\gamma$ -Fe<sub>2</sub>O<sub>3</sub>). *Environmental Science & Technology* **48**, 1665-1674.
- Jordan N., Ritter A., Foerstendorf H., Scheinost A. C., Weiß S., Heim K., Grenzer J., Mücklich A. and Reuther H. (2013) Adsorption mechanism of selenium(VI) onto maghemite. *Geochimica et Cosmochimica Acta* **103**, 63-75.
- Li S., Xiao T. and Zheng B. (2012) Medical geology of arsenic, selenium and thallium in China. *Science of The Total Environment* **421-422**, 31-40.
- López de Arroyabe Loyo R., Nikitenko S. I., Scheinost A. C. and Simonoff M. (2008) Immobilization of Selenite on Fe<sub>3</sub>O<sub>4</sub> and Fe/Fe<sub>3</sub>C Ultrasmall Particles. *Environmental Science & Technology* **42**, 2451-2456.
- M. Marques Fernandes and Baeyens B. (2020) Competitive adsorption on illite and montmorillonite: Experimental and modelling investigations, Nagra Technical Report NTB 19-05, Nagra, Wettingen, Switzerland.
- Ma B., Charlet L., Fernandez-Martinez A., Kang M. and Madé B. (2019) A review of the retention mechanisms of redox-sensitive radionuclides in multi-barrier systems. *Applied Geochemistry* **100**, 414-431.
- MacFarquhar J. K., Broussard D. L., Melstrom P., Hutchinson R., Wolkin A., Martin C., Burk R. F., Dunn J. R., Green A. L., Hammond R., Schaffner W. and Jones T. F. (2010) Acute selenium toxicity associated with a dietary supplement. *Arch Intern Med* **170**, 256-261.
- Manceau A. and Charlet L. (1994) The Mechanism of Selenate Adsorption on Goethite and Hydrrous Ferric Oxide. *Journal of Colloid and Interface Science* **168**, 87-93.
- Masscheleyn P. H., Delaune R. D. and Patrick W. H., Jr. (1990) Transformations of selenium as affected by sediment oxidation-reduction potential and pH. *Environmental Science & Technology* **24**, 91-96.
- Minaev V. S., Timoshenkov S. P. and Kalugin V. V. (2005) STRUCTURAL AND PHASE TRANSFORMATIONS IN CONDENSED SELENIUM. *Journal of Optoelectronics and Advanced Materials* **7**, 1717-1741.
- Missana T., Alonso U. and García-Gutiérrez M. (2009) Experimental study and modelling of selenite sorption onto illite and smectite clays. *Journal of Colloid and Interface Science* **334**, 132-138.
- Moreno-Reyes R., Egrise D., Nève J., Pasteels J.-L. and Schoutens A. (2001) Selenium Deficiency-Induced Growth Retardation Is Associated with an Impaired Bone

- Metabolism and Osteopenia. *Journal of Bone and Mineral Research* **16**, 1556-1563.
- Myneni S. C. B., Tokunaga T. K. and Brown G. E. (1997) Abiotic Selenium Redox Transformations in the Presence of Fe(II,III) Oxides. *Science* **278**, 1106-1109.
- Olegario J. T., Yee N., Miller M., Szczepaniak J. and Manning B. (2010) Reduction of Se(VI) to Se(-II) by zerovalent iron nanoparticle suspensions. *Journal of Nanoparticle Research* **12**, 2057-2068.
- Onoguchi A., Granata G., Haraguchi D., Hayashi H. and Tokoro C. (2019) Kinetics and mechanism of selenate and selenite removal in solution by green rust-sulfate. *Royal Society Open Science* **6**, 182147.
- Oremland R. S. and Stolz J. (2000) Dissimilatory Reduction of Selenate and Arsenate in Nature. In *Environmental Microbe - Metal Interactions*. pp. 199-224.
- Peak D., Saha U. K. and Huang P. M. (2006) Selenite Adsorption Mechanisms on Pure and Coated Montmorillonite: An EXAFS and XANES Spectroscopic Study. *Soil Science Society of America Journal* **70**, 192-203.
- Pearce C. I., Coker V. S., Charnock J. M., Patrick R. A. D., Mosselmans J. F. W., Law N., Beveridge T. J. and Lloyd J. R. (2008) Microbial manufacture of chalcogenide-based nanoparticles via the reduction of selenite using *Veillonella atypica*: an in situ EXAFS study. *Nanotechnology* **19**, 155603.
- Peigneur P. (1976 ) Stability and adsorption affinity of some transition metal-amine complexes in aluminosilicates. Ph.D Thesis, Univ. Leuven, Belgium.
- Persch C., Müller M. J., Yadav A., Pries J., Honné N., Kerres P., Wei S., Tanaka H., Fantini P., Varesi E., Pellizzer F. and Wuttig M. (2021) The potential of chemical bonding to design crystallization and vitrification kinetics. *Nature Communications* **12**, 4978.
- Poulain A., Fernandez-Martinez A., Greneche J.-M., Prieur D., Scheinost A. C., Menguy N., Bureau S., Magnin V., Findling N., Drnec J., Martens I., Mirolo M. and Charlet L. (2022) Selenium Nanowire Formation by Reacting Selenate with Magnetite. *Environmental Science & Technology* **56**, 14817-14827.
- Qian Y., Scheinost A. C., Grangeon S., Greneche J.-M., Hoving A., Bourhis E., Maubec N., Churakov S. V. and Fernandes M. M. (2023) Oxidation State and Structure of Fe in Nontronite: From Oxidizing to Reducing Conditions. *ACS Earth and Space Chemistry* **7**, 1868-1881.
- Rayman M. P. (2012) Selenium and human health. *The Lancet* **379**, 1256-1268.
- Ressler T. (1998) WinXAS: A program for X-ray absorption spectroscopy data analysis under MS-Windows. *Journal of Synchrotron Radiation* **5**, 118-122.
- Rodriguez D. M., Mayordomo N., Scheinost A. C., Schild D., Brendler V., Müller K. and Stumpf T. (2020) New insights into <sup>99</sup>Tc(VII) removal by pyrite: a spectroscopic approach. *Environ. Sci. Technol.* **54**, 2678-2687.

- Rojo H., Scheinost A. C., Lothenbach B., Laube A., Wieland E. and Tits J. (2018) Retention of selenium by calcium aluminate hydrate (AFm) phases under strongly-reducing radioactive waste repository conditions. *Dalton Transactions* **47**, 4209-4218.
- Rossberg A., Reich T. and Bernhard G. (2003) Complexation of uranium (VI) with protocatechuic acid—application of iterative transformation factor analysis to EXAFS spectroscopy. *Analytical and bioanalytical chemistry* **376**, 631-638.
- Scheinost A. C. and Charlet L. (2008) Selenite reduction by mackinawite, magnetite and siderite: XAS characterization of nanosized redox products. *Environmental science & technology* **42**, 1984-1989.
- Scheinost A. C., Kirsch R., Banerjee D., Fernandez-Martinez A., Zaenker H., Funke H. and Charlet L. (2008) X-ray absorption and photoelectron spectroscopy investigation of selenite reduction by FeII-bearing minerals. *Journal of Contaminant Hydrology* **102**, 228-245.
- Scheinost A. C., Claussner J., Exner J., Feig M., Findeisen S., Hennig C., Kvashnina K. O., Naudet D., Prieur D., Rossberg A., Schmidt M., Qiu C., Colomp P., Cohen C., Dettona E., Dyadkin V. and Stumpf T. (2021) ROBL-II at ESRF: a synchrotron toolbox for actinide research. *Journal of Synchrotron Radiation* **28**, 333-349.
- Séby F., Potin-Gautier M., Giffaut E., Borge G. and Donard O. F. X. (2001) A critical review of thermodynamic data for selenium species at 25°C. *Chemical Geology* **171**, 173-194.
- Soltermann D., Marques Fernandes M., Baeyens B., Mieke-Brendle J. and Dahn R. (2014b) Competitive Fe(II)-Zn(II) uptake on a synthetic montmorillonite. *Environ Sci Technol* **48**, 190-198.
- Stucki J., Golden D. and Roth C. (1984a) Preparation and Handling of Dithionite-Reduced Smectite Suspensions. *Clays and Clay Minerals - CLAYS CLAY MINER* **32**, 191-197.
- Tan L. C., Nanchaiah Y. V., van Hullebusch E. D. and Lens P. N. (2018) Selenium: environmental significance, pollution, and biological treatment technologies. *Anaerobic treatment of mine wastewater for the removal of selenate and its co-contaminants*, 9-71.
- Titov A. F., Kaznina N. M., Karapetyan T. A., Dorshakova N. V. and Tarasova V. N. (2022) Role of Selenium in Plants, Animals, and Humans. *Biology Bulletin Reviews* **12**, 189-200.
- Van Olphen H., Fripiat J. J., Organisation for Economic C.-o., Development and Clay Minerals S. (1979) *Data handbook for clay materials and other non-metallic minerals : providing those involved in clay research and industrial application with sets of authoritative data describing the physical and chemical properties and mineralogical composition of the available reference materials*. Pergamon Press.
- Vantelon D., Montarges-Pelletier E., Michot L. J., Pelletier M., Thomas F. and Briois V. (2003) Iron distribution in the octahedral sheet of dioctahedral smectites. *An Fe K-*

edge X-ray absorption spectroscopy study. *Physics and Chemistry of Minerals* **30**, 44-53.

Volfson I. F., Farrakhov E. G., Pronin A. P., Beiseyev O. B., Beiseyev A. O., Bogdasarov M. A., Oderova A. V., Pechenkin I. G., Khitrov A. E. and Pikhur O. L. (2010) Medical Geology in Russia and the NIS. In *Medical Geology: A Regional Synthesis*. Springer. pp. 221-258.

W. Hummel T. T. (2023) The PSI chemical thermodynamic database 2020, Nagra Technical Report NTB 21-03, Nagra, Wettingen, Switzerland.

Webb S. M. (2005) SIXpack: a graphical user interface for XAS analysis using IFEFFIT. *Physica Scripta* **2005**, 1011.

Wiberg E. and Wiberg N. (2001) *Inorganic chemistry*. Academic press.

Winkel L. H. E., Johnson C. A., Lenz M., Grundl T., Leupin O. X., Amini M. and Charlet L. (2012) Environmental Selenium Research: From Microscopic Processes to Global Understanding. *Environmental Science & Technology* **46**, 571-579.

Yalçıntaş E., Scheinost A. C., Gaona X. and Altmaier M. (2016a) Systematic XAS study on the reduction and uptake of Tc by magnetite and mackinawite. *Dalton Trans.* **45**, 17874-17885.

Zhang P. and Sparks D. L. (1990) Kinetics of selenate and selenite adsorption/desorption at the goethite/water interface. *Environmental Science & Technology* **24**, 1848-1856.

Zoroufchi Benis K., McPhedran K. N. and Soltan J. (2022) Selenium removal from water using adsorbents: A critical review. *Journal of Hazardous Materials* **424**, 127603.

### 3.6 Supporting information

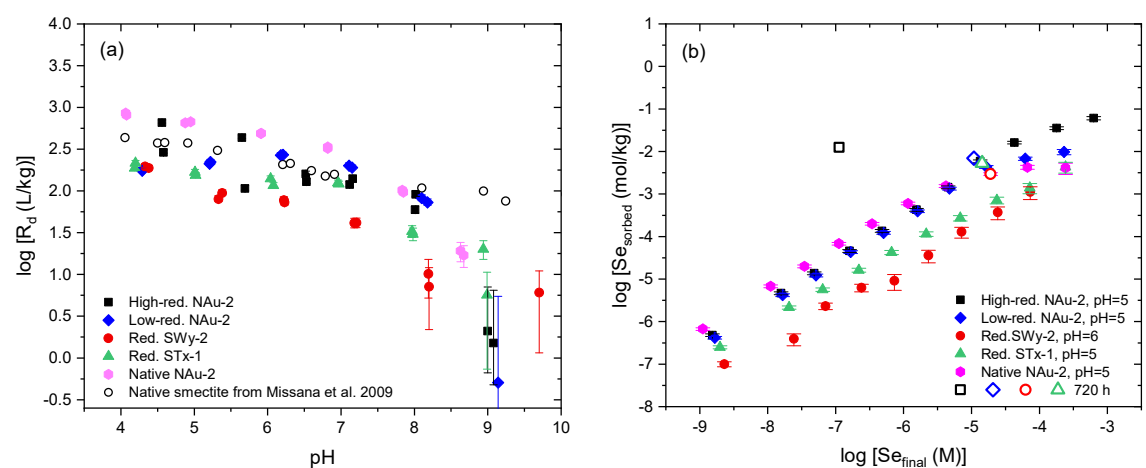


Fig. S3.1. Selenite sorption on high-red. NAu-2, low-red. NAu-2, red. SWy-2, red. STx-1, and native NAu-2 at S/L of 2 g/L, 0.1 M NaCl. (a) Sorption edge at  $[Se]_{init} = 6 \times 10^{-8} \text{ M}$  after 7 days, (b) Sorption isotherm at pH 5 ~ 6 after 7 days (solid symbols) and 720 h (hollow symbols).

## **Chapter 4: The retention of technetium by Fe-bearing clay minerals**

*In preparation for publication*

## Abstract

A comprehensive understanding of technetium (Tc) retention on Fe-bearing clay minerals is crucial for the safety assessment of deep geological repositories, given the long half-life and radiotoxicity of Tc. Tc reductive retention is an effective method for impeding its migration. Nevertheless, the precise retention mechanism remains unclear. This study undertakes an examination of Tc(VII) retention on Fe-bearing clay minerals, with a specific focus on the structural Fe(II) content in relation to redox potential, pH, and Tc concentration. Batch sorption experiments of Tc(VII) on clays with different total Fe(II) contents were conducted to analyze the retention behavior. Molecular-scale interactions between Tc and clay minerals were investigated using X-ray Absorption Fine Structure (XAFS) spectroscopy, Scanning Electron Microscopy (SEM), and Transmission Electron Microscopy (TEM). The findings revealed Tc retention on reduced clay minerals, whereas native clay minerals confirmed no such retention. Additionally, Tc retention on reduced clay minerals increases from  $\log R_d$  of 0.5 L/kg to 2.0 L/kg as the structural Fe(II) content increases from 0.6 wt% to 11.4 wt% and is normalized to a unified retention value ( $\log R_d \approx 3.0$  L/kg) by the amount of structural Fe(II). Furthermore, Tc retention shows a linear increase as a function of Tc equilibrium concentration up to  $10^{-5.5}$  M, however, this behavior diverges based on the structural Fe(II) content.  $\text{TcO}_2 \cdot n\text{H}_2\text{O}$  was identified as the sole reduced species, and no surface-complexed (adsorbed) Tc(IV) species could be detected, even at very low Tc loadings around 35 ppm. Consequently, an outer-sphere electron transfer mechanism was hypothesized in Tc retention. This understanding of Tc retention provides valuable insights for Tc remediation and risk assessment.

Keywords: pertechnetate retention, reductive sorption, Fe-bearing clay minerals,  $\text{TcO}_2 \cdot n\text{H}_2\text{O}$ , hydrogen bond electron transfer.

## 4.1 Introduction

Technetium (Tc) is an artificial metal element without stable isotopes, originating from the fission products of  $^{235}\text{U}$  and  $^{239}\text{Pu}$  in nuclear power plants (Newsome et al., 2014). In spent nuclear fuel,  $^{99}\text{Tc}$  is associated in metallic form with the  $\epsilon$  phase (Poineau et al., 2013). Within vitrified high-level waste (HLW), which results from reprocessed spent fuel and is proposed to be stored in deep geological repositories,  $^{99}\text{Tc}$  exists as a mixture of Tc(IV) and Tc(VII) (Childs et al., 2018; Muller et al., 2014). The release of Tc from HLW into the

geological environment definitely involves its oxidized heptavalent form as the anion  $\text{TcO}_4^-$ , which exhibits high solubility and mobility, presenting a potential for migration from the backfill clay materials of the repository to the biosphere. However, in anoxic and reducing environments,  $\text{Tc(VII)}$  has a tendency to be reduced to  $\text{Tc(IV)}$ , which forms solids with oxygen or sulfur coordination, or hydrous polymers, which occur either free or attached to surfaces (Pearce et al., 2020; Peretyazhko et al., 2008b; Wildung et al., 2000; Zachara et al., 2007). Given its long half-life ( $2.1 \times 10^5$  years) and high toxicity, a good understanding of the migration mechanism and retention methods of Tc on the clay minerals is of significant importance for ensuring an accurate safety assessment.

The migration and retention of Tc are closely linked to its solubility, which is contingent upon its oxidation states. The oxidation states of Tc varies from  $-I$  to  $VII$ , with  $IV$  and  $VII$  being the most stable states (Yu et al., 2022). Under oxidizing conditions, Tc exists as pertechnetate ( $\text{Tc}^{\text{VII}}\text{O}_4^-$ ), which is highly soluble and mobile, leading to negligible adsorption on clay minerals. Conversely, in reducing conditions, Tc is stable as  $\text{Tc(IV)}$ . Due to the remarkably low solubility of  $\text{Tc(IV)}$  ( $10^{-8}$  M) (Yalçıntaş et al., 2016c), it precipitates as insoluble hydrous oxide  $\text{TcO}_2 \cdot n\text{H}_2\text{O}$  (Cui and Eriksen, 1996a). For retaining mobile  $\text{Tc(VII)}$  on clay minerals, reduction and subsequent precipitation as  $\text{TcO}_2 \cdot n\text{H}_2\text{O}$  have been identified as an effective method (Siegel and Bryan, 2014). Clay minerals inherently contain Fe in their structure, and possible adsorbed Fe on their surfaces resulted from steel canister corrosion. In the anoxic condition of repositories, the  $\text{Fe(II)/Fe(III)}$  redox couple of clay minerals exhibits a reducing potential capable of reducing Tc. Consequently, the reduction of  $\text{Tc(VII)}$  by Fe-bearing clay minerals, mediated by the  $\text{Fe(II)/Fe(III)}$  couple, plays a pivotal role in influencing the mobility and bioavailability of Tc.

The redox interactions between  $\text{Tc(VII)}$  and the  $\text{Fe(II)/Fe(III)}$  couple are influenced by various factors, including the  $\text{Fe(II)}$  content and distribution associated with clay minerals, redox potential, pH, and Tc concentration.  $\text{Fe(II)}$  in the structure of clay minerals ( $\text{Fe(II)}_{\text{str}}$ ) has been shown to reduce  $\text{Tc(VII)}$  (Bishop et al., 2011; Cui and Eriksen, 1996b; Jaisi et al., 2008a; Jaisi et al., 2009; Pearce et al., 2020; Peretyazhko et al., 2008b; Wildung et al., 2004; Yang et al., 2012). Additionally, adsorbed  $\text{Fe(II)}$  on mineral surfaces ( $\text{Fe(II)}_{\text{ad}}$ ) has been identified as another agent for  $\text{Tc(VII)}$  reduction (Burke et al., 2005; Burke et al., 2006; Fredrickson et al., 2004; McBeth et al., 2007; Pearce et al., 2020; Peretyazhko et al., 2008b; Wildung et al., 2004; Zachara et al., 2007). Notably, the reactivity of different  $\text{Fe(II)}$  species—namely  $\text{Fe(II)}_{\text{str}}$ ,  $\text{Fe(II)}_{\text{ad}}$ , and aqueous  $\text{Fe}^{2+}_{\text{aq}}$ —varies in their ability to drive



Tc(VII) reduction (Jaisi et al., 2008a). Among these species, Fe(II)<sub>ad</sub> exhibits the highest reactivity, followed by Fe(II)<sub>str</sub>, while Fe<sup>2+</sup><sub>aq</sub> displays the least reactivity. Cui et al. highlighted that despite the thermodynamic feasibility of Tc(VII) reduction to Tc(IV) by Fe<sup>2+</sup><sub>aq</sub>, the process is hindered kinetically. At pH values below 7.5, no observable reaction occurred, and beyond this point, Fe<sup>2+</sup><sub>aq</sub> underwent gradual precipitation as a mixture of FeCO<sub>3</sub>(s) and Fe(OH)<sub>2</sub>(s) (Cui and Eriksen, 1996b). Zachara et al. emphasized the pH dependence of abiotic Tc(VII) reduction by Fe<sup>2+</sup><sub>aq</sub>, noting that reduction was evident at pH 7 and pH 8, but not at pH 6, even after a month's duration (Zachara et al., 2007). Given the extensive studies into the homogeneous reduction of Tc(VII) by Fe<sup>2+</sup><sub>aq</sub>, this study will not be investigated further into this aspect. In addition to the varied Fe(II) species, the content of Fe(II)<sub>str</sub>, acting as an electron donor, also exerts an influence on the reduction of Tc(VII). Furthermore, differing Fe(II)<sub>str</sub> contents give rise to distinct Fe(II)/Fe(III) couples, yielding disparate redox potentials (Gorski et al., 2013; Qian et al., 2023). The impact of pH on the Tc(VII) and clay-Fe(II) redox interaction has not been systematically investigated. Jaisi et al. only compared three pH values 5.5, 7.0, and 8.5 (Jaisi et al., 2009), while Peretyazhko et al. solely presented data for pH 6 to 7 (Peretyazhko et al., 2008b). Similarly, a comprehensive study regarding the influence of Tc(VII) concentration on its retention is yet to be conducted. TcO<sub>2</sub> precipitation, resulting from the low solubility of Tc(IV), is established as the main reduction product (Icenhower et al., 2010; Oliveira et al., 2022; Yalçıntaş et al., 2016c). However, less is understood about whether the concentration of Tc(VII) impacts the amount of Tc retention and thus affects the size and structural configuration of TcO<sub>2</sub> precipitation. Clay minerals, characterized by their negatively charged layer structures (Chorom and Rengasamy, 1995), exhibit strong cation adsorption properties. Consequently, TcO<sub>4</sub><sup>-</sup> anions inducing repulsive forces lead to low and even absent adsorption capacity (Wilmarth et al., 2011). This prompts the question: In cases where TcO<sub>4</sub><sup>-</sup> is not adsorbed onto clay minerals, how are then the electrons transferred from structural or adsorbed Fe to Tc to induce the redox reaction? To study the redox interplay of Tc(VII) and Fe(II), X-ray Absorption Fine Structure (XAFS) analysis is commonly used for characterizing the Tc reduction products. Due to the considerable quantity of Fe(II)<sub>str</sub> within clay minerals compared to the limited Tc presence, the minute differences in Fe(II)<sub>str</sub> pre- and post-redox reaction prove challenging to discern via XAFS. It is important to investigate a range of Tc concentrations and select a suitable Tc retention amount for XAFS analysis. This approach is crucial for advancing our understanding of these intricate interfacial

reactions.

In this study, we investigate systematically the redox reaction between Tc(VII) and Fe(II)/Fe(III) couple of clay minerals under different conditions of pH, Tc concentration, and structural Fe(II) content in clay minerals associated with redox potentials. Three types of 2:1 dioctahedral clay minerals, Texas montmorillonite STx-1, Wyoming montmorillonite SWy-2, and nontronite clay NAu-2, were reduced to obtain different amounts of Fe(II)<sub>str</sub>. Sorption experiments on reduced clay minerals as a function of pH and Tc concentration were conducted to evaluate and quantify Tc(VII) retention. XAFS, Scanning Electron Microscopy (SEM), and Transmission Electron Microscopy (TEM) were applied to the Tc-reacted clay samples to identify the speciation, structural configuration, and the distribution of the Tc redox product, with the goal of investigating the relationship between the Fe(II)/Fe(III) couple and Tc(VII) retention. Our study provides insight into Tc(VII) retention from a macroscopic (batch sorption) and a molecular-scale view.

## **4.2 Materials and methods**

### **4.2.1 Clay preparation and reduction**

Three 2:1 dioctahedral clay minerals of different Fe content, Texas montmorillonite STx-1, Wyoming montmorillonite SWy-2, and nontronite clay NAu-2, were obtained from the Clay Source Repository of the Clay Minerals Society (Purdue University, West Lafayette, IN). Clay powders were prepared to clay suspension, conditioned to Na-form, and reduced chemically with Citrate-Bicarbonate-Dithionite (CBD) method (Stucki et al., 1984a) to obtain varying Fe(II)<sub>str</sub> content as red STx-1, red SWy-2, low-red NAu-2, and high-red NAu-2. The purified native clay suspension was initially mixed with Citrate-Bicarbonate (CB) buffer solution ( $\text{Na}_3\text{C}_6\text{H}_5\text{O}_7 \cdot 2\text{H}_2\text{O}$  and  $\text{NaHCO}_3$ ), followed by the addition of dithionite ( $\text{Na}_2\text{S}_2\text{O}_4$ ). In the case of red STx-1, red SWy-2, and high-red NAu-2, the amount of added dithionite was three times the mass of the clay, corresponding to a molar ratio of S/Fe of 10. For low-red NAu-2, 1.3 g of dithionite were added, resulting in a molar ratio of S/Fe of 0.5. After overnight end-to-end shaking, the reduced clay suspensions underwent washing in dialysis bags. Initially, they were washed with 1 M NaCl at pH 4 approximately ten times, followed by further washing with 0.1 M NaCl without pH adjustment until the matrix of the clay suspension matched that of 0.1 M NaCl, as well as the added chemicals were less than  $10^{-9}$  M. The preparation processes and Fe(II) content determination were described in detail in the previous work (Qian et al., 2023).

#### 4.2.2 Tc sorption experiments

Tc sorption edge and sorption isotherm experiments were conducted in 0.1 M NaCl at 2 g/L in duplication in an anoxic glovebox ( $O_2 < 0.1$  ppm). All the solutions in this experiment were prepared with Milli-Q water ( $18\text{ M}\Omega\text{ cm}^{-1}$ , Millipore) and degassed with  $N_2$  before transferring into the glovebox to prevent introduction of oxygen and  $CO_2$ .

Sorption edge batch experiments were conducted with  $^{99}\text{Tc}$  trace concentration ( $1 \times 10^{-7}$  M) as a function of pH from 3 to 9. The stock solution of Tc was prepared by dissolving  $\text{NaTcO}_4$  in 0.1 M HCl. Due to the big buffer capacity of reduced clays, the pH of reduced clay suspensions was adjusted with HCl or NaOH accordingly before sorption experiments to have a better pH interval. Afterwards,  $^{99}\text{Tc}$  trace solution, 0.1 NaCl, pH buffer, and clay suspension were added into a centrifuge tube (Backman 26 mL) to a total volume of 22 mL. The pH buffers are HCl at pH 3, acetate ( $\text{CH}_3\text{COONa} \cdot 3\text{H}_2\text{O}$ ) at pH 4 and 5, MES (2-(N-morpholino)ethanesulfonic acid) at pH 6, MOPS (3-(N-morpholino) propanesulfonic acid) at pH 7, and TRIS (Tris(hydroxymethyl)aminomethane) at pH 8 and 9 at a concentration of  $2 \times 10^{-3}$  M (Bradbury and Baeyens, 2002). Yang et al. demonstrated that the equilibrium of Tc(VII) reduction on reduced NAu-2 is achieved in about 50 hours (Yang et al., 2012), thereby confirming the attainment of equilibrium after 7 days in this study. After 7 days of continuous end-to-end shaking, centrifuge tubes were centrifuged at 40,000 g (Backman Coulter Optima™ L-100 XP Ultracentrifuge, 70 Tirotor) for an hour. Two aliquots of the supernatant were taken immediately for radiochemical assays of  $^{99}\text{Tc}$  using a beta liquid scintillation counter (Tri-Carb 4910 TR), and the pH was measured using a Metrohm pH electrode. The sorption is expressed by the logarithm of the distribution coefficient,  $R_d$ , defined in equation (4.1).

$$R_d = \frac{[C_{\text{init}}] - [C_{\text{eq}}]}{[C_{\text{eq}}]} \cdot \frac{V}{m} \quad (\text{L/kg}) \quad (4.1)$$

where  $C_{\text{init}}$ : initial concentration of  $^{99}\text{Tc}$  (M),  $C_{\text{eq}}$ : equilibrium concentration of  $^{99}\text{Tc}$  (M),  $V$ : total volume of the liquid phase (L),  $m$ : mass of the solid phase (kg).

Sorption isotherm batch experiments were performed as a function of  $^{99}\text{Tc}$  concentration varying from  $9 \times 10^{-8}$  M to  $3 \times 10^{-4}$  M at pH 5 and 7. The experiment procedures were the same as Tc sorption edge experiments. The sorption of Tc is displayed by the logarithm of the element sorbed amount in equation (4.2).

$$\text{Sorbed} = ([C_{\text{init}}] - [C_{\text{eq}}]) \cdot \frac{V}{m} \quad (\text{mol/kg}) \quad (4.2)$$

Where  $C_{\text{init}}$ : initial concentration of  $^{99}\text{Tc}$  (M),  $C_{\text{eq}}$ : equilibrium concentration of  $^{99}\text{Tc}$  (M),

V: total volume of the liquid phase (L), m: mass of the solid phase (kg).

#### **4.2.3 X-ray absorption spectroscopy**

The clay wet pastes after centrifugation were put into a High-Density Polyethylene (HDPE) double-confinement sample holder, and the holder was then heat-sealed inside the glovebox ( $O_2 < 0.1$  ppm). After being taken out of the glovebox, samples were immediately flash-frozen in  $LN_2$ . The samples were preserved and transported to the beamline in a  $LN_2$  dewar and subsequently transferred to the He-cryostat of the beamline within less than 5 minutes to keep them frozen. Note that gamma spectrometry measurements for quantitative radionuclide inventory and test for surface contamination were done both at the shipping institution (PSI) as well at the receiving institution (ESRF) on dry ice, again to prevent the thawing of the samples.

The measurements were carried out at the Rossendorf Beamline (ROBL) BM20 of the European Synchrotron Radiation Facility (ESRF), France (Scheinost et al., 2021). The setup for the beamline and experiments were described in detail in the previous work (Qian et al., 2023). The energy of the incoming beam was calibrated with a Mo foil K-edge (20000 eV). Tc K-edge spectra were collected in fluorescence mode at 15 K with an 18-element Ge-detector (Mirion) at an energy step of 0.5 eV using a Si(111) double crystal monochromator. Rejection of higher harmonics was obtained by using two Rh-coated mirrors at 2.5 mrad grazing incidence. Each sample was subjected to multiple repeated measurements to ensure a sufficiently low noise level. The spectra were corrected for fluorescence deadtime and averaged using Sixpack (Webb, 2005). Normalization, conversion into k-space and background subtraction were performed with WinXAS using the autospline function (Ressler, 1998).

#### **4.2.4 Transmission electron microscope**

The TEM measurements were conducted at the Electron Microscopy Facility in PSI, Switzerland. A drop of clay suspension were placed and dried on a Cu grid with lacey carbon films loaded in the glovebox. Transmission electron microscopy (TEM) experiments were performed at 200 keV using a NeoARM/JEM-ARM200F probe-corrected transmission electron microscope from JEOL, equipped with a cold-FEG (field-emission gun) and a JEOL-EDX system (energy dispersive X-ray spectroscopy).

## 4.3 Results and discussion

### 4.3.1 Tc sorption edge

In our earlier investigation, we conducted a comprehensive comparison of clay properties between native and reduced clays (Qian et al., 2023). This included an assessment of clay dissolution, morphology, structure, cation exchange capacity (CEC), and the availability of surface edge sites. Our findings revealed no significant alterations in the morphology and structure of reduced clays when compared to their counterparts in the native state. Only a limited dissolution of the external layers of the clay platelets was discernible. Moreover, no secondary mineral phases were detected in the reduced clays after rigorous washing procedures. The CEC and surface edge sites of the reduced clays closely resembled those of the native clays. Consequently, the surface properties of the reduced clays exhibit negligible differences when compared to the native clays. The comprehensive understanding of the clay structure and surface properties provides a good basis for investigating Tc retention behavior.

Figure 4.1a illustrates the Tc sorption behavior as a function of pH. The kinetic study of Tc(VII) reduction on reduced NAu-2 by Yang et al. (2012) revealed that equilibrium is attained in approximately 50 hours, thus confirming that equilibrium is certainly reached after 7 days in this study. Native clay SWy-2 exhibits negligible Tc retention across the entire pH range. Chorom et al. (1995) have previously indicated that native smectite carries a negative zeta potential at pH 2-10 (Brigatti et al., 2013), resulting in repulsion between the native clay and pertechnetate anions, hence leading to negligible retention. Moreover, Tc is a strong acid with low pKa ( $\text{HTcO}_4 \rightleftharpoons \text{H}^+ + \text{TcO}_4^-$ ,  $\text{pKa}=0.32$ ) (Omori et al., 1995), indicating that  $\text{TcO}_4^-$  has a low affinity to stay bound with protons. Conversely, all reduced clays, regardless of the amount of  $\text{Fe(II)}_{\text{str}}$  content, display Tc retention. A comparison with sorption outcomes from native clay containing solely Fe(III) makes it evident that Fe(II) drives pertechnetate retardation.

Among all the reduced clay minerals, the retention of Tc varies, as depicted in Figure 4.1a. Red STx-1 (0.6 wt%  $\text{Fe(II)}_{\text{str}}$ ) exhibits the lowest Tc retention ( $\log R_d \approx 0.5$  L/kg), while red SWy-2 (2.5 wt%  $\text{Fe(II)}_{\text{str}}$ ) and low-red NAu-2 (4.2 wt%  $\text{Fe(II)}_{\text{str}}$ ) display similar levels of Tc retention ( $\log R_d \approx 1.5$  L/kg). High-red NAu-2 (11.4 wt%  $\text{Fe(II)}_{\text{str}}$ ) presents the highest level of Tc retention ( $\log R_d \approx 2.0$  L/kg) among the reduced clay minerals. Based on the results, Tc retention increases with increasing  $\text{Fe(II)}_{\text{str}}$  content in the reduced clay minerals. When the Tc retention in Figure 4.1a is normalized by the  $\text{Fe(II)}_{\text{str}}$  content in each

clay, a unified Tc retention value ( $\log R_d \approx 3.0$  L/kg) is obtained for all four reduced clay minerals for  $\text{pH} < 8$  in Figure 4.1b. However, for  $\text{pH} > 8$ , the retention of Tc drops to zero ( $\log R_d \approx 0$  L/kg) for all clays.

From pH 3 to 8, the retention of Tc on red STx-1, red SWy-2, and low-red NAu-2 is relatively constant. At low pH, Tc can approach the protonated edge site adequately, facilitating an electron transfer. Conversely, as the pH exceeds 8, the increasing repulsion between the deprotonated edge site and Tc anion becomes dominant, impeding any electron transfer.

In Figure 4.1a, the high-red NAu-2 exhibits a significant rise (shadowed area) in Tc retention between pH 6.5 and 7.5. High-red NAu-2, being a clay rich in iron, is expected to have a higher concentration of  $\text{Fe}^{2+}_{\text{aq}}$  in the clay suspension due to the clay dissolution equilibrium ( $\sim 1.6 \times 10^{-3}$  M). Literature has documented substantial  $\text{Fe}^{2+}_{\text{aq}}$  adsorption onto clay surfaces between pH 6.5 and 7.5 (Jaisi et al., 2008a; Soltermann et al., 2014a; Soltermann et al., 2014c). Therefore, in the pH range of  $> 6$ ,  $\text{Fe}^{2+}_{\text{aq}}$  gets adsorbed onto the clay surface, leading to the formation of  $\text{Fe(II)}_{\text{ad}}$  species. Among various Fe(II) species,  $\text{Fe(II)}_{\text{ad}}$  exhibits the highest reactivity (Jaisi et al., 2008a), because the  $\text{Fe(II)}_{\text{ad}}$  acts as a catalyst on the clay surface to facilitate the heterogeneous interface reaction between Tc near the clay surface and Fe in the clay minerals. Therefore,  $\text{Fe(II)}_{\text{ad}}$  reinforces the Tc retention.

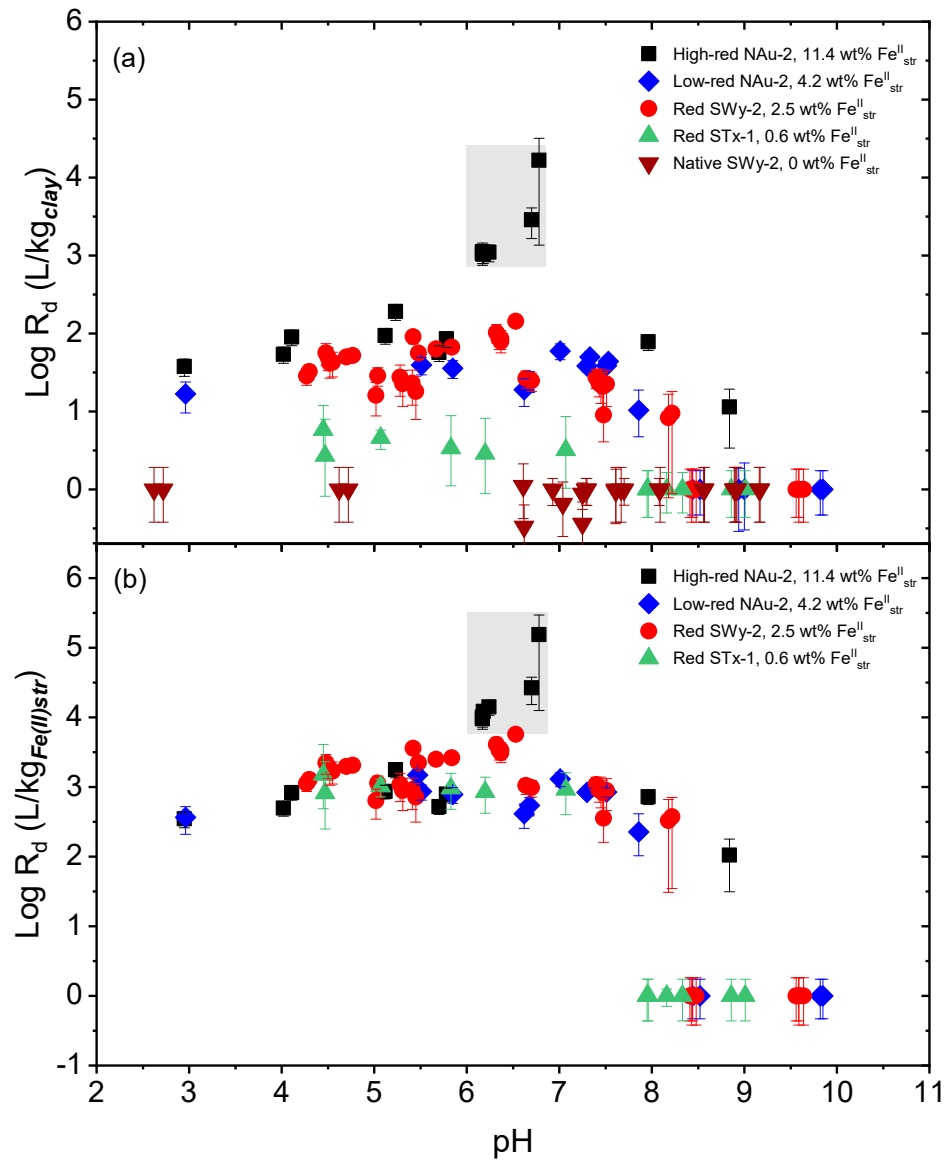


Figure 4.1. Tc retention on native SWy-2, red STx-1, red SWy-2, low-red NAu-2, and high-red NAu-2 as a function of pH at S/L of 2 g/L,  $[\text{Tc}]_{\text{init}} = 1 \times 10^{-7} \text{ M}$ , and 0.1 M NaCl after 7 days. (a)  $R_d$  per kg clay, (b)  $R_d$  per kg Fe(II) in each type of reduced clay. See text for an explanation of the data in the grey squares.

#### 4.3.2 Tc sorption isotherm

Figure 4.2 illustrates Tc retention as a function of Tc concentration at both pH 5 and 7. The influence of  $\text{Fe(II)}_{\text{ad}}$  is evident at pH 6.5 – 7.5 in Figure 4.1, hence, sorption isotherm experiments were conducted at pH 5 to address essentially the effect of  $\text{Fe(II)}_{\text{str}}$  on the retention, while at pH 7, the joint effect of  $\text{Fe(II)}_{\text{str}}$  and  $\text{Fe(II)}_{\text{ad}}$  on sorption behavior was examined.

At pH 5 (Figure 4.2a), Tc retention displays a linear increase with a slope of 1 ( $R^2=0.99$ )

when the equilibrium concentration remains below  $10^{-5.5}$  M. This linear sorption pattern suggests that Tc retention occurs on the same clay site, with the slope value indicating the retention ability at that specific site. For Tc equilibrium concentrations exceeding  $10^{-5.5}$  M, Tc retention behaves in different ways. High-red NAu-2 demonstrates very high Tc retention, leading to low Tc concentration in the equilibrium suspension. As a result, the high retention points are found in a low Tc equilibrium concentration. The rapid increase in Tc retention with low Tc equilibrium concentration suggests noticeable precipitation. In contrast, low-red NAu-2 and red SWy-2 exhibit no sign of precipitation but rather continue with the increase and gradually move towards a plateau. Tc retention for red STx-1 also tends toward a plateau immediately after reaching the Tc equilibrium concentration of  $10^{-5.5}$  M, earlier than observed in low-red NAu-2 and red SWy-2. A plateau indicates the saturation point of Tc retention, signifying the maximum retention capacity of the clay. The lower plateau observed for red STx-1 aligns with its lower  $\text{Fe(II)}_{\text{str}}$  content, which results in a smaller retention capacity compared to red SWy-2 and low-red NAu-2, possessing higher  $\text{Fe(II)}_{\text{str}}$  content.

At pH 7 (Figure 4.2b), there is no discernible difference in Tc retention among low-red NAu-2, red SWy-2, and red STx-1 when compared to their retention behavior at pH 5. The sole contrast lies with high-red NAu-2, which exhibits heightened Tc retention and a higher slope at pH 7 relative to pH 5. This high Tc retention on high-red NAu-2 leads to a shift towards the region of lower Tc concentrations. This difference in Tc retention isotherm between pH 5 and 7 aligns with the retention behavior observed in sorption edge experiments (Figure 4.1), where  $\text{Fe(II)}_{\text{ad}}$  on high-red NAu-2 contributes to elevated Tc retention. Moreover, the increased slope might also be attributed to  $\text{Fe(II)}_{\text{ad}}$ , thereby enhancing the retention ability. While macroscopic sorption experiments allow to quantify the Tc retention as a function of pH and Tc concentration, the need for spectroscopy measurements remains paramount for a more profound molecular-level comprehension of Tc retention.



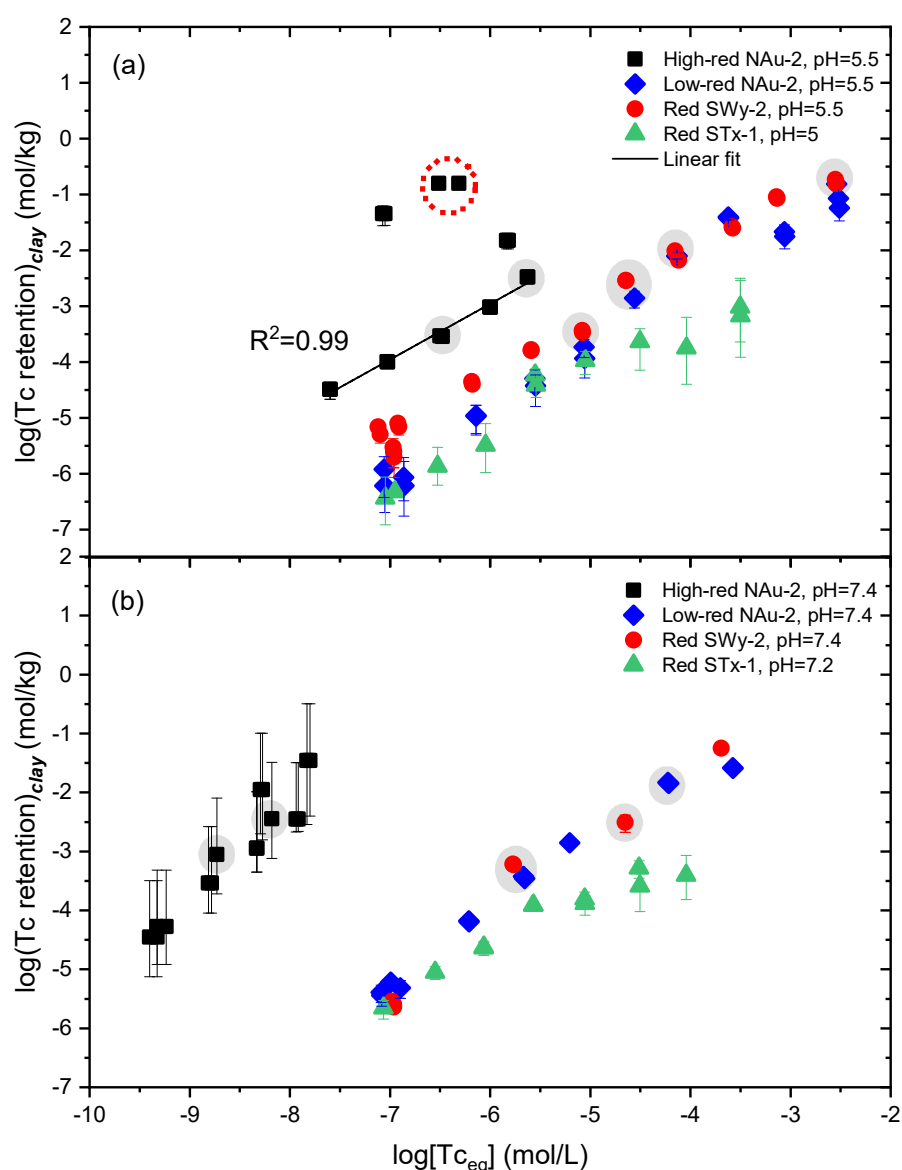


Figure 4.2. Tc retention as a function of Tc concentration at S/L of 2 g/L and 0.1 M NaCl after 7 days. (a) At pH 5 – 5.5, (b) at pH 7.2 – 7.4. Samples marked with grey bullets were measured with XAFS; the sample encircled with red hatched lines was measured with TEM.

#### 4.3.3 Tc K-edge XAFS measurements of sorption isotherm clay samples

Samples with different Tc concentrations, amount of Tc retention, pH, and  $\text{Fe(II)}_{\text{str}}$  amount were measured by XAFS in order to gain a better understanding of the interface reaction and reduced species. Samples containing Tc retention down to 30 ppm were investigated. The sorption results of each sample are displayed in Table 4.1 and the XAFS spectra are shown in Figure 4.3.

Figure 4.3a shows the Tc K-edge XANES spectra, where the XANES absorption edge

is influenced by the oxidation state and local coordination geometry of Tc. Spectra #2 to #14 encompass samples subjected to various experimental conditions (black solid line). All sample spectra appear to exhibit a similar absorption edge. To further ascertain the specific reduced species, ITFA analysis of these spectra are conducted (Rossberg et al., 2003). First of all, principal component analysis (PCA) is conducted on all sample spectra. The Malinoswki indicator shows one component.  $\text{TcO}_2 \cdot n\text{H}_2\text{O}$ , as the most possible reduced species, is used to reconstruct the experimental spectra, represented by the red solid line. All XANES spectra in Figure 4.3a are well reconstructed with  $\text{TcO}_2 \cdot n\text{H}_2\text{O}$  reference spectrum #1. The white line of XANES spectra is marked with the blue dot line, corresponding to Tc(IV).

Figure 4.3b displays the chi spectra of  $\text{TcO}_2 \cdot n\text{H}_2\text{O}$  reference (#1) and samples (#2-14) within the range of 2 to 12  $\text{\AA}^{-1}$ . It's noticeable that spectra with low Tc loadings appear relatively noisy, while those with high Tc loadings exhibit better quality. Upon comparison, no apparent distinction is discernible between the sample spectra and the  $\text{TcO}_2 \cdot n\text{H}_2\text{O}$  reference spectrum. All chi spectra are well reconstructed using the chi spectrum of  $\text{TcO}_2 \cdot n\text{H}_2\text{O}$  reference #1, although some spectra with low Tc loading displayed significant noise.

Figure 4.3c exhibits the Fourier Transform Magnitude (FTM) of the chi spectra in Figure 4.3b. The first peak at around 1.6  $\text{\AA}$  marked by the blue dot line represents Tc-O interaction, which was also documented by other researchers (Lukens et al., 2002; Oliveira et al., 2022). The second peak at around 2.2  $\text{\AA}$  can be Tc-Tc or Tc-Fe. Back Fourier Transformation (BFT) was carried out the 2<sup>nd</sup> peak for all the samples to check the possible elements. The electron density of Fe and Tc atom is different, hence, the oscillation of the BFT also located at different k. Fe locates at 6 – 8  $\text{\AA}^{-1}$ , while Tc being heavier locates at 10 – 12  $\text{\AA}^{-1}$ . Nevertheless, no Tc-Fe was found in all the samples, even at the lowest Tc loading sample (spectrum #7). The reconstruction of FTM is pretty good, while the reconstruction quality of the low loading samples is not satisfying due to the big noise.

FTM spectra were fitted with Tc-O and Tc-Tc paths in the R range of 1 – 2.7  $\text{\AA}$ . A stable fit of sample spectra of  $\text{TcO}_2 \cdot n\text{H}_2\text{O}$  was obtained in Table 4.1 for all the samples under different conditions. The structure of  $\text{TcO}_2 \cdot n\text{H}_2\text{O}$  was already illustrated that Tc(IV) was octahedrally coordinated with 6 O atoms (Lukens et al., 2002; Oliveira et al., 2022). Therefore, 6 was fixed as coordination number (CN) of Tc-O path in the fitting of the 1<sup>st</sup> peak. The 2<sup>nd</sup> peak was fitted with Tc-Tc path, the fitted CN relatively corresponds to the

size of the reduced species. Samples with low Tc loading present low  $CN_{Tc-Tc}$  (e.g., spectra #2 and #7), which is between monomer and dimer. When the  $CN_{Tc-Tc}$  is around 2, the  $TcO_2 \cdot nH_2O$  precipitates are in chain structure (Oliveira et al., 2022; Yalçintaş et al., 2016b).

Based on the XAFS analysis of sorption isotherm clay samples in Figure 4.2, the Tc retention species is essentially  $TcO_2 \cdot nH_2O$  and no surface complexed (adsorbed) Tc(IV) species is observed even at low Tc loadings.

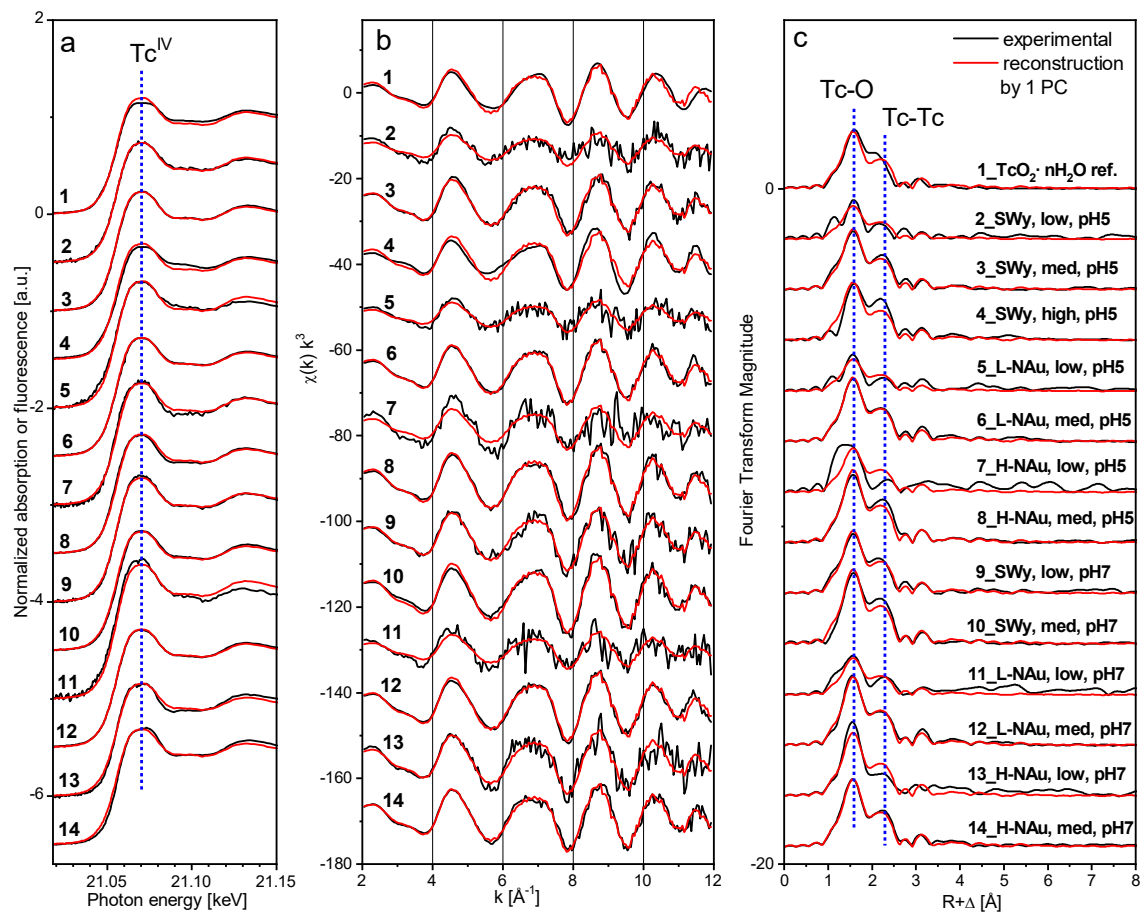


Figure 4.3. Tc K-edge XAFS measurements on red SWy-2, low-red NAu-2, and high-red NAu-2 at S/L of 2 g/L, pH 5 and 7, and 0.1 M NaCl. The samples correspond to the shadowed data in Figure 4.2. The experiment data is in black solid lines, the red solid lines represent the reconstruction of the spectra with one component:  $TcO_2$ , and the blue dot line shows the position of each peak. (a) Normalized Tc absorption edge (XANES), (b)  $k^3$ -weighted EXAFS chi function, (c)  $k^3$ -weighted EXAFS Fourier transform magnitude.

Table 4.1. Tc sorption results and Tc k-edge shell fitting results of the samples in shadows in Figure 4.2.

Sample	Tc retention ppm	Log (Tc <sub>eq</sub> ) mol/L	Log (Tc retention) mol/kg	Path	<sup>a</sup> CN	<sup>b</sup> R [Å]	<sup>c</sup> σ <sup>2</sup> [Å <sup>-2</sup> ]	ΔE <sub>0</sub> [eV]	<sup>d</sup> S <sub>0</sub> <sup>2</sup>	χ <sub>Res</sub>
pH=5										
2_Red SWy-2, low	36	-5.08	-3.38	Tc-O	6	2.05	0.0100	9.6	0.8	18.3
				Tc-Tc	0.86	2.56	0.0057			
3_Red SWy-2, med	292	-4.64	-2.54	Tc-O	6	2.01	0.0044	7.9	0.8	6.5
				Tc-Tc	1.60	2.57	0.0033			
4_Red SWy-2, high	15318	-2.54	-0.81	Tc-O	6	2.01	0.0039	1.9	0.8	11.4
				Tc-Tc	1.92	2.56	0.0030			
5_Low-red NAu-2, low	130	-4.56	-2.86	Tc-O	6	2.05	0.0100	9.6	0.8	18.5
				Tc-Tc	1.76	2.58	0.0100			
6_Low-red NAu-2, med	800	-4.13	-2.10	Tc-O	6	2.02	0.0034	7.9	0.8	6.8
				Tc-Tc	1.34	2.58	0.0021			
7_High-red NAu-2, low	30	-6.67	-3.55	Tc-O	6	2.00	0.0058	6.5	0.8	21.3
				Tc-Tc	0.5	2.57	0.0010			
8_High-red NAu-2, med	310	-5.51	-2.50	Tc-O	6	2.01	0.0028	7.6	0.8	5.2
				Tc-Tc	1.39	2.57	0.0010			
pH=7										
9_Red SWy-2, low	60	-5.77	-3.22	Tc-O	6	2.01	0.0039	6.2	0.8	10.8
				Tc-Tc	2.52	2.58	0.0056			
10_Red SWy-2, med	308	-4.65	-2.43	Tc-O	6	2.02	0.0022	7.1	0.8	5.7
				Tc-Tc	2.19	2.58	0.0031			
11_Low-red NAu-2, low	35	-5.66	-3.46	Tc-O	6	2.03	0.0085	8.3	0.8	9.2
				Tc-Tc	2.14	2.60	0.0090			
12_Low-red NAu-2, med	1400	-4.22	-1.82	Tc-O	6	2.01	0.0025	7.6	0.8	5.8
				Tc-Tc	1.34	2.58	0.0018			
13_High-red NAu-2, low	88	-8.73	-3.05	Tc-O	6	2.02	0.0025	7.9	0.8	7.1
				Tc-Tc	1.32	2.57	0.0048			
14_High-red NAu-2, med	352	-8.18	-2.45	Tc-O	6	2.01	0.0031	7.3	0.8	5.5
				Tc-Tc	1.17	2.56	0.0013			

a: Error of coordination number (CN) ± 25%. The CN of Tc-O is fixed to 6 according to the structure of TcO<sub>2</sub>·nH<sub>2</sub>O.  
b: Error of radial distance (R) ± 0.01 Å.  
c: Error of Debye-Waller factor (σ<sup>2</sup>) ± 0.002 Å.  
d: S<sub>0</sub><sup>2</sup> fixed to 0.8.

4.3.4 Tc retention by Fe(II) species

The retention species TcO<sub>2</sub>·nH<sub>2</sub>O indicates that TcO<sub>4</sub><sup>-</sup> is retarded on the reduced clay minerals by being reduced to Tc(IV). Due to the low solubility of Tc(IV) around 10<sup>-8</sup> M (Yalçintaş et al., 2016c), it precipitates as TcO<sub>2</sub>·nH<sub>2</sub>O solids and thus results in retardation. This Tc reductive precipitation retention mechanism was also reported by previous works (Bishop et al., 2011; Jaisi et al., 2009; Peretyazhko et al., 2008b).

Fe(II)<sub>str</sub> in the reduced clay minerals as an electron donor plays a significant role in Tc retention. The presence of Fe(II)<sub>str</sub> generates a reducing potential within the clay minerals (Gorski et al., 2013). Researchers have identified Fe(II)-O-Fe(III) linkages as pathways for electron transfer in clay minerals (Ilgen et al., 2019; Williams and Scherer, 2004; Yu et al., 2023; Yuan et al., 2018). Consequently, the reducing potential and electron transfer pathways in the reduced clay minerals provide a solid basis for TcO<sub>4</sub><sup>-</sup> reduction and thus result in retention. Figure 4.4 shows the Eh-pH diagram of Tc-O-H system under the initial

Tc concentration of  $1 \times 10^{-7}$  M between pH 2 and 14.  $\text{Tc(VII)O}_4^-$  exists at higher potential, while  $\text{Tc(IV)}$  including  $\text{TcO}_2(\text{OH})_2^{2+}$ ,  $\text{TcO}(\text{OH})_2$ , and  $\text{Tc}(\text{OH})_3^-$  exists at lower potential. The redox potentials of the reduced clay minerals are positioned within the  $\text{TcO}(\text{OH})_2$  region of the Eh-pH diagram of Tc. These positions signify that all four reduced clay minerals have the capacity to initiate the reduction of  $\text{TcO}_4^-$ .

Upon meeting the threshold potential for the reduction of  $\text{TcO}_4^-$ , the extent of the redox reaction becomes heavily reliant on the transferred electron quantity. Notably, the lowest  $\text{Fe(II)}_{\text{str}}$  content at 0.6 wt%, corresponding to  $2 \times 10^{-4}$  M, can provide several orders of magnitude greater number of electrons than needed for the complete reduction of all  $\text{Tc(VII)}$  ( $1 \times 10^{-7}$  M) to  $\text{Tc(IV)}$  in the sorption edge experiment. Hence, the reduction saturation of  $\text{TcO}_4^-$  will not be reached in these sorption edge experiments in Figure 4.1. Tc retention increases as the  $\text{Fe(II)}_{\text{str}}$  content increases and can be normalized to the same Tc retention value by the  $\text{Fe(II)}_{\text{str}}$  content in each clay, therefore, the  $\text{Fe(II)}_{\text{str}}$  content appears as the primary determinant influencing variations in Tc retention under the experimental condition of Figure 4.1.

The  $\text{Fe(II)}_{\text{str}}$  content also significantly influences Tc retention at Tc equilibrium concentration  $> 10^{-5.5}$  M in Figure 4.2a.  $\text{Fe(II)}_{\text{str}}$  content is directly proportional to the number of electrons available for reducing  $\text{Tc(VII)}$  from the clay minerals. Therefore, the behavior of Tc retention on different clay samples is evident: red STx-1, with the lowest  $\text{Fe(II)}_{\text{str}}$  content, possesses fewer electrons and consequently reaches a plateau at the lowest Tc concentration. Subsequently, red SWy-2 and low-red NAu-2, having a moderate amount of  $\text{Fe(II)}_{\text{str}}$  content, plateau at higher Tc concentrations compared with red STx-1. In contrast, high-red NAu-2, with the highest  $\text{Fe(II)}_{\text{str}}$  content, exhibits greater Tc retardation, resulting potentially in the formation of  $\text{Tc(IV)}$  clusters characterized by high Tc retention amount and low equilibrium Tc concentration. Therefore, at elevated Tc concentrations ( $> 10^{-5.5}$  M) under pH 5, the retention of Tc exhibits a direct correlation with  $\text{Fe(II)}_{\text{str}}$  content.

Regarding the impact of  $\text{Fe(II)}_{\text{ad}}$  on the rise in Tc retention observed between pH 6.5 and 7.5 in Figure 4.1,  $\text{Fe(II)}_{\text{ad}}$  adsorbed on the clay mineral surface not only serves as electron donor to reduce  $\text{TcO}_4^-$  but also facilitates the electron transfer as  $\text{Fe(II)/Fe(III)}$  redox couple between Fe in the clay structure and  $\text{TcO}_4^-$  in proximity to the clay mineral surface (Williams and Scherer, 2004). This increase in Tc retention attributed to  $\text{Fe(II)}_{\text{ad}}$  is also depicted in Figure 4.2b, where the Tc retention of high-red NAu-2 is notably higher compared to that at pH 5, observed at the same Tc equilibrium concentration.

Concerning the presence of dissolved  $\text{Fe}^{2+}_{\text{aq}}$  in the clay suspension, despite the thermodynamic feasibility of the homogeneous reduction of  $\text{TcO}_4^-$  by  $\text{Fe}^{2+}_{\text{aq}}$ , previous study demonstrated kinetic hindrance (Cui and Eriksen, 1996a; Zachara et al., 2007). Additionally, among the three Fe(II) species considered,  $\text{Fe}^{2+}_{\text{aq}}$  exhibits the lowest reactivity (Jaisi et al., 2008a). Given that the retention in this study reaches equilibrium relatively quickly, in less than 50 hours (Yang et al., 2012), it seems improbable that homogeneous reduction of  $\text{TcO}_4^-$  by  $\text{Fe}^{2+}_{\text{aq}}$  occurred here. Reported possibilities entail  $\text{Fe}^{2+}_{\text{aq}}$  forming solid phases like iron hydroxides in alkaline condition, leading to heterogeneous reduction on the solid phase (Zachara et al., 2007). However, in this study, no secondary iron phases were detected in the clay suspension without  $\text{CO}_2$  and  $\text{O}_2$  (Qian et al., 2023), thereby ruling out the likelihood of  $\text{TcO}_4^-$  reduction by  $\text{Fe}^{2+}_{\text{aq}}$ . Therefore, the retention of Tc by dissolved  $\text{Fe}^{2+}_{\text{aq}}$  can be excluded in this study.

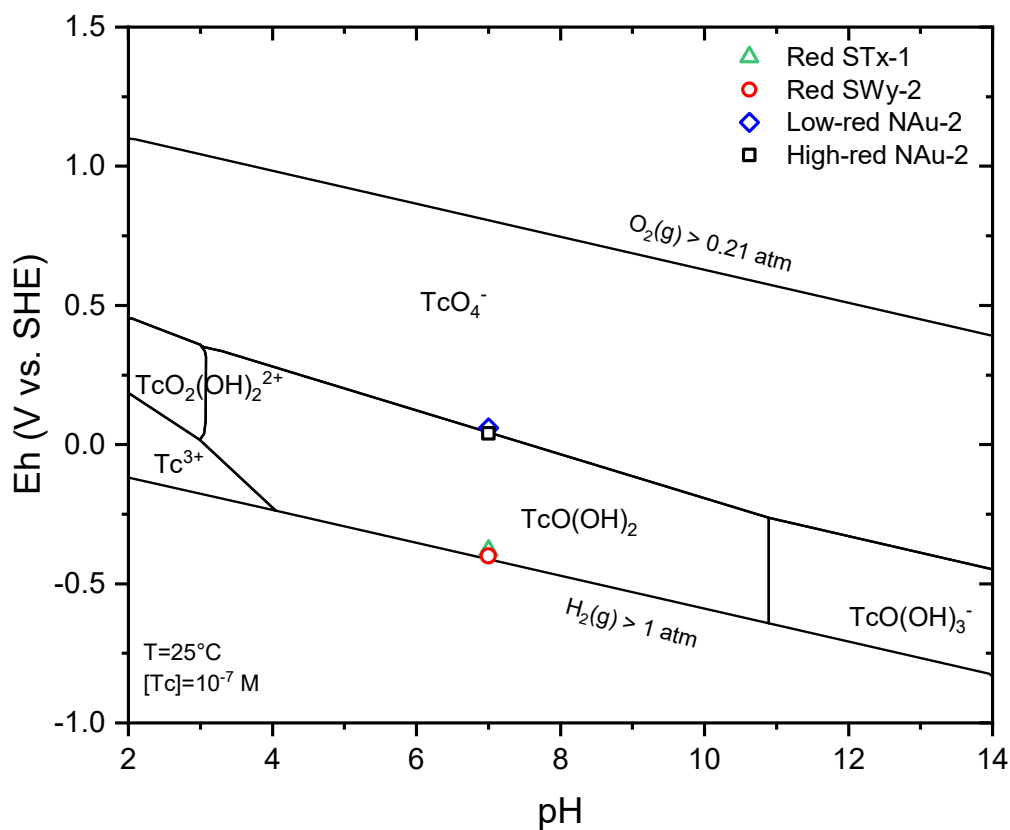


Figure 4.4. Eh-pH diagram of Tc-O-H system at 25°C,  $[\text{Tc}]=1\times10^{-7}$  M, plotted by PhreePlot using PSI Chemical Thermodynamic Database 2020 (W. Hummel, 2023). The redox potentials of reduced clays (green triangle: red STx-1, red circle: red SWy-2, blue diamond: low-red NAu-2, black square: high-red NAu-2) were measured by MEO/MER at pH 7. The MEO/MER measurements were displayed in Chapter 3.3.6.

#### 4.3.5 Tc(VII) reduction products

TcO<sub>2</sub>·nH<sub>2</sub>O reductive precipitation has been extensively documented (Jaisi et al., 2009; Peretyazhko et al., 2008a; Peretyazhko et al., 2008b; Peretyazhko et al., 2012; Zachara et al., 2007). Alongside the reduced species TcO<sub>2</sub>·nH<sub>2</sub>O, Tc(IV) has also been reported to adsorb (Tc-Fe pairs) onto iron minerals such as chukanovite, goethite, hematite, ferrihydrite, and magnetite, and even integrate into their structural composition (Heald et al., 2007; Saslow et al., 2017; Schmeide et al., 2021; Um et al., 2011; Yalçıntaş et al., 2016b). Nevertheless, in this study, no discernible Tc-Fe peak could be observed or fitted. Additionally, only one component was extracted in the PCA analysis, and no trace of Fe was found in the back Fourier transform. Therefore, it is evident that TcO<sub>2</sub>·nH<sub>2</sub>O was predominantly the only reduced species observed in this study, irrespective of the varied experimental conditions.

Quantifiable retention of Tc is observed on all the reduced clay minerals in the pH range < 8. Although clay minerals have permanent negative charge (Brigatti et al., 2013; Chorom and Rengasamy, 1995), the edge sites remain positively charged in this pH range due to protonation and might allow Tc to approach the edge sites closely enough to enable electron transfer from the sorbed/structural Fe(II) to Tc(VII) without undergoing bonding. When Tc(VII) is reduced to Tc(IV), which has a low solubility of around 10<sup>-8</sup> M, Tc(IV) precipitates as TcO<sub>2</sub>·nH<sub>2</sub>O.

TEM was utilized to investigate the morphology of the reduced Tc species at a nanoscale. Figure 4.5a presents the TEM image of the Tc-retained high-red NAu-2 sample captured in dark field mode. The image reveals variously sized particles in bright areas. Comprehensive EDX analysis was performed on the entire image to discern the chemical composition of these particles, encompassing Tc, Si, Fe, and Al. The intensities of these elements are visually represented by the height of the peaks in Figure 4.5f, while their distribution is depicted in Figures 4.5b-4.5e. Si, Fe, and Al correspond to the constituents of high-red NAu-2 clay particles. The biggest discrete Tc particles were identified approximately 10 nm in size (Figure 4.5b), corresponding to the Tc(IV) precipitation clusters observed in Figure 4.2a. This measured clay sample demonstrates the highest quantity of retained Tc, as indicated in Figure 4.2a, yet barely manifests the Tc peak in Figure 4.5f. Instances where Tc retention falls below this level will likely be below the detection limit of EDX. Upon examining the distribution of Tc and high-red NAu-2, no direct correlation between Tc and Fe was observed.

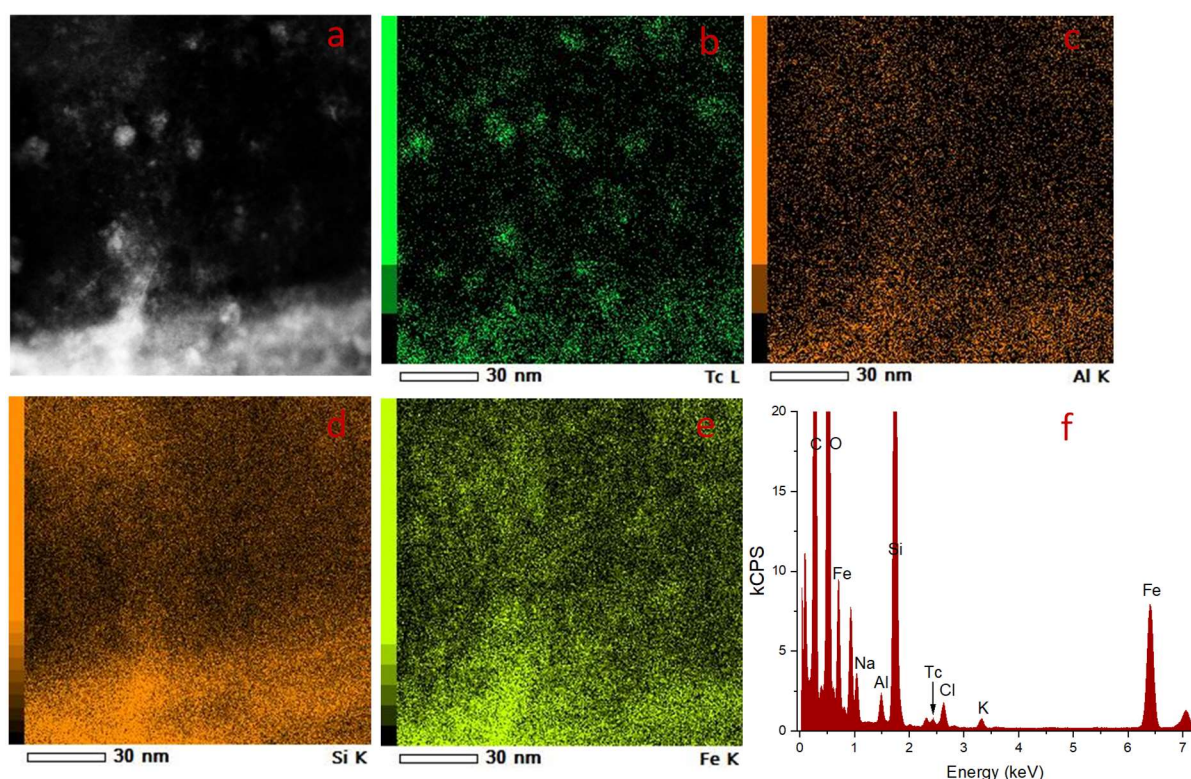


Figure 4.5. TEM image of Tc retention (0.158 mol/kg) on high-red NAu-2, corresponding to the samples encircled by the red dotted line in Figure 4.2a. (a) TEM image captured in dark field mode. (b)-(e) The spatial distribution of Tc, Al, Si, and Fe elements analyzed through EDX analysis of the entire TEM image mentioned in (a). The intensity of the dots corresponds to the concentration of each element. (f) The counts obtained for each element through EDX analysis on the TEM image in (a).

#### 4.3.6 Electron transfer in Tc retention by Fe(II) clay minerals

Tc(VII) does not adsorb onto the native clay mineral from pH 3 to 9, indicating the absence of Tc surface complex at the edge sites. The reduced clay minerals retard Tc(VII) by reductive precipitation process. However, EXAFS measurements reveal no surface adsorbed Tc species (no Fe backscattering contribution). Therefore, the underlying mechanism of electron transfer between structural/adsorbed Fe and Tc in this redox retention process is not clear. One hypothesis considers a possibility of electron transfer between outer-sphere complex and mineral surface. This assumption aligns with the Marcus theory of outer-sphere electron transfer reactions (Marcus, 1956; Marcus and Sutin, 1985). However, the details of electron transfer pathway remain unclear. Future studies on the electron transfer pathway are necessary, for instance, calculation of electron transfer rate by density functional theory (Rosso and Rustad, 2000; Rosso and Morgan, 2002) or experimental investigation using high-speed channel electrode (Clegg et al., 2004).



Moreover, Charlet et al. proposed that electrons generated from the oxidation of adsorbed Fe(II) may be stored in surface  $H_2$  species (Charlet et al., 2007). Additionally,  $TcO_4^-$  exists in a hydrated form where oxygen atoms establish hydrogen bonds with water molecules (Ustynyuk et al., 2021), and the reduced species  $TcO_2 \cdot nH_2O$  is also hydrated. It has been reported that anions can construct hydrogen bond with the surface of clay minerals (Li et al., 2016) and a hydrogen bond conducts electrons more effectively than a covalent bond (Nishino et al., 2013). Consequently, water molecules could possibly serve as the medium for electron transfer between the clay and hydrated  $TcO_4^-$ . Future studies could concentrate on in-situ experiments incorporating Fe isotope labeling into the clay mineral. This would enable a thorough and quantifiable tracking of the transition between Fe(II) and Fe(III), thereby shedding light on the electron transfer mechanism.

#### 4.4 Conclusion and outlook

We conducted a systematic investigation of Tc retention by Fe(II)/Fe(III)-bearing clay minerals with varying structural Fe(II) content and redox potential, in a wide range of pH and  $TcO_4^-$  concentrations. We observed Tc retention exclusively on reduced clay minerals, signifying that the redox potential governed by Fe(II) within the clays acts as the driving force behind Tc retention. Moreover, Tc retention between pH 3 and 8 exhibited a direct correlation with the structural Fe(II) content in the clay minerals. At low  $TcO_4^-$  concentration  $< 10^{-5.5}$  M, we observed consistent Tc retention behavior. However, at higher  $TcO_4^-$  concentration  $> 10^{-5.5}$  M, distinct retention behaviors emerged, namely nucleation-like precipitation, retardation, or saturation. Our investigations identified  $TcO_2 \cdot nH_2O$  as the sole reduced species, as no evidence of Tc-Fe pairs were detected, leaving the interfacial interaction and electron transfer mechanism in the Tc(VII) reduction process unclear. We hypothesize that an outer-sphere electron transfer mechanism is responsible for the Tc retention process. Future studies on Tc retention could employ Fe isotope-labeled clay minerals to gain a more comprehensive understanding of electron transfer via Fe atoms. Additionally, spectroscopic techniques sensitive to changes in hydrogen bonds, such as Fourier Transform Infrared Spectroscopy (FTIR), can be utilized to investigate the interfacial reactions between clay minerals and  $TcO_4^-$  anions.

The Tc retention parameters examined in this study are of high relevance for the Tc geochemistry. The findings affirm the efficacy of Tc retention by Fe-bearing clay minerals, resulting in the formation of insoluble  $TcO_2 \cdot nH_2O$  precipitates. Additionally, they furnish

essential data for thermodynamic calculations and models pertaining to Tc chemistry. These results make a substantial contribution to enhancing the safety assessment of deep geological repositories, providing substantial support to radioactive waste management efforts, as well as informing the development of remediation strategies for Tc-contaminated sites.

## **Acknowledgment**

This work was supported by European Union's Horizon 2020 research and innovation program under grant agreement No 847593. We thank Astrid Schaible and Andreas Laube for their technical support in the laboratory. We also extend our thanks to the ESRF and the Helmholtz Zentrum Dresden Rossendorf beamline (ROBL) for facilitating the EXAFS measurements.

## 4.5 Reference

- Bishop M. E., Dong H., Kukkadapu R. K., Liu C. and Edelman R. E. (2011) Bioreduction of Fe-bearing clay minerals and their reactivity toward pertechnetate (Tc-99). *Geochimica et Cosmochimica Acta* **75**, 5229-5246.
- Bradbury M. H. and Baeyens B. (2002) Sorption of Eu on Na- and Ca-montmorillonites: experimental investigations and modelling with cation exchange and surface complexation. *Geochimica et Cosmochimica Acta* **66**, 2325-2334.
- Brigatti M. F., Galán E. and Theng B. K. G. (2013) Chapter 2 - Structure and Mineralogy of Clay Minerals. In *Developments in Clay Science* (eds. F. Bergaya and G. Lagaly). Elsevier. pp. 21-81.
- Burke I. T., Boothman C., Lloyd J. R., Mortimer R. J. G., Livens F. R. and Morris K. (2005) Effects of Progressive Anoxia on the Solubility of Technetium in Sediments. *Environmental Science & Technology* **39**, 4109-4116.
- Burke I. T., Boothman C., Lloyd J. R., Livens F. R., Charnock J. M., McBeth J. M., Mortimer R. J. G. and Morris K. (2006) Reoxidation Behavior of Technetium, Iron, and Sulfur in Estuarine Sediments. *Environmental Science & Technology* **40**, 3529-3535.
- Charlet L., Scheinost A. C., Tournassat C., Greneche J.-M., GÉhin A., Fernandez-Martinez A., Coudert S., Tisserand D. and Brendle J. (2007) Electron transfer at the mineral/water interface: Selenium reduction by ferrous iron sorbed on clay. *Geochimica et Cosmochimica Acta* **71**, 5731-5749.
- Childs B. C., Lawler K. V., Braband H., Mast D. S., Bigler L., Stalder U., Peterson D. R., Jansen A., Forster P. M., Czerwinski K. R., Alberto R., Sattelberger A. P. and Poineau F. (2018) The Nature of the Technetium Species Formed During the Oxidation of Technetium Dioxide with Oxygen and Water. *European Journal of Inorganic Chemistry* **2018**, 1137-1144.
- Chorom M. and Rengasamy P. (1995) Dispersion and zeta potential of pure clays as related to net particle charge under varying pH, electrolyte concentration and cation type. *European Journal of Soil Science* **46**, 657-665.
- Clegg A. D., Rees N. V., Klymenko O. V., Coles B. A. and Compton R. G. (2004) Marcus Theory of Outer-Sphere Heterogeneous Electron Transfer Reactions: Dependence of the Standard Electrochemical Rate Constant on the Hydrodynamic Radius from High Precision Measurements of the Oxidation of Anthracene and Its Derivatives in Nonaqueous Solvents Using the High-Speed Channel Electrode. *Journal of the American Chemical Society* **126**, 6185-6192.
- Cui D. and Eriksen T. E. (1996a) Reduction of Pertechnetate by Ferrous Iron in Solution: Influence of Sorbed and Precipitated Fe(II). *Environmental Science & Technology* **30**, 2259-2262.
- Cui D. and Eriksen T. E. (1996b) Reduction of Pertechnetate in Solution by Heterogeneous

Electron Transfer from Fe(II)-Containing Geological Material. *Environmental Science & Technology* **30**, 2263-2269.

Fredrickson J. K., Zachara J. M., Kennedy D. W., Kukkadapu R. K., McKinley J. P., Heald S. M., Liu C. and Plymale A. E. (2004) Reduction of TcO<sub>4</sub><sup>-</sup> by sediment-associated biogenic Fe(II). *Geochimica et Cosmochimica Acta* **68**, 3171-3187.

Gorski C. A., Klupfel L. E., Voegelin A., Sander M. and Hofstetter T. B. (2013) Redox properties of structural Fe in clay minerals: 3. Relationships between smectite redox and structural properties. *Environ Sci Technol* **47**, 13477-13485.

Heald S. M., Zachara J. M., Jeon B. H., McKinley J. P., Kukkadapu R. and Moore D. (2007) XAFS Study of the Chemical and Structural States of Technetium in Fe(III) Oxide Co - Precipitates. *AIP Conference Proceedings* **882**, 173-175.

Icenhower J. P., Qafoku N. P., Zachara J. M. and Martin W. J. (2010) The biogeochemistry of technetium: a review of the behavior of an artificial element in the natural environment. *American Journal of Science* **310**, 721-752.

Ilgen A. G., Kukkadapu R. K., Leung K. and Washington R. E. (2019) "Switching on" iron in clay minerals. *Environmental Science: Nano* **6**, 1704-1715.

Jaisi D. P., Dong H. and Morton J. P. (2008a) Partitioning of Fe(II) in reduced nontronite (NAu-2) to reactive sites: Reactivity in terms of Tc(VII) reduction. *Clays and Clay Minerals* **56**, 175-189.

Jaisi D. P., Dong H., Plymale A. E., Fredrickson J. K., Zachara J. M., Heald S. and Liu C. (2009) Reduction and long-term immobilization of technetium by Fe(II) associated with clay mineral nontronite. *Chemical Geology* **264**, 127-138.

Li X., Li H. and Yang G. (2016) Configuration, anion-specific effects, diffusion, and impact on counterions for adsorption of salt anions at the interfaces of clay minerals. *The Journal of Physical Chemistry C* **120**, 14621-14630.

Lukens W. W., Bucher J. J., Edelstein N. M. and Shuh D. K. (2002) Products of Pertechnetate Radiolysis in Highly Alkaline Solution: Structure of TcO<sub>2</sub>·xH<sub>2</sub>O. *Environmental Science & Technology* **36**, 1124-1129.

Marcus R. (1956) On the Theory of OxidationReduction Reactions Involving Electron Transfer. I. vol.

Marcus R. A. and Sutin N. (1985) Electron transfers in chemistry and biology. *Biochimica et Biophysica Acta (BBA)-Reviews on Bioenergetics* **811**, 265-322.

McBeth J. M., Lear G., Lloyd J. R., Livens F. R., Morris K. and Burke I. T. (2007) Technetium Reduction and Reoxidation in Aquifer Sediments. *Geomicrobiology Journal* **24**, 189-197.

Muller I. S., McKeown D. A. and Pegg I. L. (2014) Structural Behavior of Tc and I Ions in Nuclear Waste Glass. *Procedia Materials Science* **7**, 53-59.

- Newsome L., Morris K. and Lloyd J. R. (2014) The biogeochemistry and bioremediation of uranium and other priority radionuclides. *Chemical Geology* **363**, 164-184.
- Nishino T., Hayashi N. and Bui P. T. (2013) Direct Measurement of Electron Transfer through a Hydrogen Bond between Single Molecules. *Journal of the American Chemical Society* **135**, 4592-4595.
- Oliveira A. F., Kuc A., Heine T., Abram U. and Scheinost A. C. (2022) Shedding Light on the Enigmatic  $\text{TcO}_2 \cdot x\text{H}_2\text{O}$  Structure with Density Functional Theory and EXAFS Spectroscopy\*\*. *Chemistry – A European Journal* **28**, e202202235.
- Omori T., Asahina K. and Suganuma H. (1995) Mechanism of the solvent extraction of pertechnetate with tetraphenylarsonium chloride. *Journal of Radioanalytical and Nuclear Chemistry* **191**, 99-104.
- Pearce C. I., Moore R. C., Morad J. W., Asmussen R. M., Chatterjee S., Lawter A. R., Levitskaia T. G., Neeway J. J., Qafoku N. P., Rigali M. J., Saslow S. A., Szecsody J. E., Thallapally P. K., Wang G. and Freedman V. L. (2020) Technetium immobilization by materials through sorption and redox-driven processes: A literature review. *Science of The Total Environment* **716**, 132849.
- Peretyazhko T., Zachara J. M., Heald S. M., Kukkadapu R. K., Liu C., Plymale A. E. and Resch C. T. (2008a) Reduction of Tc(VII) by Fe(II) Sorbed on Al (hydr)oxides. *Environmental Science & Technology* **42**, 5499-5506.
- Peretyazhko T., Zachara J. M., Heald S. M., Jeon B. H., Kukkadapu R. K., Liu C., Moore D. and Resch C. T. (2008b) Heterogeneous reduction of Tc(VII) by Fe(II) at the solid–water interface. *Geochimica et Cosmochimica Acta* **72**, 1521-1539.
- Peretyazhko T. S., Zachara J. M., Kukkadapu R. K., Heald S. M., Kutnyakov I. V., Resch C. T., Arey B. W., Wang C. M., Kovarik L., Phillips J. L. and Moore D. A. (2012) Pertechnetate ( $\text{TcO}_4^-$ ) reduction by reactive ferrous iron forms in naturally anoxic, redox transition zone sediments from the Hanford Site, USA. *Geochimica et Cosmochimica Acta* **92**, 48-66.
- Poineau F., Mausolf E., Jarvinen G. D., Sattelberger A. P. and Czerwinski K. R. (2013) Technetium Chemistry in the Fuel Cycle: Combining Basic and Applied Studies. *Inorganic Chemistry* **52**, 3573-3578.
- Qian Y., Scheinost A. C., Grangeon S., Greneche J.-M., Hoving A., Bourhis E., Maubec N., Churakov S. V. and Fernandes M. M. (2023) Oxidation State and Structure of Fe in Nontronite: From Oxidizing to Reducing Conditions. *ACS Earth and Space Chemistry* **7**, 1868-1881.
- Ressler T. (1998) WinXAS: A program for X-ray absorption spectroscopy data analysis under MS-Windows. *Journal of Synchrotron Radiation* **5**, 118-122.
- Rossberg A., Reich T. and Bernhard G. (2003) Complexation of uranium (VI) with protocatechuic acid—application of iterative transformation factor analysis to EXAFS spectroscopy. *Analytical and bioanalytical chemistry* **376**, 631-638.

- Rosso K. M. and Rustad J. R. (2000) Ab Initio Calculation of Homogeneous Outer Sphere Electron Transfer Rates: Application to  $M(OH_2)_6^{3+/2+}$  Redox Couples. *The Journal of Physical Chemistry A* **104**, 6718-6725.
- Rosso K. M. and Morgan J. J. (2002) Outer-sphere electron transfer kinetics of metal ion oxidation by molecular oxygen. *Geochimica et Cosmochimica Acta* **66**, 4223-4233.
- Saslow S. A., Um W., Pearce C. I., Engelhard M. H., Bowden M. E., Lukens W., Leavy I. I., Riley B. J., Kim D.-S., Schweiger M. J. and Kruger A. A. (2017) Reduction and Simultaneous Removal of  $^{99}Tc$  and Cr by  $Fe(OH)_2(s)$  Mineral Transformation. *Environmental Science & Technology* **51**, 8635-8642.
- Scheinost A. C., Claussner J., Exner J., Feig M., Findeisen S., Hennig C., Kvashnina K. O., Naudet D., Prieur D., Rossberg A., Schmidt M., Qiu C., Colomp P., Cohen C., Dettona E., Dyadkin V. and Stumpf T. (2021) ROBL-II at ESRF: a synchrotron toolbox for actinide research. *Journal of Synchrotron Radiation* **28**, 333-349.
- Schmeide K., Rossberg A., Bok F., Shams Aldin Azzam S., Weiss S. and Scheinost A. C. (2021) Technetium immobilization by chukanovite and its oxidative transformation products: Neural network analysis of EXAFS spectra. *Science of The Total Environment* **770**, 145334.
- Siegel M. D. and Bryan C. R. (2014) 11.6 - Radioactivity, Geochemistry, and Health. In *Treatise on Geochemistry (Second Edition)* (eds. H. D. Holland and K. K. Turekian). Elsevier, Oxford. pp. 191-256.
- Soltermann D., Baeyens B., Bradbury M. H. and Marques Fernandes M. (2014a) Fe(II) uptake on natural montmorillonites. II. Surface complexation modeling. *Environ Sci Technol* **48**, 8698-8705.
- Soltermann D., Marques Fernandes M., Baeyens B., Dahn R., Joshi P. A., Scheinost A. C. and Gorski C. A. (2014c) Fe(II) uptake on natural montmorillonites. I. Macroscopic and spectroscopic characterization. *Environ Sci Technol* **48**, 8688-8697.
- Stucki J., Golden D. and Roth C. (1984a) Preparation and Handling of Dithionite-Reduced Smectite Suspensions. *Clays and Clay Minerals - CLAYS CLAY MINER* **32**, 191-197.
- Um W., Chang H.-S., Icenhower J. P., Lukens W. W., Serne R. J., Qafoku N. P., Westsik J. H., Jr., Buck E. C. and Smith S. C. (2011) Immobilization of  $^{99}Tc$  by Fe(II)-Goethite and Limited Reoxidation. *Environmental Science & Technology* **45**, 4904-4913.
- Ustynyuk Y. A., Gloriozov I. P., Zhokhova N. I., German K. E. and Kalmykov S. N. (2021) Hydration of the pertechnetate anion. DFT study. *Journal of Molecular Liquids* **342**, 117404.
- W. Hummel T. T. (2023) The PSI chemical thermodynamic database 2020, Nagra Technical Report NTB 21-03, Nagra, Wettingen, Switzerland.
- Webb S. M. (2005) SIXpack: a graphical user interface for XAS analysis using IFEFFIT.

- Wildung R. E., Li S. W., Murray C. J., Krupka K. M., Xie Y., Hess N. J. and Roden E. E. (2004) Technetium reduction in sediments of a shallow aquifer exhibiting dissimilatory iron reduction potential. *FEMS Microbiology Ecology* **49**, 151-162.
- Wildung R. E., Gorby Y. A., Krupka K. M., Hess N. J., Li S., Plymale A. E., McKinley J. P. and Fredrickson J. K. (2000) Effect of electron donor and solution chemistry on products of dissimilatory reduction of technetium by *Shewanella putrefaciens*. *Applied and Environmental Microbiology* **66**, 2451-2460.
- Williams A. G. B. and Scherer M. M. (2004) Spectroscopic Evidence for Fe(II)–Fe(III) Electron Transfer at the Iron Oxide–Water Interface. *Environmental Science & Technology* **38**, 4782-4790.
- Wilmarth W. R., Lumetta G. J., Johnson M. E., Poirier M. R., Thompson M. C., Suggs P. C. and Machara N. P. (2011) Review: Waste-Pretreatment Technologies for Remediation of Legacy Defense Nuclear Wastes. *Solvent Extraction and Ion Exchange* **29**, 1-48.
- Yalçıntaş E., Scheinost A. C., Gaona X. and Altmaier M. (2016b) Systematic XAS study on the reduction and uptake of Tc by magnetite and mackinawite. *Dalton Transactions* **45**, 17874-17885.
- Yalçıntaş E., Gaona X., Altmaier M., Dardenne K., Polly R. and Geckeis H. (2016c) Thermodynamic description of Tc(IV) solubility and hydrolysis in dilute to concentrated NaCl, MgCl<sub>2</sub> and CaCl<sub>2</sub> solutions. *Dalton Transactions* **45**, 8916-8936.
- Yang J., Kukkadapu R. K., Dong H., Shelobolina E. S., Zhang J. and Kim J. (2012) Effects of redox cycling of iron in nontronite on reduction of technetium. *Chemical Geology* **291**, 206-216.
- Yu C., Qian A., Lu Y., Liao W., Zhang P., Tong M., Dong H., Zeng Q. and Yuan S. (2023) Electron transfer processes associated with structural Fe in clay minerals. *Critical Reviews in Environmental Science and Technology* 10.1080/10643389.2023.2221154, 1-26.
- Yu S., Liu Y., Pang H., Tang H., Wang J., Zhang S. and Wang X. (2022) Chapter 1 - Novel nanomaterials for environmental remediation of toxic metal ions and radionuclides. In *Emerging Nanomaterials for Recovery of Toxic and Radioactive Metal Ions from Environmental Media* (ed. X. Wang). Elsevier. pp. 1-47.
- Yuan S., Liu X., Liao W., Zhang P., Wang X. and Tong M. (2018) Mechanisms of electron transfer from structural Fe(II) in reduced nontronite to oxygen for production of hydroxyl radicals. *Geochimica et Cosmochimica Acta* **223**, 422-436.
- Zachara J. M., Heald S. M., Jeon B.-H., Kukkadapu R. K., Liu C., McKinley J. P., Dohnalkova A. C. and Moore D. A. (2007) Reduction of pertechnetate [Tc(VII)] by aqueous Fe(II) and the nature of solid phase redox products. *Geochimica et Cosmochimica Acta* **71**, 2137-2157.

## **Chapter 5: Comparison of the retention of Se and Tc**



Chapter 3 and 4 address the retention of Se and Tc on four reduced clay minerals, respectively. In these two systems, various parameters were studied, including structural Fe(II) content, redox potential, pH, concentration, kinetics, and reduced species. There are many similarities and differences. In this chapter, systematic comparison of the retention of Se and Tc on the four reduced clay minerals will be addressed.

## 5.1 Chemical properties

Both Se and Tc are redox-sensitive elements with oxidation states varying from –II to VI for Se and –I to VII for Tc, respectively. Their oxidized forms are soluble and mobile, whereas their reduced forms are insoluble and immobile, making reduction an effective retention strategy for both elements. In their oxidized states, both Se and Tc exist as oxyanions – selenite ( $\text{Se(IV)O}_3^{2-}$ ) and pertechnetate ( $\text{Tc(VII)O}_4^-$ ). However, selenite is a weak acid that can exist as  $\text{H}_2\text{SeO}_3$ ,  $\text{HSeO}_3^-$ , or  $\text{SeO}_3^{2-}$ , depending upon the pH of solution ( $\text{pK}_{a1} = 2.70$  and  $\text{pK}_{a2} = 8.54$ ) (Fernández-Martínez and Charlet, 2009). Contrary, pertechnetate is a strong acid ( $\text{pK}_a = 0.32$ ) (Omori et al., 1995), predominantly existing as the pertechnetate ion without any hydrolysis form in aqueous solutions. This distinct difference in  $\text{pK}_a$  values imparts varying affinities to these anions in the sorption process.

## 5.2 Retention mechanism

In the sorption edge experiments conducted with the native clay mineral, Se(IV) adsorbs from pH 4 to 8, and the adsorption decreases as the pH increases. This variation in adsorption is attributed to the protonation and deprotonation of hydroxyl groups on the edges of clay mineral with changing pH. EXAFS measurements show backscattering from Fe in the second coordination shell, indicating that Se(IV) adsorption takes place via surface complexes. Contrarily, Tc(VII) does not exhibit adsorption of surface complexation on the native clay mineral throughout the pH range of 4 to 8. The difference in adsorption behavior is likely attributed to the chemical properties of Se and Tc. Se exists in the hydrolyzed form as  $\text{HSeO}_3^-$  within the pH range of 4 to 8, displaying high  $\text{pK}_a$  values, which indicate a strong affinity of proton to selenite. Contrarily, Tc exists as unhydrolyzed  $\text{TcO}_4^-$  in this pH range, characterized by a low  $\text{pK}_a$ , suggesting a weaker affinity of protons to pertechnetate. Consequently, Se adsorbs onto the edge sites of clay minerals, while Tc does not exhibit such adsorption behavior. In summary, distinct adsorption behavior is observed for Se and Tc on the native clay mineral.

Concerning the four distinct reduced clay minerals varying in structural Fe(II) content – red STx-1 (0.5 wt%), red SWy-2 (2.5 wt%), low-red NAu-2 (4.2 wt%), high-red NAu-2 (11.4 wt%), the retention of both Se and Tc is observed in all system. Fe(II) plays a critical role due to its reducing potential, initiating the reduction of Se(VI) and Tc(VII). However, besides Fe(II) being associated with the reducing potential for this reduction, the retention of Se and Tc is also influenced by other factors.

Kinetics is one of the sorption controlling parameters. Se reduction is kinetically controlled and occurs relatively slow up to months (Charlet et al., 2007; Onoguchi et al., 2019; Pearce et al., 2008). Initially, Se(IV) is adsorbed and subsequently undergoes a gradual reduction, transitioning from red Se(0) to amorphous red Se(0) before finally converting into crystalline grey Se(0). The rate of Se(IV) reduction is markedly linked to the Fe(II)<sub>str</sub> content, with higher Fe(II)<sub>str</sub> content resulting in a faster reduction of Se(IV) to red Se(0), hastening the conversion of red Se(0) to grey Se(0). This entire retention process spans from days to several months. Conversely, the reduction of Tc(VII) occurs at a much quicker rate, typically taking about 50 hours (Yang et al., 2012).

Due to the slow kinetics of Se retention, it remains unknown how much time is required to achieve Se sorption equilibrium for low-red NAu-2, red SWy-2, and red STx-1. This is because their sorption equilibrium is not reached within 3600 hours. Consequently, the sorption edge and isotherm of Se are not examined in this study. The Se retention is rapid within the 168 hours and then gradually slows down. Therefore, Se sorption occurs fast, while the consequent steps of selenite reduction and structural conversion of red Se(0) to grey Se(0) proceed slowly. In contrast, owing to the rapid kinetics of Tc retention, the Tc sorption edge and isotherm have been studied after 7 days, ensuring the attainment of equilibrium. The retention of Tc remains relatively constant between pH 4 and 8 as pH increases. Moreover, the Tc retention increases proportionally with the increasing Fe(II)<sub>str</sub> content and can be normalized to a unified value by the amount of Fe(II)<sub>str</sub> in each reduced clay mineral.

In addition to Fe(II)<sub>str</sub> content, Fe<sup>2+</sup><sub>aq</sub> play an important role in the retention process. Fe<sup>2+</sup><sub>aq</sub> is present in the clay suspension due to partial clay dissolution. In both sorption experiments of Se and Tc, no reduced Se or Tc species are formed directly from homogeneous interaction with Fe<sup>2+</sup><sub>aq</sub>. This observation is reasonable because Fe<sup>2+</sup><sub>aq</sub> has low reactivity compared to Fe(II)<sub>str</sub> and Fe<sup>2+</sup><sub>aq</sub> adsorbed on a mineral phase (Jaisi et al., 2008a). Thermodynamically feasible homogeneous reaction between Fe<sup>2+</sup><sub>aq</sub> and Se or Tc is

kinetically hindered (Cui and Eriksen, 1996a). According to previous studies,  $\text{Fe}^{2+}_{\text{aq}}$  can be adsorbed to the reduced clay mineral surface ( $\text{Fe(II)}_{\text{ad}}$ ) depending on the pH of the solution. The sorption increases from pH of 4 to 7 and reaches maximum around pH 7 (Jaisi et al., 2008a; Soltermann et al., 2014a). The role of  $\text{Fe(II)}_{\text{ad}}$  is not apparent in the current experiments of Se retention, but is prominent in the case of Tc retention around pH 7. High-red NAu-2 characterized by high  $\text{Fe}^{2+}_{\text{aq}}$  demonstrates significantly greater Tc retention at pH 7 compared to other pH values. Conversely, other reduced clay minerals, like low-red NAu-2, red SWy-2, and red STx-1, having low  $\text{Fe}^{2+}_{\text{aq}}$ , do not exhibit increase in Tc retention due to the absence of  $\text{Fe(II)}_{\text{ad}}$ .

Regarding the reduced species,  $\text{Se(IV)}$  undergoes an initial reduction to form amorphous red  $\text{Se(0)}$ , which gradually transitions into crystalline grey  $\text{Se(0)}$ . Throughout the Se sorption kinetics experiments under different  $\text{Fe(II)}_{\text{str}}$  content and  $\text{Fe}^{2+}_{\text{aq}}$  concentration, neither  $\text{FeSe}_2$  or  $\text{FeSe}$  is detected. Under the same condition,  $\text{Tc(VII)}$  is reduced to  $\text{Tc(IV)}$  after reaching equilibrium. Regardless of the different  $\text{Fe(II)}_{\text{str}}$  content, redox potential, pH, and Tc concentration,  $\text{TcO}_2 \cdot n\text{H}_2\text{O}$  is the only reduction product, no Tc-Fe pairs are detected even under very low Tc loading (35 ppm). Overall, in the retention process, both Se and Tc undergo reduction to a lower oxidation state, leading to their precipitation as solid phases due to the low solubility of their reduced species, thereby immobilizing these elements.

Concerning the electron transfer in the retention process, Se and Tc display different mechanisms.  $\text{Se(IV)}$  is initially adsorbed onto the reduced clay minerals as inner-sphere surface complexes, forming a Se-Fe pair. Consequently, electrons can be transferred via an inner-sphere mechanism. Contrarily,  $\text{Tc(VII)}$  does not adsorb onto the surface of reduced clay minerals, implying that reduction is likely to occur through an outer-sphere electron transfer mechanism (Marcus, 1956; Marcus and Sutin, 1985).

Many parameters affect the retention of Se and Tc, making it challenging to determine a dominant factor.  $\text{Fe(II)}_{\text{str}}$  content at pH 5 is the prevailing factor in Se retention in the kinetics experiments, while the redox potential becomes the controlling factor at pH 7. When reduced clay minerals reach the redox potential threshold for  $\text{Se(IV)}$  reduction at pH 5, progress of retention is by the amount of transferred electrons, which correlates with  $\text{Fe(II)}_{\text{str}}$  content. However, at pH 7, a lower reduction potential is required to reduce  $\text{Se(IV)}$ , thus the redox potentials of clay minerals control the kinetic experiments. As the same samples are used in the study of Tc retention, the redox potential of the reduced clay minerals is identical

to that of the Se retention system. However, the redox potential does not limit Tc retention neither at pH 5 nor 7, despite just meeting the threshold of Tc(VII) reduction at pH 7. Although differences can be observed through retention experiments, a comprehensive understanding of the reductive sorption mechanism of these elements needs further studies.

### 5.3 Reference

- Charlet L., Scheinost A. C., Tournassat C., Greneche J.-M., G  hin A., Fernandez-Martinez A., Coudert S., Tisserand D. and Brendle J. (2007) Electron transfer at the mineral/water interface: Selenium reduction by ferrous iron sorbed on clay. *Geochimica et Cosmochimica Acta* **71**, 5731–5749.
- Cui D. and Eriksen T. E. (1996a) Reduction of Pertechnetate by Ferrous Iron in Solution: Influence of Sorbed and Precipitated Fe(II). *Environmental Science & Technology* **30**, 2259-2262.
- Fern  ndez-Mart  nez A. and Charlet L. (2009) Selenium environmental cycling and bioavailability: a structural chemist point of view. *Reviews in Environmental Science and Bio/Technology* **8**, 81-110.
- Jaisi D. P., Dong H. and Morton J. P. (2008a) Partitioning of Fe(II) in reduced nontronite (NAu-2) to reactive sites: Reactivity in terms of Tc(VII) reduction. *Clays and Clay Minerals* **56**, 175-189.
- Marcus R. (1956) On the Theory of OxidationReduction Reactions Involving Electron Transfer. I. vol.
- Marcus R. A. and Sutin N. (1985) Electron transfers in chemistry and biology. *Biochimica et Biophysica Acta (BBA)-Reviews on Bioenergetics* **811**, 265-322.
- Omori T., Asahina K. and Suganuma H. (1995) Mechanism of the solvent extraction of pertechnetate with tetraphenylarsonium chloride. *Journal of Radioanalytical and Nuclear Chemistry* **191**, 99-104.
- Onoguchi A., Granata G., Haraguchi D., Hayashi H. and Tokoro C. (2019) Kinetics and mechanism of selenate and selenite removal in solution by green rust-sulfate. *Royal Society Open Science* **6**, 182147.
- Pearce C. I., Coker V. S., Charnock J. M., Patrick R. A. D., Mosselmans J. F. W., Law N., Beveridge T. J. and Lloyd J. R. (2008) Microbial manufacture of chalcogenide-based nanoparticles via the reduction of selenite using *Veillonella atypica*: an in situ EXAFS study. *Nanotechnology* **19**, 155603.
- Soltermann D., Baeyens B., Bradbury M. H. and Marques Fernandes M. (2014a) Fe(II) uptake on natural montmorillonites. II. Surface complexation modeling. *Environ Sci Technol* **48**, 8698-8705.
- Yang J., Kukkadapu R. K., Dong H., Shelobolina E. S., Zhang J. and Kim J. (2012) Effects of redox cycling of iron in nontronite on reduction of technetium. *Chemical Geology* **291**, 206-216.

## **Chapter 6: Conclusions and outlook**

## 6.1 Conclusions

In this thesis, the retention of Se and Tc on Fe(II)/Fe(III)-bearing clay minerals has been investigated. The goal is to reveal the mechanism of coupled adsorption and the redox interface reactions in the retention process using macroscopic sorption experiments and molecular scale spectroscopic measurements. The focus is on the role of Fe in the clay minerals, where Fe(II)/Fe(III) and its associated redox potential serve as the driving force behind the retention process. The experimental results demonstrate the role of Fe(II)/Fe(III)-bearing clay minerals in retarding the anions of Se and Tc by converting the oxidized and mobile anions into reduced and insoluble precipitates, and thus highlight the importance of clay minerals as the engineered backfill materials in ensuring the secure disposal of HLW in the deep geological repositories.

Initially, Fe(II)/Fe(III)-bearing clay minerals were prepared through chemical reduction of native clay minerals to varying degrees, resulting in different Fe(II) content levels of 0.6 wt%, 2.5 wt%, 4.2 wt%, and 11.4 wt%. Subsequently, the reduced clay minerals underwent characterization to assess the impact of reduction on their structure. The clay dissolution, structure, and morphology were examined using XRD and TEM. Through this reduction method, the reduced clay minerals retained their layered structure over long ranges. Only minor dissolution was observed on the external basal plane of the clay particles, and no secondary iron phases were identified in the treated reduced clay suspension. The local structure of Fe in the clay mineral was probed using Mössbauer spectrometry, XPS, XANES, EXAFS, and MEO/MER techniques. These analyses indicated an increase in structural disorder and Fe clustering with increasing reduction of structural Fe, likely linked to the variations in redox potential at different reduction levels. The cation exchange capacity and the availability of sorption edge sites were examined by comparing the sorption behavior between native and reduced clay minerals, revealing negligible differences. Consequently, no substantial alterations were detected in the structure of the reduced clay minerals, providing a foundation for the subsequent investigation of Se and Tc retention on these reduced clay minerals.

In studying the retention of Se, kinetics experiments of selenite were conducted on the reduced clay minerals at an initial selenite concentration of  $3 \times 10^{-5}$  M, a solid-liquid ratio of 2 g/L, pH levels of 5 and 7, and an electrolyte of 0.1 M NaCl, spanning a period of up to 5 months. The impact of structural Fe(II) content was specifically examined at pH 5. Through sorption experiments, the adsorption of selenite was observed, and inner-sphere surface

complexes were identified using EXAFS measurements. This indicates that selenite retention involves an initial adsorption step followed by reductive precipitation. The reduction rate of selenite was found to increase with higher structural Fe(II) content. Two forms of reduced selenium, red Se(0) and grey Se(0), were observed, while no FeSe or FeSe<sub>2</sub> species were detected under the experimental conditions. Initially, amorphous red Se(0) appeared as the reduction product, gradually transitioning to crystalline grey Se(0) over time as it represents the thermodynamically more stable phase. This transformation occurred at a faster rate when the structural Fe(II) content was higher. At pH 5, given sufficient redox potential in the clay minerals to initiate selenite reduction, the structural Fe(II) content, corresponding to the quantity of electron donor, emerged as the controlling factor. On the other hand, at pH 7, the reduction potential required to reduce selenite was lower than that at pH 5, making the redox potential of the clay minerals the dominant factor in retention. Despite a slower selenite reduction rate, the reaction still progressed over an extended period, yielding the same reduced species as observed at pH 5. In summary, this study examined four key parameters: structural Fe(II) content, redox potential, pH, and reaction time. The controlling parameter in selenite reduction varied depending on the specific experimental conditions.

To investigate the retention of Tc, the same samples were utilized. Sorption edge experiments, conducted at a TcO<sub>4</sub><sup>-</sup> concentration of  $1 \times 10^{-7}$  M, a solid-liquid ratio of 2 g/L, an electrolyte of 0.1 M NaCl, and an equilibrium time of 7 days, revealed a retention of TcO<sub>4</sub><sup>-</sup> on reduced clay minerals, with no retention observed on native clay minerals. This underscores the critical role of structural Fe(II) as the driving force for TcO<sub>4</sub><sup>-</sup> retention, showing a proportional relationship with its content. Furthermore, the adsorption of Fe<sup>2+</sup><sub>aq</sub> in the pH range of 6.5-7.5 onto the clay surface enhances TcO<sub>4</sub><sup>-</sup> retention. Sorption isotherm experiments demonstrated that TcO<sub>4</sub><sup>-</sup> retention is directly proportional to its concentration on all reduced clay minerals when the TcO<sub>4</sub><sup>-</sup> concentration is below  $10^{-5.5}$  M. Above this concentration, crystallization-like precipitation occurs on clay minerals with high structural Fe(II) content (11.4 wt%), while retention saturation is reached on those with low structural Fe(II) content (0.6 wt%). Spectroscopic measurements identified only TcO<sub>2</sub>·nH<sub>2</sub>O precipitate as the reduced species, with no adsorbed Tc species detected. Given the absence of adsorbed Tc surface complexes, outer-sphere electron transfer mechanism is hypothesized.

The findings of this thesis unequivocally demonstrate the capability of Fe(II)/Fe(III)-



bearing clay minerals to effectively immobilize Se and Tc. Despite both Se and Tc existing as anionic species, their distinct chemical properties lead to differing retention mechanisms. Selenite exhibits inner-sphere sorption complexes on reduced clay minerals, followed by a redox reaction facilitated by the presence of Se-O-Fe bonds which enable an efficient electron transfer and ultimately lead to precipitation of elemental Se(0). In contrast,  $\text{TcO}_4^-$  is not detected as adsorbed surface complexes on the reduced clays. However, it is still susceptible to reduction under the redox potential of the reduced clay minerals, leaving the electron transfer process as an uncharted territory in the redox reaction—a facet hitherto unexplored in the existing literature. While an outer-sphere electron transfer mechanism is speculated, further validation is needed.

The study examined the influence of various parameters, including the role of Fe in the clay mineral, pH levels, and radionuclide concentrations, on the retention of Se and Tc. In the context of a deep geological repository, the anoxic corrosion of the steel canister generates hydrogen and a substantial amount of Fe(II) (Wersin et al., 2003), which can interact with the engineered backfill clay materials, leading to higher Fe(II) content. The findings in this thesis demonstrate a proportional relationship between the retentions of Se and Tc and the presence of Fe(II). Therefore, conditions in the repository with an increased amount of Fe(II) can bolster the retention of Se and Tc. Moreover, the release of Fe(II) may lead to a lower redox potential in the backfill clay materials, further enhancing the retention of Se and Tc. These results from the sorption experiments contribute valuable data for sorption modeling and risk assessment in the context of the repository.

Beyond applications in deep geological repositories, the findings of this thesis hold promise for remediation efforts of Se- and Tc-contaminated sites. Some anthropogenic activities such as coal and oil combustion facilities, selenium refining plants, mining and milling operations, as well as various end-product manufacturers, may lead to the contamination of water and soil by Se (Fordyce, 2013; Tan et al., 2018). Over time, Se contamination in water can accumulate in the soil. In the US, leaking from waste tanks at the Hanford Site has caused a large area of soil to become contaminated by Tc (Pearce et al., 2018). These contaminated sites contain predominantly clay and clay-like minerals (Fredrickson et al., 2004; Krumhansl et al., 2002; Kukkadapu et al., 2006). The natural redox cycle in these environments can lead to the reduction of structural Fe(III) to Fe(II) in the clays through biological and natural processes (Corzo et al., 2018; Stucki et al., 2007). Consequently, the findings of this thesis on the retention of Se and Tc by Fe(II) in the clay

minerals play a crucial role in the remediation of Se- and Tc-contaminated sites.

## 6.2 Outlook

Sorption of Se(IV) on native clay minerals has been previously studied and modeled with a simple one-site model (surface complexes with only weak sites) (Missana et al., 2009). The kinetics of Se(IV) sorption on reduced clay minerals were explored in this thesis, revealing an exceedingly long reaction time to reach sorption equilibrium. For instance, High-red N<sub>Au</sub>-2 with Fe(II)<sub>str</sub> of 11.4 wt% achieved equilibrium after 720 h, while red SWy-2 with Fe(II)<sub>str</sub> of 2.5 wt% did not reach equilibrium even after 3600 h. Moreover, the impact of Fe(II)<sub>str</sub> content on the Se(IV) sorption kinetics has been studied at pH 5 and 7 under an initial selenite concentration of  $3 \times 10^{-5}$  M. Furthermore, the influence of redox potentials of reduced clay minerals has also been investigated at pH 5 and 7.

However, several aspects remain unexplored in the context of Se retention on Fe(II)/Fe(III)-bearing clay minerals: the influence of pH, Se concentration, and redox potential at different pH. Future investigations could involve Se sorption edge and sorption isotherm experiments on reduced clay minerals conducted over extended reaction times to ensure reaching reaction equilibrium. This approach can quantify the Se sorption on reduced clay minerals and shed light on the relationship between Se sorption and Fe(II)<sub>str</sub> content. Moreover, kinetics experiments could be carried out using clay minerals with higher Fe(II)<sub>str</sub> content under elevated Se concentrations to probe the potential formation of FeSe<sub>2</sub> or FeSe as reduced species. Additionally, introducing Fe<sup>2+</sup><sub>aq</sub> into kinetics experiments might reveal insights into the significance of Fe<sup>2+</sup><sub>aq</sub> presence and concentration in the kinetics of reduced species formation, along with the role of Fe(II)<sub>ad</sub> in Se retention. Further studies involving kinetics experiments at various pH levels or employing reduced clay minerals with different redox potentials would be valuable to elucidate how redox potential governs Se retention.

Studies have examined Tc(VII) sorption on both native and reduced clay minerals, confirming that Fe(II) plays a pivotal role in Tc retention, with the amount of Fe(II)<sub>str</sub> being directly linked to Tc retention. The systematic investigation has included Tc sorption as a function of pH and Tc concentration under four different Fe(II)<sub>str</sub> content and redox potentials. EXAFS analysis of clay samples with various experimental conditions revealed that TcO<sub>2</sub>·nH<sub>2</sub>O is the sole identified reduced species, indicating the absence of a Tc-Fe pair, leaving the electron transfer mechanism in Tc retention uncertain.

However, in the realm of Tc retention on Fe(II)/Fe(III)-bearing clay minerals, several

key aspects have yet to be explored, including the solid to liquid ratio (S/L),  $\text{Fe(II)}_{\text{ad}}$ , electron transfer mechanism, and sorption reversibility remain. In the future, Tc sorption can be performed at different S/L ratio to investigate the relevance between Tc retention and S/L ratio. Additionally, due to the observed enhancement of  $\text{Fe(II)}_{\text{ad}}$  to Tc retention around pH 7, further studies can involve Tc sorption on reduced clay minerals which are stabilized with different amount of  $\text{Fe}^{2+}$  at pH 7, in order to quantify the impact of  $\text{Fe(II)}_{\text{ad}}$  to Tc retention. Moreover, a proposed outer-sphere electron transfer mechanism in Tc retention could be investigated further. To achieve a better understanding, numerical modelling utilizing the Marcus theory to predicate the outer-sphere electron transfer rates (Rosso and Rustad, 2000; Rosso and Morgan, 2002), coupled with kinetics experiments on Tc retention employing High-Speed Channel Electrode methodologies (Clegg et al., 2004), might prove insightful. Fe isotope-labeled clay minerals can be used to trace the electron transfer pathway via Fe atoms. Upon suspecting the possibility of electron transfer by hydrogen bond between clay mineral surface and hydrated  $\text{TcO}_4^-$  anions, a hydrogen bond sensitive technique like Fourier Transform Infrared Spectroscopy (FTIR) may be used to help validate our hypothesis. Furthermore, conducting in-situ Tc retention experiments could provide valuable insights into the interface reaction between Tc and  $\text{Fe(II)/Fe(III)}$ -bearing clay minerals. Additionally, experiments examining the desorption or oxidation of retained Tc could aid in investigating the reversibility of Tc retention and assessing the stability of the reduced species.

## 6.3 Reference

- Clegg A. D., Rees N. V., Klymenko O. V., Coles B. A. and Compton R. G. (2004) Marcus Theory of Outer-Sphere Heterogeneous Electron Transfer Reactions: Dependence of the Standard Electrochemical Rate Constant on the Hydrodynamic Radius from High Precision Measurements of the Oxidation of Anthracene and Its Derivatives in Nonaqueous Solvents Using the High-Speed Channel Electrode. *Journal of the American Chemical Society* **126**, 6185-6192.
- Corzo A., Jiménez-Arias J. L., Torres E., García-Robledo E., Lara M. and Papaspyrou S. (2018) Biogeochemical changes at the sediment–water interface during redox transitions in an acidic reservoir: exchange of protons, acidity and electron donors and acceptors. *Biogeochemistry* **139**, 241-260.
- Fordyce F. M. (2013) Selenium Deficiency and Toxicity in the Environment. In *Essentials of Medical Geology: Revised Edition* (ed. O. Selinus). Springer Netherlands, Dordrecht. pp. 375-416.
- Fredrickson J. K., Zachara J. M., Kennedy D. W., Kukkadapu R. K., McKinley J. P., Heald S. M., Liu C. and Plymale A. E. (2004) Reduction of  $\text{TcO}_4^-$  by sediment-associated biogenic Fe(II). *Geochimica et Cosmochimica Acta* **68**, 3171-3187.
- Krumhansl J. L., Brady P. V. and Zhang P.-C. (2002) Soil Mineral Backfills and Radionuclide Retention. In *Geochemistry of Soil Radionuclides*. pp. 191-209.
- Kukkadapu R. K., Zachara J. M., Fredrickson J. K., McKinley J. P., Kennedy D. W., Smith S. C. and Dong H. (2006) Reductive biotransformation of Fe in shale–limestone saprolite containing Fe(III) oxides and Fe(II)/Fe(III) phyllosilicates. *Geochimica et Cosmochimica Acta* **70**, 3662-3676.
- Missana T., Alonso U. and García-Gutiérrez M. (2009) Experimental study and modelling of selenite sorption onto illite and smectite clays. *Journal of Colloid and Interface Science* **334**, 132-138.
- Pearce C. I., Serne R. J., Saslow S. A., Um W., Asmussen R. M., Miller M. D., Qafoku O., Snyder M. M. V., Resch C. T., Johnson K. C., Wang G., Heald S. M., Szecsody J. E., Zachara J. M., Qafoku N. P., Plymale A. E. and Freedman V. L. (2018) Characterizing Technetium in Subsurface Sediments for Contaminant Remediation. *ACS Earth and Space Chemistry* **2**, 1145-1160.
- Rosso K. M. and Rustad J. R. (2000) Ab Initio Calculation of Homogeneous Outer Sphere Electron Transfer Rates: Application to  $\text{M}(\text{OH}_2)_6^{3+/2+}$  Redox Couples. *The Journal of Physical Chemistry A* **104**, 6718-6725.
- Rosso K. M. and Morgan J. J. (2002) Outer-sphere electron transfer kinetics of metal ion oxidation by molecular oxygen. *Geochimica et Cosmochimica Acta* **66**, 4223-4233.
- Stucki J. W., Lee K., Goodman B. A. and Kostka J. E. (2007) Effects of in situ biostimulation on iron mineral speciation in a sub-surface soil. *Geochimica et Cosmochimica Acta* **71**, 835-843.

- Tan L. C., Nancharaiah Y. V., van Hullebusch E. D. and Lens P. N. (2018) Selenium: environmental significance, pollution, and biological treatment technologies. *Anaerobic treatment of mine wastewater for the removal of selenate and its co-contaminants*, 9-71.
- Wersin P., Johnson L. H., Schwyn B., Berner U. and Curti E. (2003) Redox Conditions in the Near Field of a Repository for SF/HLW and ILW in Opalinus Clay, Nagra Technical Report NTB 02-13, Nagra, Wettingen, Switzerland.



# Declaration of consent


on the basis of Article 18 of the PromR Phil.-nat. 19

Name/First Name:	<input type="text" value="Qian, Yanting"/>
Registration Number:	<input type="text" value="19-124-288"/>
Study program:	<input type="text" value="Earth Sciences"/>
	Bachelor <input type="checkbox"/> Master <input type="checkbox"/> Dissertation <input checked="" type="checkbox"/>
Title of the thesis:	<input type="text" value="Coupled adsorption and redox interface reactions governing the retention of Se and Tc on Fe(II)/Fe(III)-bearing clay minerals"/>
Supervisor:	<input type="text" value="Prof. Dr. Sergey Churakov"/>

I declare herewith that this thesis is my own work and that I have not used any sources other than those stated. I have indicated the adoption of quotations as well as thoughts taken from other authors as such in the thesis. I am aware that the Senate pursuant to Article 36 paragraph 1 litera r of the University Act of September 5th, 1998 and Article 69 of the University Statute of June 7th, 2011 is authorized to revoke the doctoral degree awarded on the basis of this thesis.

For the purposes of evaluation and verification of compliance with the declaration of originality and the regulations governing plagiarism, I hereby grant the University of Bern the right to process my personal data and to perform the acts of use this requires, in particular, to reproduce the written thesis and to store it permanently in a database, and to use said database, or to make said database available, to enable comparison with theses submitted by others.

Place/Date

  
Signature

Digitally signed by Yanting Qian  
Date: 2023.11.23 20:30:57  
+01'00'

